TECHNISCHE UNIVERSITÄT MÜNCHEN

WALTER SCHOTTKY INSTITUT

Zentralinstitut für Physikalische Grundlagen der Halbleiterelektronik

BERICHT
2005
ANNUAL REPORT

Walter Schottky Institut, TU München, Am Coulombwall, 85748 Garching, Germany

Druck und Einband: Herbert Hieronymus, München

Contents

		page
	Preface	**I**
1.	**The Walter Schottky Institut**	**V**
2.	**Scientific Activities**	
	Basic Semiconductor Physics	**1**
	Elimination of spurious solutions from multiband k·p models in real space discretization	2
	Self-consistent quantum transport theory of carrier capture in heterostructures	4
	Calculation of carrier transport through quantum dot molecules	6
	Novel 1D phases in a bent quantum Hall junction	8
	Coulomb blockade resonances and non-linear conductance in aluminum arsenide wires	10
	The ion sensitivity of surface conductive single crystalline diamond	12
	Electronic and optical properties of boron-doped nanocrystalline diamond	14
	Spin dynamics of optically stimulated charges in InGaAs self-assembled quantum dots	16
	Optical spectroscopy of individual quantum dot molecules	18
	Semiconductor Materials Science and Technology	**21**
	High mobility two dimensional hole gases on (110) GaAs substrates and cleave facets	22
	Transport in a vertical quantum wire fabricated with cleaved-edge over-growth	24
	Optical and magneto-transport properties of electrically gated CEO semi-conductor nanostructures	26
	High-resolution X-ray diffraction study of stress relaxation in Si-doped AlN grown by plasma-assisted molecular-beam epitaxy	28
	Electronic properties of AlN/diamond heterojunctions	30
	Ferromagnetic GeMn nanostructures	32
	Structural and magnetic properties of Mn_5Ge_3 clusters in a dilute magnetic germanium matrix	34
	Aluminum-induced crystallization of amorphous silicon-germanium thin films for photovoltaic applications	36
	Aluminum-induced crystallization of Si nanoparticle thin films dispersed from solution	38
	Molecular beam epitaxy of metal oxides	40
	Low resistive p-GaSb/n-InAsSb tunnel-junctions homogeneously doped with silicon for intra-device contacts	42
	n-doped epitaxial AlAsSb/GaSb distributed Bragg reflectors on GaSb substrate	44

Biochemical Semiconductor Applications **47**
Light-induced manipulation of DNA on amorphous silicon surfaces 48
Kinetic behavior of electrically manipulated DNA tethered to a gold surface 50
Controlling the surface density of DNA on Au by electrically induced desorption 52
Functionalization of ultrananocrystalline diamond thin films by biphenyl diazonium cations 54
Characterization of a chemically passivated GaAs based sensor device in electrolytes 56
Enzyme-modified AlGaN/GaN field effect transistors 58
Nano-engineering of III-V semiconductor cleaved planes for molecular electronics applications 60

Devices and Device Concepts **63**
The 3D nanometer device simulation project nextnano++ 64
Black silicon surfaces – vanishing reflectivity via nano-scale texturing 66
Micro mechanically tunable long wavelength VCSEL with extended tuning range of 60nm 68
1.55 µm Vertical-Cavity Laser Diodes at 10 Gb/s 70
State-of-the-art widely tunable laser diodes with distributed feedback 72
Widely tunable Mach-Zehnder interferometer lasers 74
Low-threshold injectorless quantum-cascade lasers emitting at ~7.9 µm 76
Progress towards an electrically driven single photon source based on two dimensional photonic crystal nanocavities 78

3. Research Funding and Collaborations **81**

4. Members of the Institute and Guest Scientists **84**

5. Doctorate, Diploma, Bachelor, and Master Theses **87**

6. Publications **90**

7. Invited Talks **100**

8. Courses, Seminars, and other Scientific Activities **109**

9. Selected Topics of Semiconductor Physics and Technology **113**

Addresses **119**

Preface

On behalf of all members of the Walter Schottky Institut of the Technische Universität München, I am pleased to present you this annual report and hope that you will find it informative and interesting. The report gives an overview of the research and teaching activities of the institute during the year 2005. As in the previous years, the efforts have been focussed on the four main areas of semiconductor electronics research:

- basic semiconductor physics combined with the development of new experimental approaches
- semiconductor materials science including the growth and manipulation of semiconductors with micro- and nanometer resolution
- biochemical semiconductor applications, and
- realization and modelling of novel semiconductor devices.

Throughout 2005, an average of 19 faculty and scientific staff members, 20 members of the administrative and technical staff, 50 doctorate candidates, 40 diploma students, and some 10 short and long term international guests belonged to the institute. 10 PhD theses, 15 diploma, 2 bachelor and 5 master theses were completed in 2005. 84 journal and conference paper, and 84 invited talks again demonstrate the scientific productivity of the institute.

In 2005 again several considerable acknowledgements were achieved by members of the institute: Ulrich Rant was assigned the "Promotionspreis des Bundes der Freunde (BdF) der TU München e.V." as well as the "Forschungspreis des Landes Steiermark für Nanowissenschaften und Nanotechnologien 2005 – Kategorie Nachwuchsförderung". Also the "Chorafas-Preis 2005" was awarded to Andrea Baumer.

Let me finally thank all colleagues, collaborators, students, and post-docs for their participation and extensive work carried out in teaching and research and express my appreciation to our friends and sponsors for their continuous support and interest in our work.

Garching, February 2006 Markus C. Amann

Our PhD's of 2005

Frank Fischer

Ulrich Rant

Markus Grau

Ingo Bormann

Robert Shau

Dominique Bougeard

Andreas Kreß

Andrea Baumer

Karin Buchholz

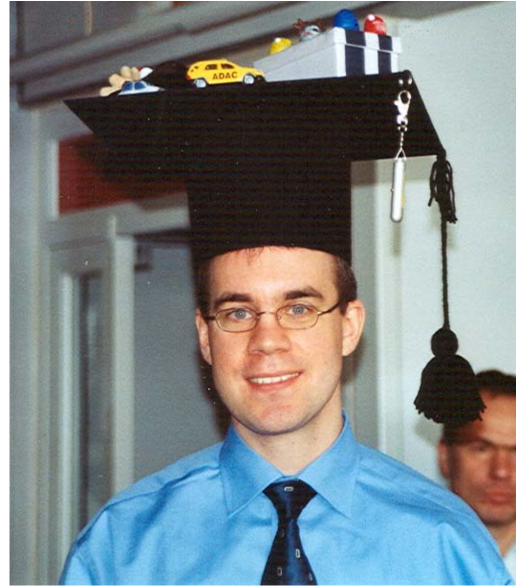

Jochen Bauer

1. The Walter Schottky Institut

History

The Walter Schottky Institut (WSI) is a Central Institute of the Technical University of Munich (TUM). It was founded in order to strengthen the interaction between basic physics and semiconductor electronics research and development. After the decision was made to create such an interdisciplinary research institute in early 1986 it took about two years until the new laboratories became operational in May 1988. This exceptionally short time for planning and construction of a modern institute building was made possible by the excellent cooperation between the Siemens AG, the Bavarian ministries, and the TUM.

Resources

The WSI building contains laboratories and offices with a total area of about 2400 m^2. It is well equipped with state-of-the-art facilities for semiconductor preparation, characterization, and device technology. The main resources are listed in the following:

Materials preparation and semiconductor technology
Epitaxy systems for GaAs, InP, GaSb, GaN/AlGaN, and SiGe based heterostructures (MBE, CBE, plasma-induced MBE, MOCVD)
Ultrahigh purity GaAs MBE machine (electron mobilities > 10 Mio cm^2/Vs)
UHV evaporation equipment for SiGe on glass
Plasma-enhanced Si-CVD
Pulsed laser processing
Laboratory for surface modification / biofunctionalization
250 m^2 class 100 clean room facility with photolithography, e-beam lithography, reactive ion etching, metallization

Characterization and spectroscopy tools
High resolution X-ray diffraction
Atomic force microscopy
Electron microscopy and EDX equipment
Photoluminescence and Raman spectroscopy (from IR to UV)
DLTS, Optical DLTS, CV-profiling
Hall measurements and magneto-transport
FTIR spectroscopy
X-ray photoelectron spectroscopy
High frequency parameter analyzers
Electron spin resonance (ODMR, EDMR)
He^3 cryostats with magnetic fields up to 15 and 17 Tesla
Special characterization facility for laser diodes

Computational facilities
High end workstations

Research groups

The WSI accommodates four research groups headed by **Gerhard Abstreiter, Markus-Christian Amann**, **Martin Stutzmann,** and **Peter Vogl**, with a total headcount of about 90 including scientific and technical staff, secretaries, and doctorate as well as diploma (master) students. Out of these, about 25 permanent positions are funded by TUM, while basically all the doctorate positions are financed via external research projects with external funding. The main research interests are:

- fabrication and characterization of new semiconductor materials, material combinations, as well as hetero- and nanostructures
- basic physics with emphasis on electronic and optical properties of low dimensional systems
- realization of new semiconductor devices for application in ultrafast electronics, optoelectronics, and sensors
- theory and simulation of modern semiconductor materials and devices

Experimental Semiconductor Physics I (Gerhard Abstreiter, Jonathan J. Finley):

Research projects of this group deal with various aspects of electronic and optical properties of low-dimensional, mesoscopic semiconductor structures, the heteroepitaxy of group IV and III-V semiconductors, the development of novel methods for lateral patterning and of analytical tools for the characterization of nanometer-size structures, as well as the fabrication and test of new, unconventional electronic and optoelectronic devices. Examples for basic research are optical spectroscopy of single quantum dots, cleaved edge overgrowth on GaAs, magnetotransport in ultrahigh mobility GaAs heterostructures as well as electronic transport and tunneling in edge channels and one-dimensional systems. Device and technology oriented work aims at novel concepts for charge and spin storage in quantum dots, coherent devices based on quantum dots for future quantum information technology, photonic crystal microcavities for efficient single photon sources and the test of semiconductor nanaostructures for chemical/biological sensors. A new area of research is the controlled manipulation of oligonucleotides on gold surface for possible protein detection and the development of SOI based lab-on-a-chip systems.

Semiconductor Technology (Markus-Christian Amann):

The research activities in this group are concentrated on modern technologies for III-V compound semiconductors and their use for developing advanced electronic and optoelectronic devices. This comprises the development of epitaxial, patterning, microstructuring, etching and coating techniques as well as the design and fabrication of semiconductor laser diodes and other photonic components. The applied material systems are GaAs-AlGaAs, InGaAsP-InP and antimonide based compounds that are grown with molecular beam epitaxy (MBE) and chemical beam epitaxy (CBE) with an accuracy in the nanometer regime. Device structuring in the 100-nm-range is obtained by using electron-beam lithography. Reactive ion etching enables the well-defined processing of the various devices with a high

material selectivity of the etching rate. The group is also well equipped with evaporation and sputtering techniques for passivation and contacting of the devices. Among the key devices are single-mode and wavelength-tunable laser diodes for the wavelength range between 1300 and 2200 nm using lattice-matched and strained InGaAsP layers on InP substrates, InGaAsP and AlInGaAs vertical cavity surface-emitting laser diodes in the 1300-2000 nm wavelength range. Recent work also covers the development of wavelength-tunable laser diodes for wavelengths above 2 µm using antimonide based compounds and quantum cascade lasers in the range of 5 to 15 µm for gas sensing. In the field of high-frequency electronic devices, the generation of rf-output power at millimeter-wave frequencies up to 300 GHz is aspired. Active transit-time diodes as well as passive varactor structures for multipliers are investigated.

Experimental Semiconductor Physics II (Martin Stutzmann):

The work of this semiconductor physics group deals with various aspects of new and non-conventional semiconductor materials and material combinations:

- semiconductors with a wide bandgap (GaN, InGaN, AlGaN, diamond, SiC),
- disordered semiconductors (amorphous, nanocrystalline, and polycrystalline),
- advanced thin film systems (silicon-based luminescent layers, thin film solar cells, organic/anorganic heterosystems, biofunctionalized semiconductors, semimagnetic semiconductors)

Most of these material systems are prepared by suitable deposition techniques (MBE, Plasma-enhanced CVD, e-beam evaporation, sputtering). Their efficient optimization is based on the large pool of structural, optical, and electrical characterization techniques available in our institute. Complementary to the usual spectroscopic techniques we have developed and employ a variety of highly sensitive methods which enable us to study in particular the influence of defects on the electronic perfomance of materials and devices. Such techniques include subgap absorption spectroscopy, optically induced capacitance spectroscopy and, in particular, modern spin resonance techniques which are applied to various materials systems and devices for spintronics.

In addition to the preparation and characterization of new semiconductor materials we also work on the modification and processing of semiconductors with pulsed high power laser systems (laser-crystallization, holographic nanostructuring, laser-induced etching) and investigate the potential of new material systems for novel device structures. Recent examples include nanostructured thin film solar cells, high electron mobility transistors based on AlGaN/GaN heterostructures, as well as UV-detectors, sensors and biosensors.

Theoretical Semiconductor Physics (Peter Vogl):

The activity of this group focuses on the theoretical study of structural, electronic and optical properties of semiconductors. The work deals with mesoscopic structures, new materials, and novel devices, in the attempt to understand their basic physics and to predict their

behavior. The research conducted in the group aims at the development of theoretical tools which can support present experimental activities and propose new ideas and solutions for the future, as indicated by the strong interaction with industrial laboratories and with engineering university departments. Sophisticated quantum mechanical calculations are used for determining the electronic structures and the optical properties of a variety of semiconductor materials and systems. The information from such fundamental studies constitute the basis for the analysis of the transport properties of such materials and for the development of reliable numerical tools for device modeling. Recent activities in this group include ab-initio studies of spin devices, prediction of novel magnetic field effects, development of multiscale methods for film growth, and the design and modeling of semiconductor based quantum information devices.
The research activity of the institute thus covers a wide spectrum from basic physics in low-dimensional semiconductor structures to the development of novel or improved electronic, optoelectronic and sensor devices based on semiconductor hetero- and nanostructures. The close collaboration between the different groups and the availability of various experimental techniques are the essential basis for the successful development of novel semiconductor devices. Close contacts with industrial partners have also proven to be very fruitful and stimulating in developing new ideas and in following new directions which may be relevant for future applications.

Apart from the extensive research activities all groups are involved in teaching within their respective departments. Besides the usual teaching responsibilities in undergraduate and graduate courses, special emphasis is put on the education of diploma and doctoral students in the physics and technology of present and future devices and of low dimensional semiconductor structures.

1

Basic Semiconductor Physics

Elimination of spurious solutions from multiband k·p models in real space discretization

Till Andlauer[1] and Peter Vogl

Multiband **k·p** models together with the envelope function approximation are frequently used to describe the electronic band structure of semiconductors in situations, where non-parabolicity is important. It is well known, that such models can produce spurious solutions, such as artificial band gap states. We have performed a systematic analysis of these deficiencies and developed a suitable method to eliminate them in real space discretization.

Multiband **k·p** theory forms a good approximation to the correct band structure only close to the band edges, i.e. for small values of the wave vector k. Models that take coupling of conduction and valence bands into account can have additional large spurious wave vector solutions for small energy values. In superlattices or heterostructures, large k values are folded back to small values close to the zone center. They can produce spurious eigenstates, either lying within the band gap, or forming bound states with an unphysical short wavelength contribution. In Fig. 1 we illustrate this problem using a simple two-band Kane model for electrons and light holes.

We have solved this problem by an appropriate rescaling of material parameters, which modifies the Hamiltonian in such a way that it does no longer lead to spurious solutions. In fact, we eliminate the parameter that describes free-electron and remote-band contributions to the conduction band effective mass, and rescale the interband momentum matrix elements to maintain the correct effective mass values. This leads to a bandstructure that does not have large wave vector solutions for small energy values. Therefore, spurious eigenstates no longer occur. This solution applies straightforwardly to the more realistic eight-band model.

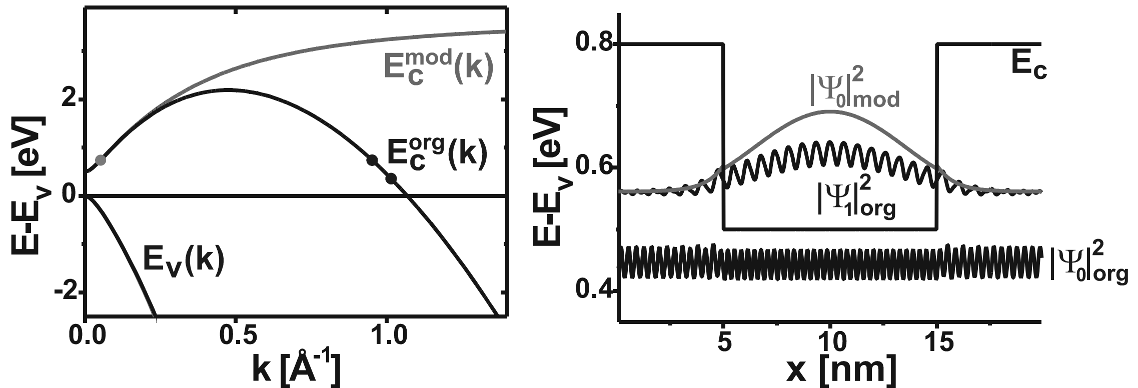

Fig. 1*: (a) Typical bandstructure for two-band Kane model with original (org) and modified (mod) Hamiltonian. Lowest energy eigenvalues of appropriate quantum well eigenstates are indicated. (b) Lowest eigenstates of a quantum well structure, formed by materials, that corresponds to the bulk bandstructure shown in (a).*

Multiband **k·p** Hamiltonians have been originally developped for bulk crystals. In nanostructures that lack translational invariance, the operator **k** becomes a differential

[1]phone: +49-89-289-14486, fax: +49-89-289-12737, email: andlauer@wsi.tum.de

operator which is multiplied by the position dependent material values. In order to guarantee a Hermitian Hamiltonian, this multiplication must be carried out carefully as the ordering matters. Several Hermitian orderings have been proposed, but most of them lead to contradictory boundary conditions at material interfaces, which can result in wave function singularities (Fig. 2). We have found an operator ordering that conserves not only the Hermiticita but, importantly, the self-adjointness of the Hamiltonian and avoids singularities in the wave functions.

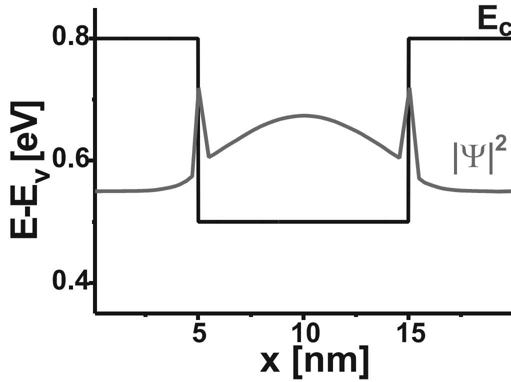

Fig. 2: *Sketched wave function singularities at material interfaces for incorrect operator ordering.*

Whenever Schroedinger's equation is solved on a discrete real space lattice, it is common practice to approximate first derivatives by centered finite differences. When applying this method to multiband **k·p** Hamiltonians that contain k-linear terms, one obtains a discretization that does not rule out unphysical fast oscillating wave functions (Fig. 3.).

We have developed a new discretization scheme that eliminates this problem. The method adds an artificial diffusion term to the Hamiltonian that stabilizes the discretization. The approach is analogous to upwinding schemes that are used for hyperbolic differential equations. The correction term only modifies the high k behavior, while preserving the physically relevant low k spectrum of the model, and vanishes in the limit of infinitely small grid spacing.

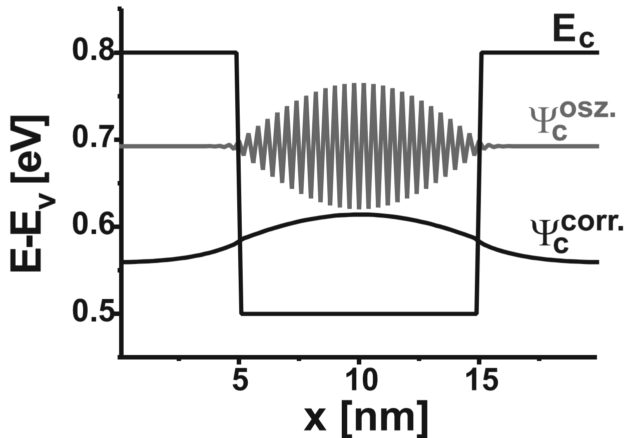

Fig. 3: *Fast oszillating wave function (osz.) for centered finite differences discretization and correct one (corr.) obtained by our stabilized discretization scheme.*

We have combined this discretization scheme with a finite volume method and formulated it in a dimension-independent manner. Therefore it automatically guarantees flux conservation and a consistent treatment of different dimensional nanostructures. It is used for a very efficient and compact implementation in our 3D nanometer device simulation project next**nano**++.

supported by Österreichische FWF (Projekt IR-ON F025)

Self-consistent quantum transport theory of carrier capture in heterostructures

Tillmann Kubis[1], Alexandros Trellakis, and Peter Vogl

A realistic description of carrier transport through semiconductor heterostructures at room temperature requires the treatment of multiple scattering and quantum effects such as carrier confinement, interferences and carrier capture on an equal footing. One of the most widely used methods for this purpose is the non-equilibrium Green's function method (NEGF). NEGF allows for the calculation of scattering states (represented by the retarded Green's function) and their occupation far from equilibrium (represented by the lesser Green's function). We have implemented the NEGF formalism fully self-consistently for resistive open devices where multiple scattering is significant. We take into account acoustic and polar-optical phonon scattering, including their full momentum and energy dependence, and the electron-electron scattering in Hartree approximation. The coupling between the lesser and the retarded Green's function is fully taken into account. In this way, the scattering states, the transition probabilities between them and their occupations are calculated self-consistently. In addition, we include the scattering within the leads self-consistently with the device regions close to the Ohmic contacts. This is necessary to match the density of states of the Ohmic leads to that of the device to avoid quantum mechanical reflections.

The structures specifically considered are assumed to be homogeneous in the lateral (x, y) directions, and to be in contact with two reservoirs at $z = 0$ and $z = L$. The electrons are described by a single conduction band with effective mass m^*.

In order to illustrate the influence of scattering in a short device, we have performed systematic NEGF calculations for GaAs n-i-n structures with an InGaAs quantum well within the intrinsic region. The total length of the device is 50 nm with 16 nm intrinsic region embedded in between the two 17 nm n-regions with $n = 1\times 10^{18} cm^{-3}$ each. Within the intrinsic region, there is a 12 nm $In_{.14}Ga_{.86}As$ quantum well of 150 meV depth. The polar optical phonon energy is $\hbar\omega = 35\,\text{meV}$.

In Fig. 1, we show a NEGF calculation for the n-i-n with no bias applied but all scattering mechanisms fully included. The figure displays a contour plot of $\rho(E,z) = -2\,\text{Im}\int d^2k G^<(z,z,k,E)/(2\pi)^3$, i.e. the local, energy-resolved density, as a function of energy and position within the device. The self-consistent total potential is indicated by a full line. When $\rho(E,z)$ is integrated over the energy, we obtain the density. The zero of energy is always put at the Fermi level of the left contact. To the right of the figure, we display the local density of states near the center of the well region (marked by an arrow). The lowest well state is a true bound state whereas the second one is a resonance state an electron can tunnel out from into the leads. The bottom of the second state lies 59.4 meV below the top edge of the well which is significantly larger than an optical phonon energy. The lowest bound state lies 37.6 meV below the second level which is also a bit larger than $\hbar\omega$. Because we treat scattering within the self-consistent Born approximation, the combination of elastic and inelastic scattering can fill both states in the stationary state.

---

[1]phone: +49-89-289-12762, fax: +49-89-289-12737, email: kubis@wsi.tum.de

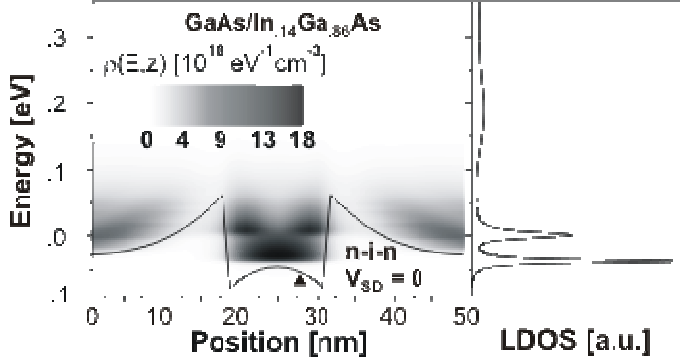

Fig. 1: Contour plot of energy-resolved electron density as a function of energy and position for the GaAs n-i-n with InGaAs quantum well described in the text at zero bias. The full line shows the self-consistent potential. To the right is the local density of states near the center of the well region (marked by an arrow).

In Fig. 2, we show the same device under an applied bias of effectively 150 mV. As one can clearly see, the resonance corresponding to the second well state has been largely emptied by tunneling towards the right lead so that only the lowest well state remains significantly occupied.

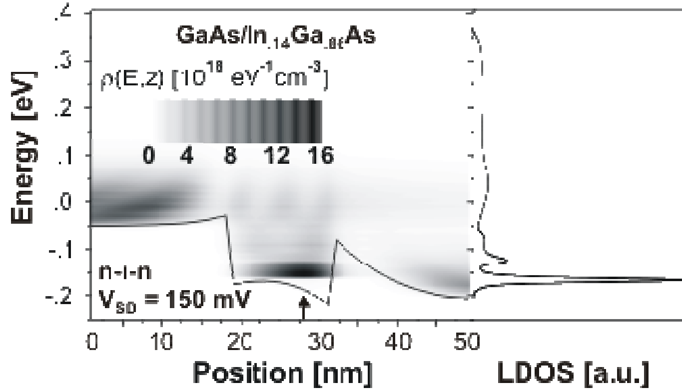

Fig. 2: Same as Fig. 1, but with a bias of effectively 150 mV applied. The second well state is largely emptied by tunneling into the right lead.

The effect of scattering can be seen from comparing the results in Fig. 1 with the contour plot in Fig. 3 where all phonon scattering mechanisms are *neglected* and only the Hartree Coulomb interaction is taken into account. Due to the absence of inelastic scattering, the carriers cannot fill the quantum well but occupy a resonance that is derived from the third quantum well state. This explains the interference pattern in the well region.

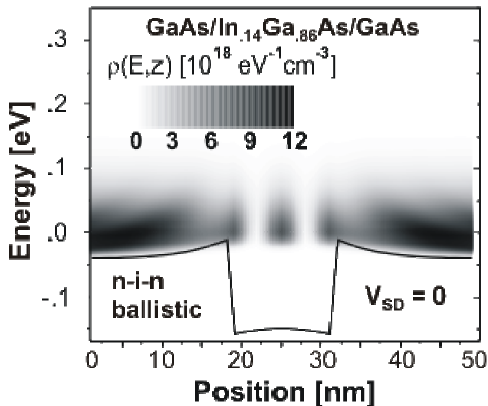

Fig. 3: Contour plot of energy-resolved electron density for the GaAs n-i-n with InGaAs quantum well at zero bias ***without*** *phonon scattering (ballistic device). The full line shows the self-consistent potential. Without any energy relaxing mechanisms the well states remain empty.*

---

supported by DFG (SFB 631, C1)

Calculation of carrier transport through quantum dot molecules

Tobias Zibold[1], Matthias Sabathil, and Peter Vogl

Quantum dot molecules (QDM) composed of vertically stacked self assembled quantum dots (QDs) are promising candidates for a solid state based implementation of quantum information processing. Here we present our quantitative theoretical analysis of the ballistic current through a QDM based on two vertically stacked QDs embedded within a resonant tunneling diode (RTD). In particular, we show that measurements of the resonant tunneling current provide a wealth of unique information about the size, geometry, and the energy levels of the QDM. Our calculations are based on a fully three-dimensional model of the RTD with realistically shaped QD structures. The local strain is calculated by minimizing the total elastic energy of the entire device. We solve the Poisson equation including the piezoelectric charges and subsequently calculate the ballistic current in terms of the contact block reduction method. This scheme computes the quantum states of the open system with scattering boundary conditions rigorously. The quantum states themselves are evaluated in terms of the single-band Schrödinger equation for the conduction bands, taking into account spatially varying electron masses, band offsets, deformation potentials, and the electrostatic potential due to the piezoelectric charges. All calculations are carried out within the framework of next**nano**^{3}.

The RTD as depicted in the inset of Fig. 1 is composed of a 33 nm thick InP barrier with two embedded InAs QDs that are grown on 0.5 nm thick wetting layers (WLs). The distance between the WLs is 15 nm. This RTD was studied experimentally by Bryllert *et al.* [1]. Upon applying a bias, pairs of bound states in the two adjacent QDs can be brought into resonance with one another, thereby increasing the electron transmission probability by several orders of magnitude. Figure 1 shows the experimentally determined as well as the theoretically predicted current. The two QDs were modeled by truncated pyramids of 2.5 (5) nm height and 12 (16) nm base width, respectively. The difference ΔE_0 of the zero bias ground state energies is 87 meV. The peak height and the line width of the current resonance depend strongly on the inter-dot distance and the lateral misalignment, which may explain the differences between theory and experiment. In fact, Fig. 2 shows the line width of the resonance to decrease exponentially with increasing QD distance which

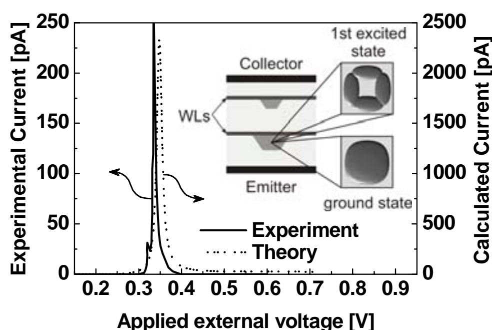

***Fig. 1:** The experimental and calculated current through the InAs/InP QDM as a function of the applied bias. The inset shows the structure of the device, including the leads (black), WLs (dark gray), and the QDs (light gray), schematically. Furthermore, a top view of the 3D orbitals of the ground and first excited state of the large QD are plotted.*

[1]phone: +49-89-289-12740, fax: +49-89-289-12737, email: tzibold@wsi.tum.de

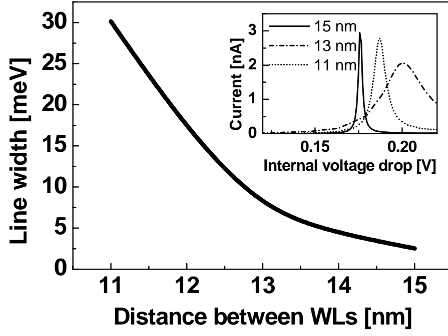

Fig. 2: Calculated resonance line width as a function of the inter-dot distance. The inset shows the resonances for WL distances of 11, 13, and 15 nm, respectively. The peak current increases with increasing inter-dot distance, whereas the integrated current falls off exponentially.

reflects the exponential decrease in the QD coupling. The inset shows the shape of several current resonances explicitly.

As depicted in the inset of Fig. 3a, an additional resonance may occur if the excited state **1** in the large dot lies in resonance with the ground state **0'** of the small dot. Figure 3 displays the ratio between the peak currents of the **1** → **0'** resonance and the **0** → **0'** resonance as a function of the relative lateral displacement of the two QDs.

The larger QD close to the emitter may be charged by emitter electrons. This charging decreases the energy difference ΔE_0 and shifts the resonance bias as is illustrated in the inset of Fig. 3b. This shift decreases for larger base width, as shown in Fig 3b, and can therefore be used to estimate the lateral dimensions of the large QD.

The peak heights and positions, and the line widths of the tunneling resonances through ground and excited states yield quantitative information about the energy levels, base widths, distance and lateral alignment of the QDs in a quantum dot molecule.

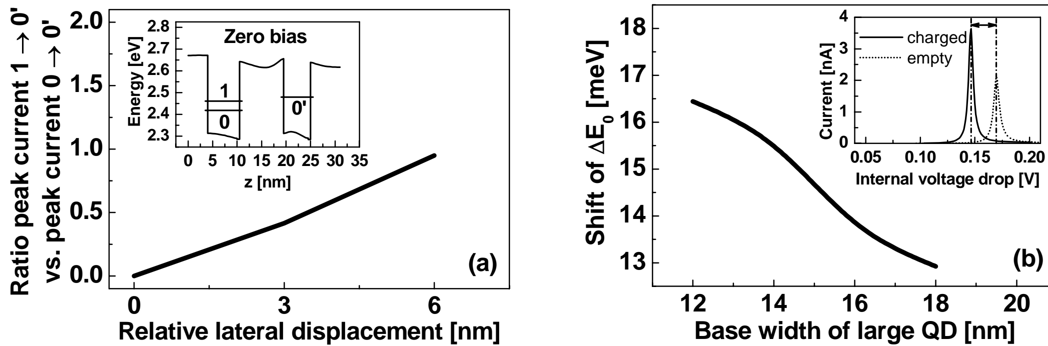

***Fig. 3:** (a) Ratio between the peak currents of the 1 → 0' resonance and the 0 → 0' resonance as a function of the relative lateral displacement of the two QDs. The inset shows the energies of the ground state 0 and excited state 1 in the large QD and of the ground state 0' in the small QD. (b) Change in the zero-bias energy difference ΔE_0 between the two QD ground states due to charging of the large QD, plotted as a function of the base width. The inset shows the shift of the current resonance for the neutral and charged situation.*

[1] Bryllert, T., Borgstrom, M., Wernersson, L.-E., Seifert, W., and Samuelson, L., Appl. Phys. Letters **82**, 2655 (2003).

---

supported by DFG (SFB 631, C1)

Novel 1D phases in a bent quantum Hall junction

Matthew Grayson[1], Lucia Steinke, Dieter Schuh, Max Bichler, and Gerhard Abstreiter

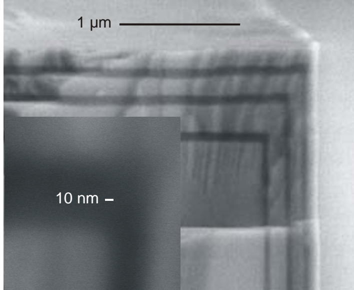

***Fig. 1:** Electron micrograph demonstrating corner-overgrowth principle*

We study a novel one-dimensional wire state which arises at the corner of two quantum Hall systems joined at a 90° angle, and observe one-dimensional metallic and insulating states. Such sharp non-planar confinement structures are unconventional in the quantum Hall effect and reveal the first observation of a macroscopic one-dimensional conductor state whose conductance increases with decreasing temperature.

Using the corner-overgrowth technique invented at the WSI [1], we create a two-dimensional (2D) electron system that is bent at an atomically sharp angle of 90º (Fig. 1). In a tilted magnetic field (Fig 2, inset) both facets of the bent quantum well form quantum Hall systems, where the ratio of filling factors is tuned by the tilt angle. The device itself is 3 mm long and less than 1 mm^2 cross section (shown schematically in Fig. 2, inset) with ohmic contacts alloyed on both facets away from the junction. The sharp bend at the overgrown corner acts as boundary for both 2D systems, and quantum Hall edge channels propagate along the corner in opposite directions. These counter-propagating channels form a novel one-dimensional (1D) system, bound on both sides by the quantum Hall gap. We call this the bent quantum Hall wire. At equal filling factors on both facets the wire has an equal number of forward and reverse propagating modes.

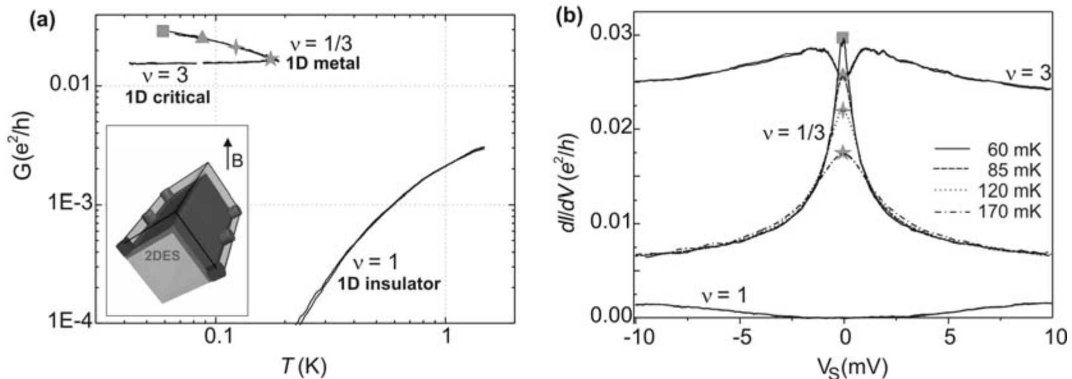

***Fig. 2:** (**a**) Bent QH wire conductance G vs. T at filling factor ν = 1/3 shows an increasing conductance with decreasing temperature, indicative of 1D metallic behavior. The filling factors ν = 1 and ν = 3 are examples of the insulating and critical phase, respectively. (**b**) The DC voltage dependence of the differential conductance dI/dV vs. V_S for the same filling factors. ν = 1/3 (60 mK) shows a dramatic increase in conductance with decreasing bias. At higher temperatures the peak height at ν = 1/3.*

Fig. 2 shows the results of conductance measurements. The bent quantum Hall wire features three different 1D quantum phases, which depend on the filling factor in the facets.

[1]phone: +49-89-289-12778, fax: +49-89-3206620, email: grayson@wsi.tum.de

At a given filling factor we measured the wire conductance as a function of temperature (Fig. 2a) and differential conductance as a function of dc voltage bias (Fig. 2b). With decreasing temperature *T*, the conductivity of the corner wire in Fig. 2a either decreases ($\nu = 1$), stays constant ($\nu = 3$), or increases ($\nu = 1/3$), illustrating what we call insulating, critical, or metallic 1D behavior, respectively. In Fig. 2b, the differential conductance *dI/dV* also shows different behaviors at different ν. The metallic state *dI/dV* increases, forming a cusp at zero bias ($\nu = 1/3$). Varying the temperature up to 170 mK while measuring this cusp shows that most of the temperature dependence occurs at the small biases. The so-called critical phase ($\nu = 3$) shows the weakest bias dependence, with mild downturns at low bias reminiscent of the insulating phase, and mild upturns at high bias reminiscent of the tails of the metallic cusp.

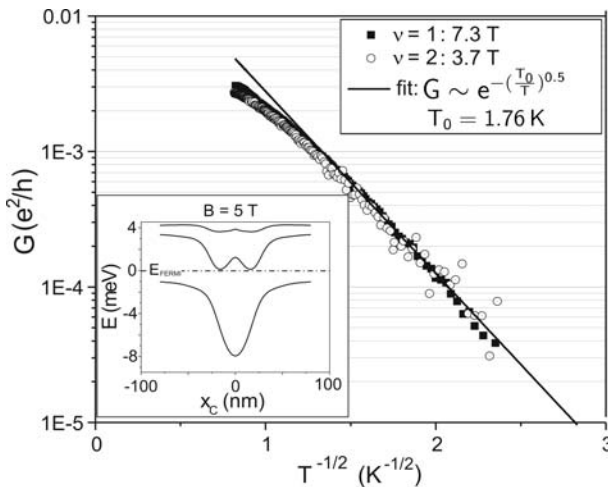

Fig. 3: *Temperature dependence of the 1D wire conductance at $\nu = 1$ and $\nu = 2$, plotted vs. $(1/T)^{1/2}$. The conductance is approximately exponential in $(1/T)^{1/2}$. The inset shows a spin-unresolved Hartree calculation of the wire dispersion at B = 5T, predicting a bandgap insulator.*

The insulating phase could be understood as a 1D bandgap insulator, predicted for high magnetic fields (B > 5T) by spin-unresolved Hartree calculations of the wire dispersion (Fig. 3, inset). This agrees roughly with the observed insulating behavior at $\nu = 2$ (3.7 T) and $\nu = 1$ (7.3 T). The plots in Fig. 3 show that the 1D wire conductance at both filling factors is approximately exponential in $(1/T)^{1/2}$. This is in good agreement with the behavior predicted for variable-range hopping conduction. An alternative explanation could be a transition from Drude conduction to a strongly localized state with an intermediate weak localization regime [2].

How a metallic 1D phase could arise at $\nu = 1/3$ is described in one theoretical model [3]. The temperature dependence is here predicted to behave as a power-law $G(T) \sim T^{\alpha}$ which in Fig. 2 would give an exponent $\alpha = -0.5$. The factor of 4 in temperature is insufficient to establish a convincing quantitative power-law, and more data needs to be collected at $\nu = 1/3$. Yet we can report the first qualitative observation of a macroscopic 1D metallic state [4].

[1] M. Grayson, D. Schuh, M. Huber, M. Bichler, and G. Abstreiter, Appl. Phys. Lett. **86**, 192106 (2005)
[2] I. V. Gornyi, A. D. Mirlin, and D. G. Polyakov, Phys. Rev. Lett. **95**, 046404 (2005)
[3] C. Kane and M. P. A. Fisher, Phys. Rev. B **56**, 15231 (1997)
[4] M. Grayson, L. Steinke, D. Schuh, M. Bichler, L. Hoeppel, J. Smet, K. v. Klitzing, D. K. Maude and G. Abstreiter, submitted to Nature

---

supported by DFG (Quanten-Hall Schwerpunkt) AB 35/4-3

Coulomb blockade resonances and non-linear conductance in aluminum arsenide wires

Joel Moser, Shivaji Dasgupta[1], Dieter Schuh, Max Bichler, Gerhard Abstreiter, and Matthew Grayson

One dimensional (1D) systems of the aluminum arsenide (AlAs) quantum wires have heavy electrons and a double valley degeneracy making them qualitatively different from GaAs. Previous work described the fabrications of these AlAs nanostructures and studied the non-linear transport and unconventional temperature dependence of the resonances. Here we report low-temperature differential conductance measurement in AlAs cleaved-edge overgrown quantum wires in the pinch-off regime.

The quantum wire samples are fabricated from a 150Å -wide, modulation-doped AlAs 2D electron system sandwiched between two AlGaAs spacers and grown on a (001) GaAs substrate (Fig.1 (inset)). The substrate is cleaved *in-situ* at the perpendicular (110) plane and overgrown with another modulation-doped barrier. Electrons in the two degenerate X-valleys accumulate along the cleaved edge of the 2DES and form the doubly valley-degenerate 1D system. A 1µm-wide metal gate on the substrate depletes the 2DES underneath and varies the wire density in the segment located below it. The 2DES regions on each side of the gate serve as ohmic contacts, and conductance measurements are performed in a 2 point configuration using V_{ac} = 10µV < k_BT and standard lock-in techniques. The effective mass in the direction of the wire is $m^*=0.33m_0$ in units of the free-electron mass leading to a stronger role for interactions at the same density. Samples are cooled down in a dilution refrigerator with an electron base temperature T = 100mK. The substrate and the cleaved-edge are illuminated at 10 K with two infrared light-emitting diodes.

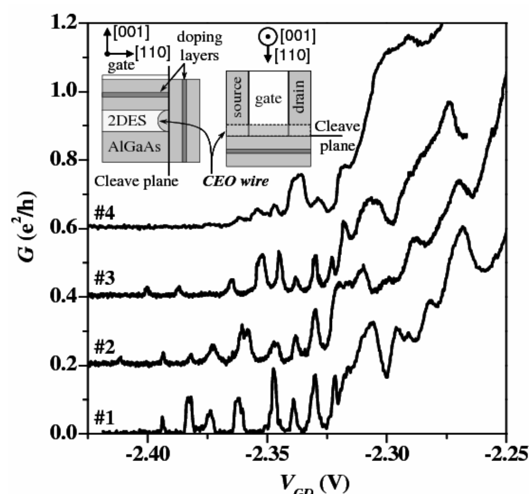

Fig. 1: *Conductance G vs. Gate bias VGD for several VGD sweeps in the positive-voltage direction at a base elctron temperature T = 100 mK. Beyond the fourth sweep it becomes increasingly difficult to resolve resonances. Each trace is offset by 0.2 e²/h for clarity. Inset : Schematic of the sample. In the right-hand side inset the wire running along the cleave plane underneath the gate is shown by the dotted lines.*

Fig. 1 depicts combs of conductance resonances at T=100 mK as the gate bias V_{GD} is scanned past the pinch-off threshold. The first V_{GD} sweep after illumination and at base T gives quasi-periodic resonances. Upon sweeping V_{GD} repeatedly in the same direction some resonances appear to be quite robust while others shift. By the fourth gate sweep most resonances have vanished and those remaining are lumped close to threshold. We interpret this behavior as Coulomb blockade (CB) in a disorder potential in analogy with its discovery in disordered Si wires. Presumably, cycling V_{GD} affects the distribution of ionized dopants underneath the gate, inducing variations in the potential background seen by the wire

[1]phone: +49-89-289-12778, fax: +49-89-3206620, email: dasgupta@wsi.tum.de

at each cycle. However by narrowing the gate bias window it is possible to preserve one resonance upon multiple V_{GD} cycles and perform a systematic study of it.

Now we study the non-linear conduction through the wire. In Fig. 2a, the differential conductance dI/dV_{SD} is shown on a color scale as a function of V_{GD} and V_{SD} at T =100 mK. Note that the vanishingly small resonances at V_{SD} =0 are not visible on this color scale. Near threshold, Coulomb diamonds highlighted in white are visible. Additional diamonds with a steeper dV_{GD}/dV_{SD} slope are observed at more negative V_{GD} (red dashed lines). Fig. 2(b) shows several dI/dV_{SD} vs. V_{SD} traces at fixed V_{GD} indicated by the vertical dashed lines in Fig. 2(a): a gap structure centered at V_{SD} =0 develops beyond pinch-off as T is lowered [Fig. 2(c)]. All features evolve smoothly, without any significant trapped charge events. Note how the condition of maximum resonant conduction at the center of the CB diamond ΔV_{GD} = 0 in Fig. 2(b) corresponds to a strong minimum in dI/dV vs. V_{SD} similar to previous observations in Si nano wires.

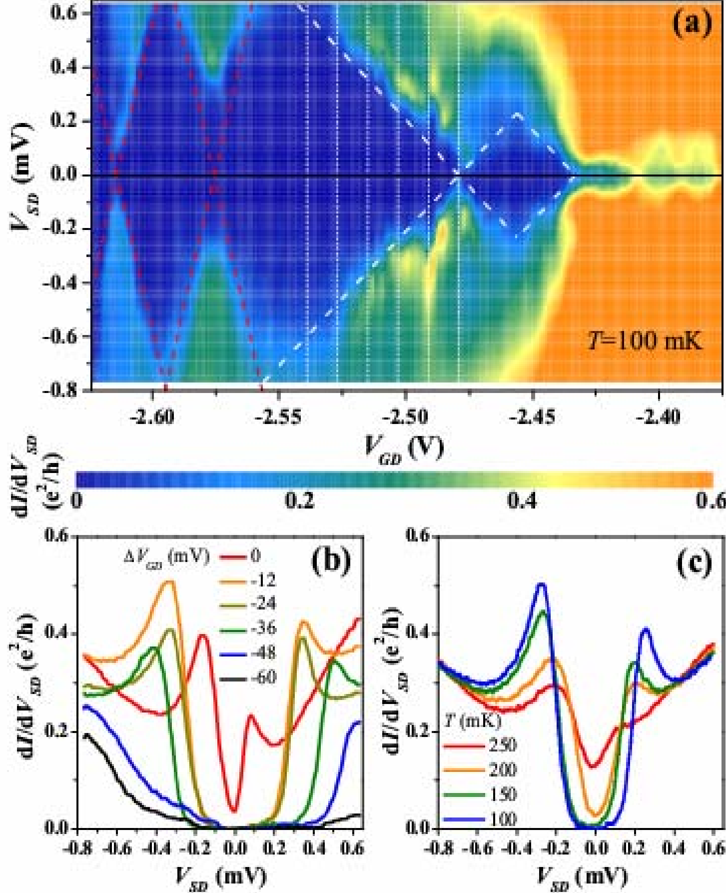

Fig. 2: (a) Differential conductance dI/dV_{SD} as a function of source-drain bias V_{SD} and Gate bias V_{GD} at T = 100 mK. (b) Subset showing traces at fixed V_{GD} indicated by the vertical dashed lines in (a). The conductance at ΔV_{GD} = 0 and V_{SD} = 0 corresponds to the maximum of a resonance peak. (c) Temperature dependence of dI/dV_{SD} at fixed V_{GD} ~ 50 mV from pinch off, taken from different data set.

These features can be explained by assuming that the disordered AlAs CEO wires break up into a series of weakly-coupled quantum dots at low electron density. This observation should prove useful for identifying transport mechanisms in similar large-mass, one dimensional disordered systems.

We gratefully acknowledge support from the COLLECT EC-Research Training Network, HPRN-CT-2002-00291 and BmBF grant 01 BM 470.

The ion sensitivity of surface conductive single crystalline diamond

Andreas Härtl[1], Stefan Nowy, José Antonio Garrido, and Martin Stutzmann

Since its first report in 1970 the ion-sensitive field effect transistor (ISFET) has become an important and versatile sensing tool. Useful modifications like the EnzymeFET (ENFET) or the ImmunoFET have expanded the number of possible applications to the broad area of biosensors, medical, and health care. Silicon, because of its technological advancement, is the most commonly used semiconductor material. But it is limited in its applications, mainly due to its instability in biological and chemical environments. The use of diamond for the development of ISFETs has been very limited, although this material offers a number of unique properties and could be very advantageous in this field.

Here, we describe recent progress in the understanding of the interaction of diamond with ions in an electrolyte.

Natural type-IIa single-crystal diamond samples (both 100 and 111 oriented) with a size of 3 by 3 mm and an average surface roughness below 0.5 nm were used for fabrication of ion sensitive devices. Hydrogen-termination of the diamond surface induces a p-type conductive channel, with typical values of $10^{-4}\ \Omega^{-1}\ cm^{-1}$, corresponding to hole densities of $10^{13}\ cm^{-2}$. Devices were fabricated by standard photolithography processing. The active area between source and drain contacts was defined by oxidizing the sample with an oxygen plasma, leaving just the active area hydrogen-terminated and conductive. Chemically resistant silicone glue was used to prevent contact between the metal contcts and the electrolyte, exposing only the active area to the solution.

The devices were measured as working electrodes in a three-electrode electrochemical cell, consistent of a double junction Ag/AgCl reference electrode and a Pt wire counter electrode. The experimental setup is designed for simultaneous recording of the drain–source current and voltage and the gate (electrolyte)–source voltage.

The drain–source current (I_{DS}) was recorded while the salt concentration of the electrolyte was changed by addition of defined salt quantities dissolved in buffer solution, in the range from 10 µM to 100 mM. The applied parameters were a constant drain–source voltage (U_{DS}) of −100 mV, and a constant gate-source voltage (U_{GS}) of −500 mV.

The drain–source current I_{DS} decreases upon an increase of the concentration of different monovalent salts, as can be seen in Fig.1. This drain–source current decrease indicates a major influence of the positively charged cations: an increased amount of positive charge at the interface leads to a depletion of the hole accumulation layer close to the diamond surface and, as a consequence, to a decrease in drain–source current. The predominant role of the cations in the ion sensitivity of diamond ISFETs becomes evident from Fig. 1, which compares the effect of two different salts (KCl and $CaCl_2$). Both salts consist of the same anion (Cl^-) but differ in the cation, the monovalent K^+ and the divalent ion Ca^{2+}. Due to the two-fold positive charge, a larger influence on the conductivity is expected for divalent cations. Indeed we find experimentally a much larger sensitivity to the salt containing the divalent cation, confirming the major influence of the cation.

The interaction of positive ions with the diamond surface can be basically explained by two effects: screening and specific adsorption. On the diamond film, a hole accumulation layer is formed just underneath the hydrogen-terminated surface. Ions from the electrolyte maintain the overall charge neutrality. A layer of specifically bound (non hydrated) ions

[1]phone: +49-89-289-12768, fax: +49-89-289-12737, email: haertl@wsi.tum.de

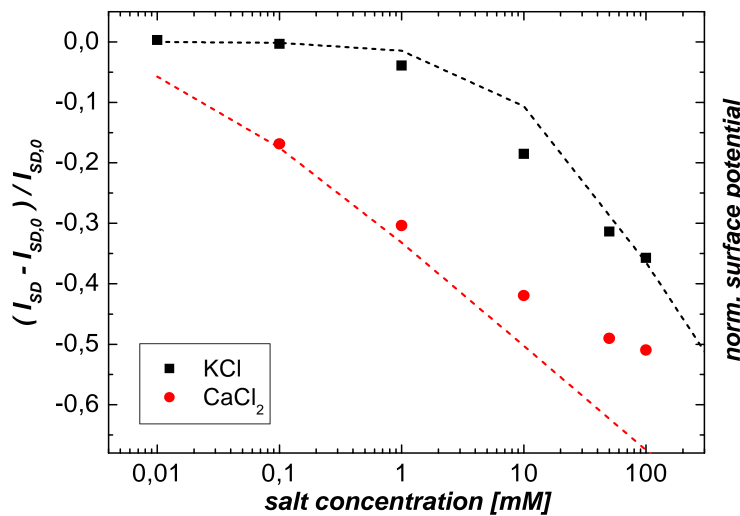

Fig. 1: *Effect of different salt concentrations on the source-drain-current (dots) and surface potential (calculation based on the Grahame equation).*

from the electrolyte forms close to the surface (at the inner Helmholtz-plane). A second layer of unspecifically bound (hydrated) ions from the solution shapes the outer Helmholtzplane. Finally, there is the extended region of diffuse charges. The potential profile over the interface (Fig. 2) starts from a positive value (hole accumulation layer with applied positive potential), then strongly drops to negative values (countercharge layer) and finally slowly rises exponentially to zero (diffuse layer).

Positive ions from the solution will partially screen the potential induced by the negative surface adsorbates, resulting in a reduced negative potential.

A second possibility to understand the effect of the electrolyte ionic strength is the specific adsorption of the positively charged cations at the surface. Possible binding sites are amphoteric oxygen groups, always present even at the H-terminated surface due to imperfections of the hydrogenation (as verified by XPS and contact angle measurements). In addition, specific adsorption can also directly occur on the hydrogenated regions.

These experiments suggest that a negative potential is present at the diamond / electrolyte interface. The nature of the negatively charged ions adsorbed on the surface is currently under discussion: anions from the buffer salt or hydroxide ions could be responsible for the negative surface charge.

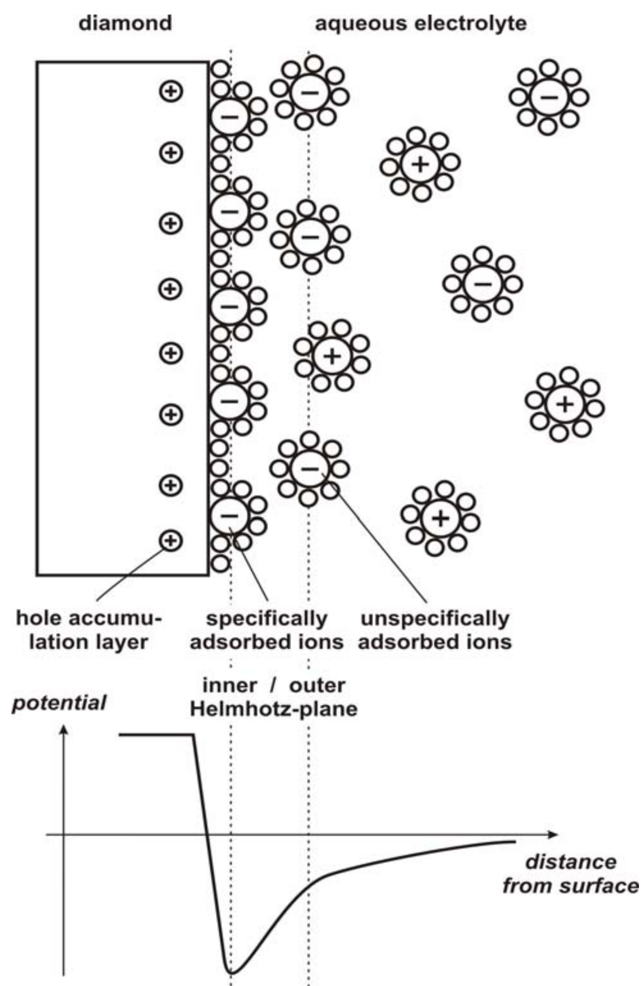

Fig. 2: *Diamond / electrolyte interface: ion distribution and potential.*

supported by Deutsche Forschungsgemeinschaft SFB 563, B15

Electronic and optical properties of boron-doped nanocrystalline diamond

Wojciech Gajewski[1], José Antonio Garrido Ariza, and Martin Stutzmann

Due to the recent progress in diamond CVD films, nanocrystalline diamond films (NCD) have received considerable attention, and are expected to play an important role for future diamond electrochemical and bioelectrochemical applications. Much attention has been devoted to optimizing the growth process, resulting in films with a smooth surface and grain sizes raging from 5 to 100 nm. However, there is so far not enough information concerning bulk and surface properties such as unintentional and intentional dopants, as well as surface states. We investigate the optical and electronic properties of boron-doped nanocrystalline diamond (B-NCD) thin films with thicknesses below 350 nm. NCD films with dopant gas concentrations ranging from 0 to 5000 ppm trimethyl boron (TMB) were grown on quartz substrates by CH_4/H_2 plasma CVD.

Hall effect measurements confirm the expected p-type conductivity of highly boron-doped samples (2500-5000ppm). The conductivity of samples with low boron concentration (3-150 ppm) in the gas phase strongly depends on temperature, however at higher boron doping (5000 ppm), the conductivity and the carrier concentration are only weekly temperature dependent, and the samples exhibit quasimetallic properties (*Fig. 1a)*.

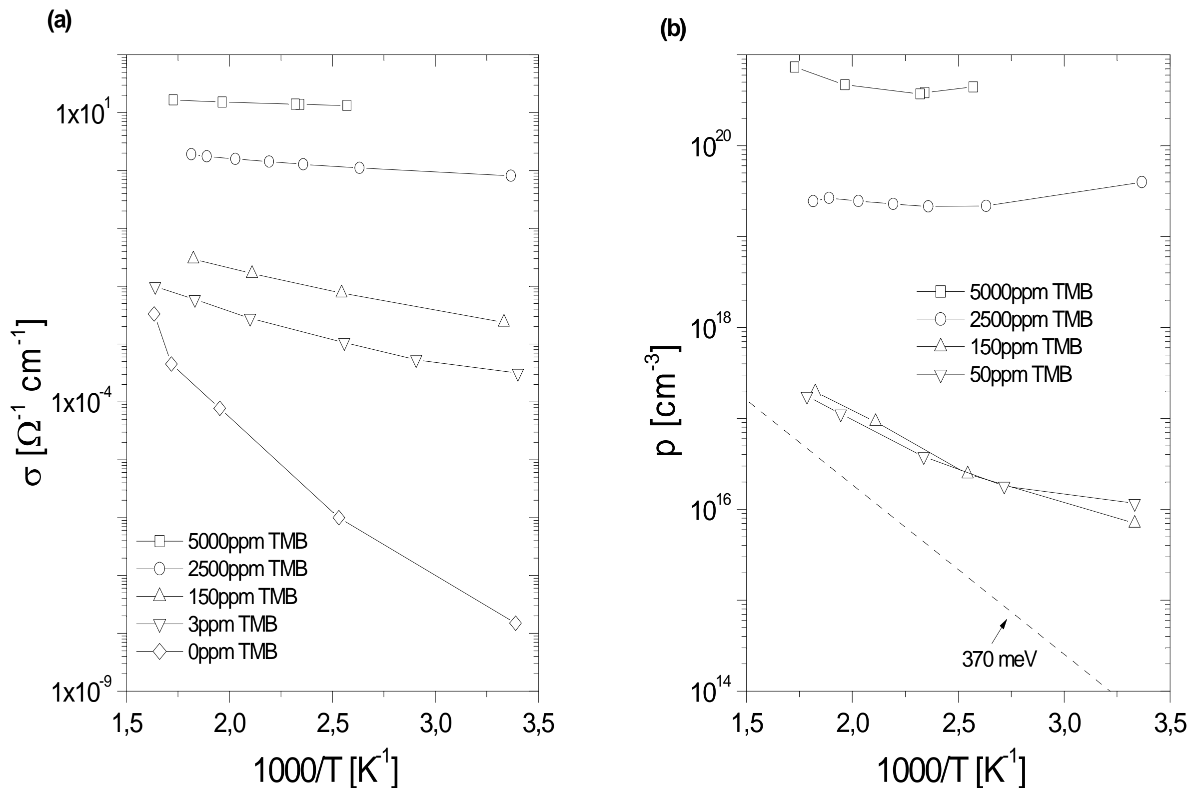

Fig. 1: *(a) Temperature dependence of the conductivity of boron-doped NCD*
(b) Temperature dependence of the carrier concentration

[1]phone: +49-89-289-12774, fax: +49-89-289-12739, email: gajewski@wsi.tum.de

The Hall mobility shows no clear temperature dependence. As expected, the higher the carrier concentration (*Fig. 1b)*, the lower the mobility. At low boron doping (50 ppm) the mobility is 2 $cm^2V^{-1}s^{-1}$, while at high boron doping (5000 ppm) the mobility decreases down to 0.2 $cm^2V^{-1}s^{-1}$. Substitutional boron acceptors in single and polycrystalline diamond are known to introduce a well defined energy level about 370 meV above the maximum of the valance band. Suprisingly, such a distinct acceptor level is not observed in the haole density data raising the question about the origin of the conductivity.

Spectrally resolved photocurrent (SPC) measurements were performed for undoped and low boron-doped samples (0-150 ppm). They reveal a strong dependence of the photosignal on the surface termination, suggesting significant contribution from surface states on the electronic properties of B-NCD. Major differences occur in the energy range 3.5 – 5.4 eV, where a pronounced photoconductivity onset at 4 eV is observed only in boron-doped "as grown" and H-plasma treated samples (*Fig. 2a)*. Oxygen-plasma treatment results in a remarkable change of the photocurrent spectral response in the high energy range (*Fig. 2a)*. After oxidation, the photocurrent spectrum only shows the indirect band gap absporption of diamond at about 5.3 eV. The spectrum of the non-intentionally doped films shows a prominent absorption slightly below 1 eV, which could be related to the contribution of grain-boundaries. In the case of the 150 ppm B-doped film, the photocurrent onset is shifted to lower energies, in agreement with the formation of an impurity band as suggested by the conductivity data.

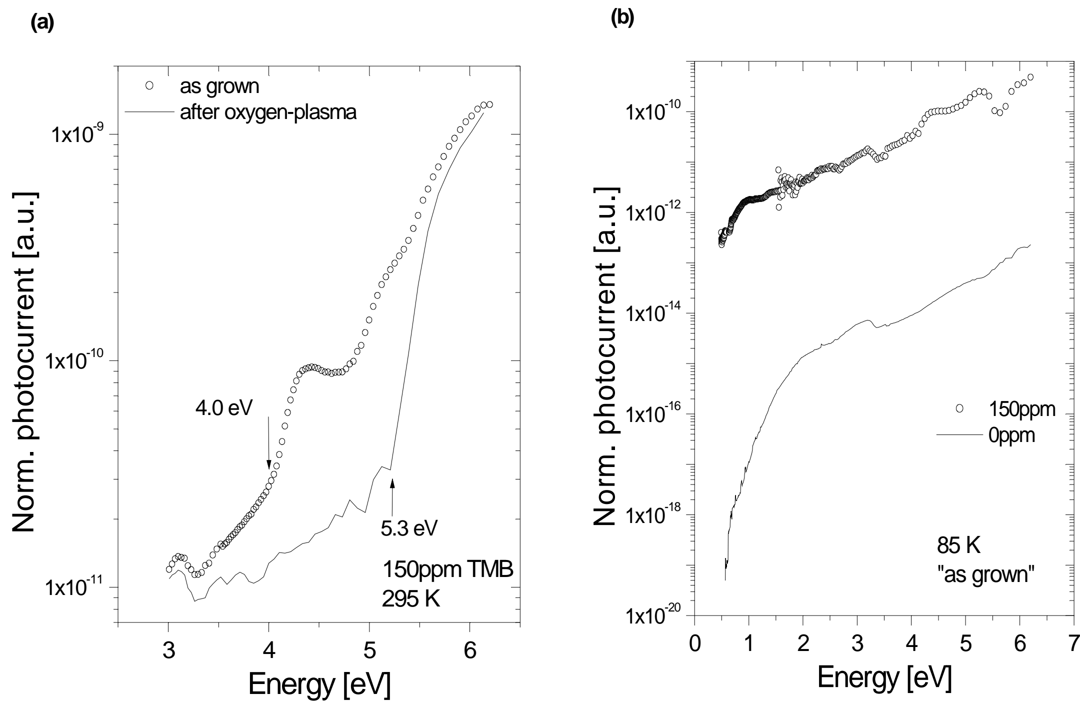

Fig. 2: *(a) Spectral response of photocurrent measured in a 150ppm B-doped NCD sample"as grown and after O-plasma (b) Spectral response of photocurrent measured in a 150ppm B-doped and non-intentional* NCD sample.

---

supported by the 6th Framework EU Marie-Curie Research and Training Network:
DRIVE - "Diamond Research on Interfaces for Versatile Electronics"

Spin dynamics of optically stimulated charges in InGaAs self-assembled quantum dots

D. Heiss[1], S. Schaeck, M. Kroutvar, H. Huebl, M. Lunz, M. Bichler, D. Schuh, M. S. Brandt, G. Abstreiter, and J. J. Finley

Technological advances in crystal growth and nanofabrication have led to an upsurge of interest in quantum dots (QDs) for which the motion of charge carriers is fully quantized in all three spatial directions. The complete absence of any motional degrees of freedom gives rise to an energetically discrete electronic structure that fundamentally modifies the physics of these nanoscale objects and strongly influences their optical and electrical properties. These properties can be tailored during fabrication facilitating the investigation and engineering of quantum effects in finite low-dimensional systems that were hitherto largely unexplored. When combined with the ability to tune their optical and electronic properties by applying controlled perturbations, individual quantum dot devices may provide a route towards quantum coherent devices for use in quantum information science [1].

We investigated the spin dynamics of optically stimulated charges in such self-assembled QDs. For these experiments we use spin memory devices, depicted in figure 1, that enable selective optical generation, storage and readout of the spin orientation of either single electrons or holes in InGaAs-GaAs self assembled quantum dots [2]. This device operates by frequency selective optical charging of a sub ensemble of dots via polarized optical excitation and subsequent selective exciton ionization using an internal electric field. The reversible transfer between optical polarization and spin orientation allows to control and probe the spin state of the stored charge. After a variable delay time, the spin polarization is tested by electrically re-injecting the complementary charge carriers into the dots and analyzing the polarization of the resulting electroluminescence storage signal.

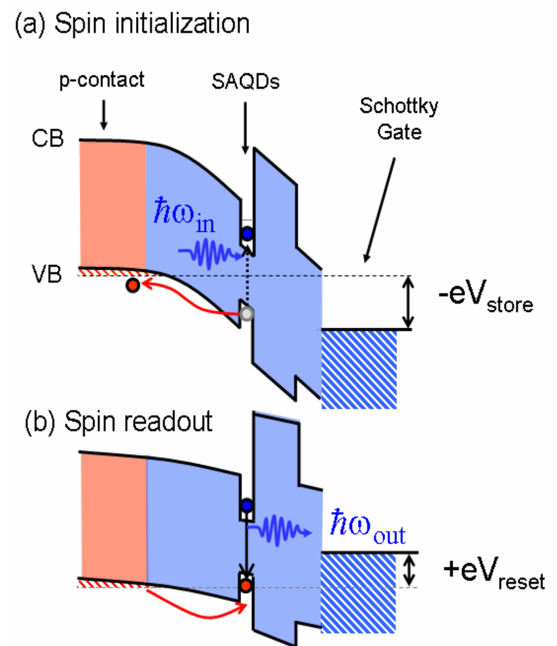

Fig. 1: *Bandstructure and operating principles of the electron spin memory devices*

Recently we reported studies of the longitudinal *electron* spin lifetime (T_1) as a function of Zeeman energy, lattice temperature and orbital quantization energy [2,3]. These measurements revealed extremely long spin lifetimes around 20ms (B=4T, T=1K) and a power law dependence $T_1 \propto B^{-4}T^{-1}$ characteristic for spin relaxation due to single phonon scattering processes [4]. Further support for this conclusion is obtained by examining the dependence of the spin lifetime on the QD emission energy. This data is presented in Fig. 2, revealing a pronounced shortening of T_1 from ~300 to ~30 μs as the detection energy re-

---

[1]phone: +49-89-289-12784, fax: +49-89-3206620, email: heiss@wsi.tum.de

duces from 1.3 to 1.26 eV. A reduction of the detection energy indicates that we are probing larger quantum dots for which the effects of motional quantization are weaker. Thus, one expects that the s-p level splitting $\hbar\omega_{sp}$ should increase with the detection energy as depicted schematically on Fig. 2. Over this comparatively small (ΔE ~40 meV) range of detection energies we observe a tenfold increase of the spin lifetime with increasing detection energy. This observation lends support to the idea that linear spin–orbit interaction mediated by single phonon scattering processes determines the spin lifetime in self-assembled quantum dots. Moreover, it suggests that the spin in self-assembled QDs could be more stable against scattering when compared with electrostatically defined dots for which the motional quantization energies are much smaller in the range of a few meV.

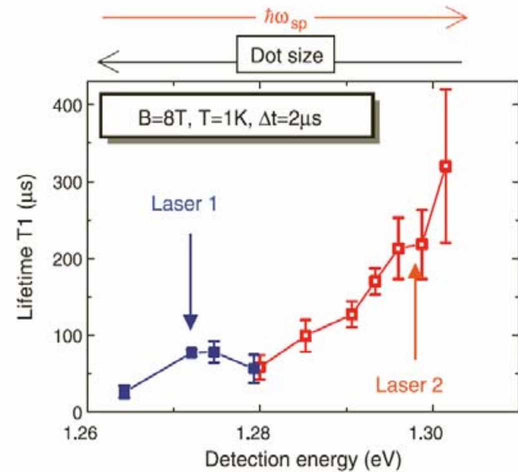

Fig. 2: *Detection energy dependence of longitudinal electron spin relaxation time*

Motivated by the success of this experimental technique and such long spin-lifetimes, we are currently modifying our setup to allow the application of microwave pulses during the storage phase. This opens up the possibility to investigate spin decoherence processes by driving optically generated electron spins with microwave pulses. Optically detected spin echo measurements will then be performed to measure the transverse electron spin lifetime (T_2^*)

In addition, over the past year we have extended our investigations to a modified device design that enables investigation of the relaxation dynamics of optically generated *holes*. In the context of quantum information processing, fully localized holes may be advantageous due to the p-like character of their Bloch wavefunction that inhibits coupling to the nuclear spin system. In strong contrast to the electron storage experiments, first measurements on hole storage samples reveal no significant optical polarization memory effect for storage times shorter than ~1μs and magnetic fields up to 12T. These findings contrast strongly with our results for electrons, indicating that the hole spin decays over much faster timescales. The hole T_1 time in QDs has been controversially discussed in the literature; some theories indicating that it can be comparable to, or even longer than for electrons whilst others predict several orders of magnitude faster relaxation [5].

This work is supported financially by the DFG via SFB 631 - Teilprojekt B1.

[1] D. Loss,D. P. DiVicenzo, PRA 57 (1998),
[2] M. Kroutvar et al., Nature 432 (2004),
[3] D. Heiss et al., Solid State Communications 135, 591, (2005),
[4] A. V. Khaetskii and Y. Nazarov. PRB 64 (2001),
[5] See e.g. D. Bulaev et al. , PRL 95 (2005) and L. Woods et al., PRB 69 (2004)

---

supported by DFG via SFB 631 - Teilprojekt B1.

Optical spectroscopy of individual quantum dot molecules

Hubert J. Krenner, Emily C. Clark[1], Matthias Sabathil, Toshihiro Nakaoka, Max Bichler, Christoph Scheurer[2], Gerhard Abstreiter, and Jonathan J. Finley

Charge and spin excitations in semiconductor quantum dots (QDs) have been proposed as an attractive system for the implementation of quantum bits for solid-state quantum information processing. Vertically correlated multi-layer structures of self-assembled QDs fabricated in the In(Ga)As/GaAs material system provide an inherently scalable architecture for semiconductor spin and exciton based quantum bits.

Recently, we reported the direct observation of coherent coupling of charge neutral single excitons in individual self-assembled quantum dot molecules (QDMs). We investigated individual pairs of vertically stacked self-assembled QDs forming a QDM which are embedded in a *n-i*-Schottky diode. By applying a bias voltage between the doped back contact and the semitransparent gate electrode we can tune the static electric field (*F*) along the QDM axis. Figure 1 (a) shows typical micro-photoluminescence (PL) spectra recorded from an individual QDM as a function of *F*. Two prominent peaks, X_A and X_B, are resolved in the spectra which exhibit a clear anti-crossing as the electric field is tuned [1]. In QDMs two exciton species can be distinguished: Spatially *direct* (*e* and *h* in the same QD) and *indirect* (*e* and *h* in different QDs). Direct excitons are optically active due to their high *e-h* overlap whereas indirect excitons are not optically active. In addition, they differ in the excitonic dipole moment: The dipole moment of direct excitons is similar to single QDs. In contrast, indirect excitons have a much larger dipole moment determined by the inter-dot separation $p_{ind} = e \cdot d$. Therefore, the Stark shift $(\Delta E = p \cdot F)$ is weak and quadratic for direct excitons and strong and linear for indirect excitons. This enables tuning of these exciton species by the electric field. With increasing *F* the indirect exciton with the hole localized in the upper QD shifts towards the direct exciton localized in the upper QD.

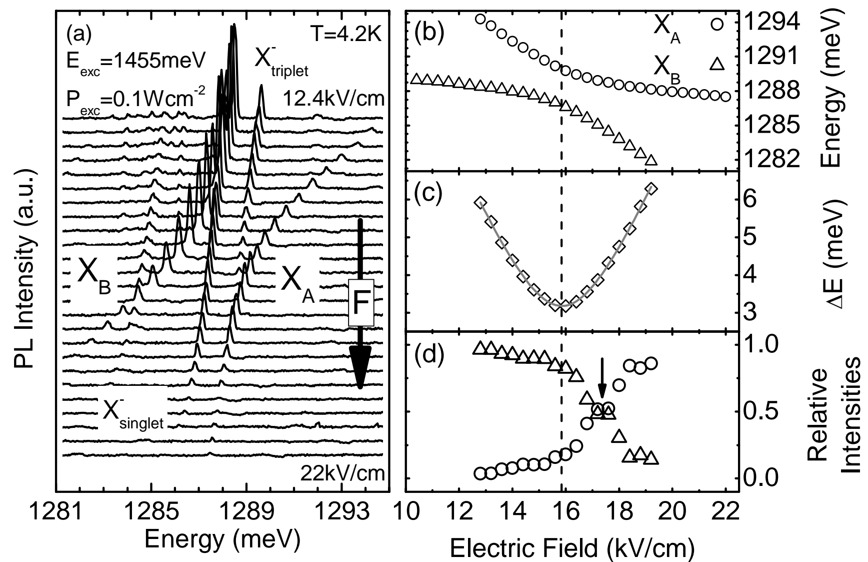

Fig. 1*: (a) PL spectra of an individual QD molecule. Extracted peak positions of* X_A *and* X_B *(b), energy splitting (c) and the relative intensities of* X_A *and* X_B*. The arrow marks the electric field at which equal relative intensities are observed.*

[1]phone: +49-89-289-12784, fax: +49-89-320 6620, email: clark@wsi.tum.de
[2]Lehrstuhl für Theoretische Chemie, TU München, email : christoph.scheurer@ch.tum.de

At the resonance field F_{crit} the electron part of the exciton wavefunction hybridizes into bonding and anti-bonding molecular states split by the coupling energy $2\Delta E_{e-e} = 3.2meV$ giving rise to the observed anti-crossing. For $F>F_{crit}$ the nature of the groundstate develops form direct to indirect character leading to the pronounced quenching behavior of the PL signal of branch X_B. Figures 1 (b)-(d) show a detailed analysis of the PL data of this QDM. Whereas the minimum energetic splitting is observed at F_{crit}=15.8kV/cm, the electric field at which equal relative intensities are detected is found to be greater than F_{crit}. This shift can be explained by efficient population relaxation between the two coupled exciton levels on timescales faster than the radiative lifetime.

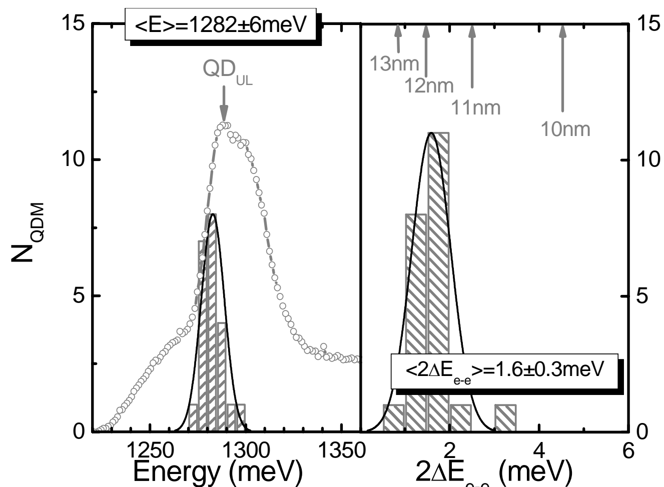

***Fig. 2**: Statistical analysis of more than 25 QDMs. Left panel: Center energies of more than 25 QDMs compared to the ensemble spectrum. Right panel: Experimental (histogram) values for $2\Delta E_{e-e}$ and calculated splittings for different inter-dot separations (arrows).*

We observed similar behavior for more than 25 QDMs demonstrating that these anti-crossings are a general fingerprint for a tunable coupled QD system [2]. Furthermore, a statistical analysis was performed on the observed center emission energies between the two anti-crossing branches and the minimum energetic splitting $2\Delta E_{e-e}$ i.e. the electron coupling energy. According to our theoretical model the observed anti-crossings occur between excitonic states with the hole localized in the upper QD. On the left panel of Figure 2 we compare the histogram of the center energies of the observed anti-crossings to the ensemble PL spectrum of ~10^6 QDMs recorded from the same sample piece. In this spectrum the signal of upper, more homogeneous QD layer can be identified as a narrow peak (QD_{UL}) on a broad background of the seed layer of QDs. The distribution of the center energies overlaps well with the ensemble PL of the upper layer confirming the assumption that the observed anti-crossing occur between excitons with the hole localized in the upper QD. Furthermore, in the right panel of Figure 2 we analyzed the coupling energies and found a mean value $\langle 2\Delta E_{e-e} \rangle = (1.6 \pm 0.3)meV$. The arrows in the figure mark the calculated coupling energies for QD separations ranging from 10 to 13nm. The experimentally obtained value corresponds to $d = (11.9 \pm 0.6)$ nm which compares well to 10nm as nominally set during MBE growth.

[1] H. J. Krenner, M. Sabathil, E. C. Clark, A. Kress, D. Schuh, M. Bichler, G. Abstreiter, and J. J. Finley, Physical Review Letters **94**, 057402 (2005)

[2] H. J. Krenner, S. Stufler, M. Sabathil, E. C. Clark, P. Ester, M. Bichler, G. Abstreiter, J. J. Finley, and A. Zrenner, New Journal of Physics **7**, 184 (2005)

---

supported by DFG via Sonderforschungsbereich 631, Teilprojekt B5

Semiconductor Materials Science and Technology

High mobility two dimensional hole gases on (110) GaAs substrates and cleave facets

Ying Xiang, Sebastian Roth[1], Nebile Isik, Max Bichler, Frank Fischer, and Matthew Grayson

High mobility two dimensional hole gases (2DHG) in GaAs are of increasing interest due to their spin-orbit coupling and their heavy mass. In recent years, high quality 2DHG's in modulation doped heterostructures have been fabricated for transport studies on the (110) GaAs surface using Si as an acceptor using modulated growth conditions for the *p*-type layer. [1] However, this technique needed to be optimized to achieve highest mobility, and the possibility of fabricating such a system on the cleave facet, called cleaved-edge overgrown (CEO), needed to be explored. In this report, 2D hole systems on (110) substrates are optimized and demonstrated at cleaved edge with a novel 4-point geometry. [2]

First, we consider high mobility (110) samples which are grown on an undoped GaAs substrate with 3000 Å thickness. It is covered by a $GaAs/Al_{0.3}Ga_{0.7}As$ superlattice with thickness of 79.24 Å and 22.64 Å. After growing the superlattice, 5000 Å GaAs, an AlGaAs with spacer thickness of 800 Å and a 20 Å Si-doped AlGaAs layer are grown. After that an AlGaAs layer with 3000 Å thickness is overgrown, topped by a 100 Å thick GaAs cap layer for oxidation protection.

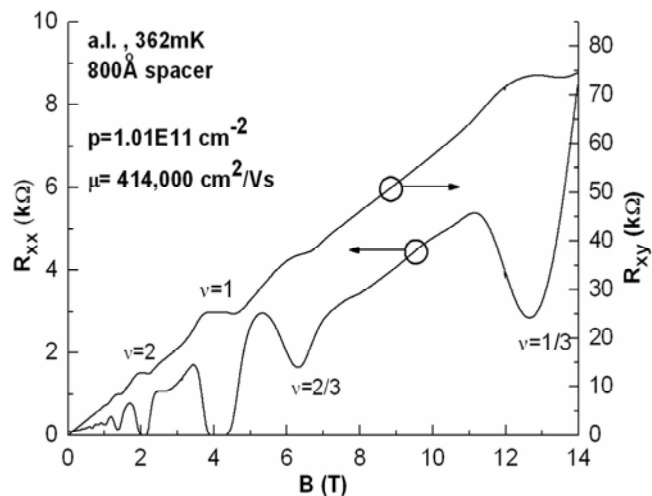

Fig. 1: *The longitudinal R_{xx} and Hall R_{xy} resistance measurements of high mobility modulation doped p-type sample at 362 mK.*

Figure 1 shows the longitudinal, R_{xx}, and Hall, R_{xy}, resistance measurements of the highest mobility *p*-type sample, which were carried out at 362 mK. The density of the sample deduced from Shubnikov-de Haas oscillations is p = 1.01×10^{11} cm^{-2}. The mobility of the sample fabricated at 800 Å thick spacer and at 10.2 Å optimum doping thickness is $\mu = 4.14 \times 10^5$ cm^2/Vs. The quantum Hall minima at integer and fractional filling factors (ν) are clearly seen in the Fig. 1. The evidence of fractional quantum Hall features demonstrate the quality of the sample.

The density dependent transport measurements have been investigated in the two orthogonal transport directions, $[1\bar{1}0]$ and $[001]$. An L-shaped Hall bar and gate mask was designed as shown in the inset of Fig. 2. The mobility anisotropy of two directions $[1\bar{1}0]$ and $[001]$ was investigated using a similar structure and is plotted in Fig. 2. The data in Fig. 2 show an increase of anisotropy with increasing hole density. We observed that the mobility along the $[1\bar{1}0]$ direction is about a factor of 1.5 larger than the mobility along the $[001]$ direction at higher densities. The increase of anisotropy with increasing carrier density may be related by the interface roughness anisotropy or to the different effective mass

[1]phone: +49-89-289-12736, fax: +49-89-289-3206620, email: roth@wsi.tum.de

in the two directions. On the other hand, very weak anisotropy at lower hole densities ($p < 7x10^{10}cm^{-2}$) is observed.

Second we study the growth and characterization of optimized *p*-type CEO samples. An undoped 4 µm GaAs layer, 3000 Å p^- and 7000 Å and p^+ doped GaAs are overgrown. The p^+/p^- layers are patterned in ~ 10 µm wide fingers which extend to the cleave plane function as ohmic contacts. After in situ cleaving this substrate, a 100 Å thick $[1\bar{1}0]$ GaAs layer is grown. It is followed by 800 Å spacer, 20 Å *p*-type modulation doping and 3000 Å thick barrier AlGaAs layers and 100 Å thick GaAs cap layer.

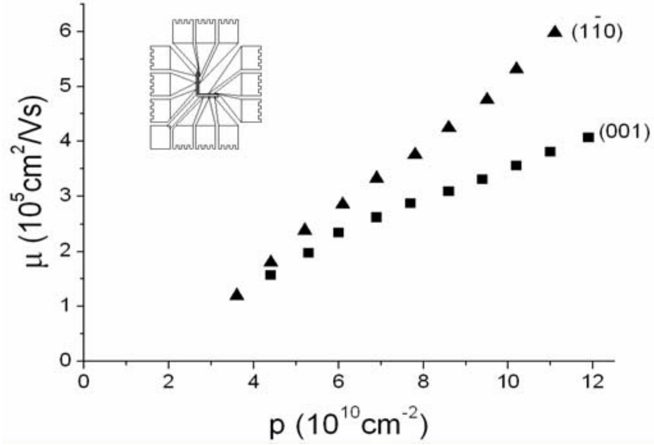

Fig. 2: *Density dependent ratio of the mobilities in* $[1\bar{1}0]$ *and* $[001]$ *direction. Inset: a new L-shaped Hall bar designed for such density dependence transport measurements.*

The longitudinal, R_{xx}, magnetoresistance of the *p*-type CEO sample measured at 380 mK is shown in Fig. 3. The density is determined using the minima at ν = 1 and ν = 2. A fractional quantum Hall effect feature is visible at ν = 2/3. The obtained mobility is $\mu = 7.6x10^4$ cm^2/Vs which is only a factor of 3 smaller than the highest mobility modulation doped *p*-type (110) sample.

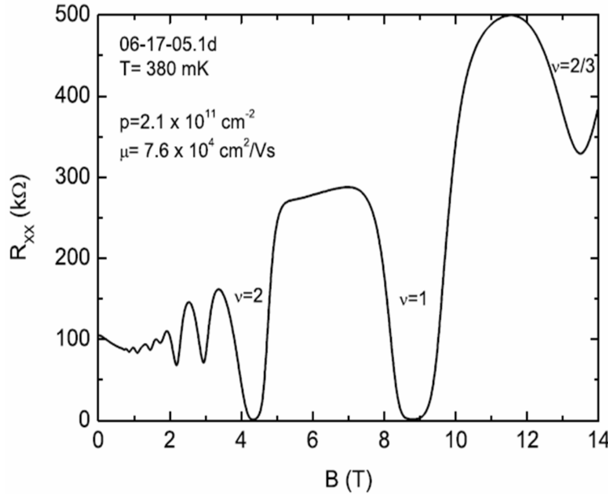

Fig. 3: *The longitudinal resistance measurement of optimized p-type CEO sample at 380 mK.*

In conclusion, we characterized a modulation doped 2D hole samples on (110) oriented GaAs. R_{xx} measurements at low temperature show the fractional quantum Hall effect. We also investigate density dependence the mobility of the sample. The results show the mobility anisotropy increases with increasing carrier density. We grow and characterize *p*-type CEO samples. We also observed fractional quantum Hall effect in R_{xx} measurements. However, we found that the CEO *p*-type samples have lower mobility than the modulation doped substrate.

[1] F. Fischer, D. Schuh, M. Bichler, G. Abstreiter, M. Grayson, and K. Neumaier, Appl. Phys. Lett. **86**, 192106 (2005)
[2] M.Grayson, S. F. Roth, Y. Xiang, F. Fischer, D. Schuh, and M. Bichler, Appl. Phys. Lett. **87**, 212113 (2005)

---

supported by the DFG via SFB 631 and Schwerpunktprogramm Quanten-Hall-Systeme, and BMBF project 01BM912.

Transport in a vertical quantum wire fabricated with cleaved-edge overgrowth

Sebastian Roth[1], Matthew Grayson, Max Bichler, Dieter Schuh, and Gerhard Abstreiter

An elegant technique for fabricating clean one-dimensional (1D) quantum wires is cleaved-edge overgrowth (CEO). Ballistic transport and optical properties of such edge wires have been studied. It was also demonstrated with CEO, how an atomically sharp modulation of the substrate potential can be transferred to an adjacent two-dimensional electron system (2DES) to create artificial minibands. If a twofold application of CEO were to create a 1D wire, this could likewise be precisely modulated by a substrate potential. In principle, 1D transport structures with epitaxially defined single or multiple barriers can be realized. The work below describes evidence of the first successful realization of such a vertical wire structure.

A substrate and two crystal cleaves define the vertical orientation of the wire. Figure 1a shows the design of the substrate and the first CEO. The second CEO takes place on the front facet. First, a (001) substrate is overgrown vertically with layer sequence. The sequence starts with a 1 µm n^+ doped GaAs bottom-contact, followed by a GaAs layer, a $Al_{0.3}Ga_{0.7}As$ layer and another GaAs layer, each 2 µm thick. A 1 µm n^+ top-contact completes the substrate. The top-contact is patterned with photolithography and partly etched away, leaving eight freestanding n^+ finger-contacts. Second, the (110)-facet is cleaved and then overgrown with a gated 2DES (I) structure. The structure consists of an 8 nm wide GaAs quantum well, a 0.55 µm barrier of $Al_{0.3}Ga_{0.7}As$ containing a Si-δ-doping at a spacer distance of 50 nm and a n^+-sidegate to control the 2D density. The substrate barrier modulates the density of 2DES I, both because the quantum confinement is increased adjacent to the barrier and because charged defects in the $Al_{0.3}Ga_{0.7}As$ can reduce the density next to the barrier. We call this region 2DES I^*.

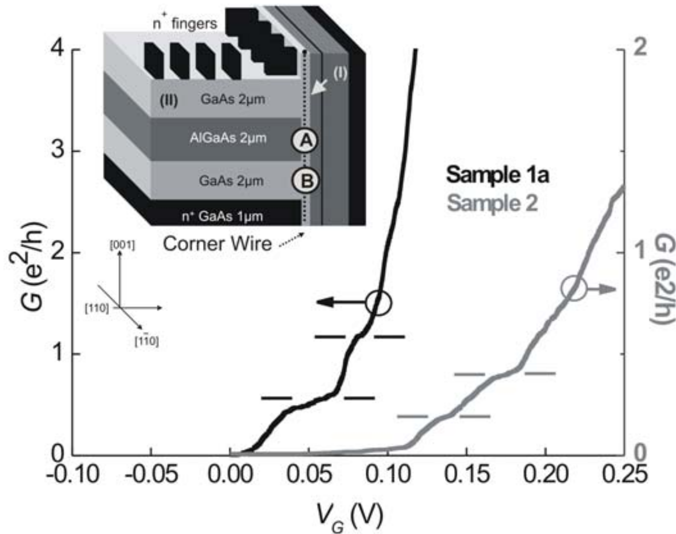

Fig. 1: *The conductance of Samples 1a and 2 along the anticipated wire exposes steps between 0 V and 0.2 V of sidegate bias V_G. Inset: The double-cleave sample. The second CEO is in the plane of the front facet.*

We quantify the density modulation of 2DES I and I^* with four-point magnetoresistance measurements using the n^+ finger-contacts. Figure 2a and the inset show the longitudinal resistance R_{xx} of 2DES I in a perpendicular magnetic field B at 300 mK. Shubnikov-de-Haas (SdH) oscillations prove the high growth quality. At a sidegate bias V_G = 0.0 V only the high density n_I of 2DES I contributes to the oscillations and the resistance minima occur at integer filling factors ν,

[1]phone: +49-89-289-12736, fax: +49-89-3206620, email: roth@wsi.tum.de

while 2DES I* is depleted. The density is deduced to be $n_I = 2.15 \times 10^{11}\text{cm}^{-2}$ after illumination and a corresponding mobility of $\mu_I = 2.6 \times 10^4$ cm²/Vs is calculated from R_{xx} at zero magnetic field. The density n_I can be changed with sidegate bias. At $V_G = 0.8$ V the zero field resistance drops more than three orders of magnitude, because 2DES I* becomes conductive and shorts 2DES I to the bulk doped bottom contact. Further, new minima appear and reflect the density of 2DES I*. These minima are related to integer filling factors ν^* corresponding to a density n_I^*.

To accumulate 1D states at the edge of 2DES I, the $(1\bar{1}0)$-facet is cleaved and then overgrown with a modulation doped barrier. This heterostructure consists of 0.32 µm $Al_{0.3}Ga_{0.7}As$ with Si-δ-doping after a 20 nm spacer, and topped with a 20 nm GaAs cap. The accumulation potential also induces a second 2DES (II) in the GaAs substrate layers at the second cleave plane. Since the second cleave does not include a quantum well, 2DES II is split by the substrate $Al_{0.3}Ga_{0.7}As$ barrier. The SdH oscillations are measured again in a four-point geometry and shown in Fig. 2b. The density of 2DES II after illumination is $n_{II} = 4.3 \times 10^{11}$ cm^{-2}, much higher compared to the density of 2DES I at $V_G = 0.0$ V, due to a higher doping concentration in the δ-layer and the smaller spacer. The mobility $\mu_{II} = 2.9 \times 10^4$ cm²/V s of is similar to μ_I on the first cleave facet.

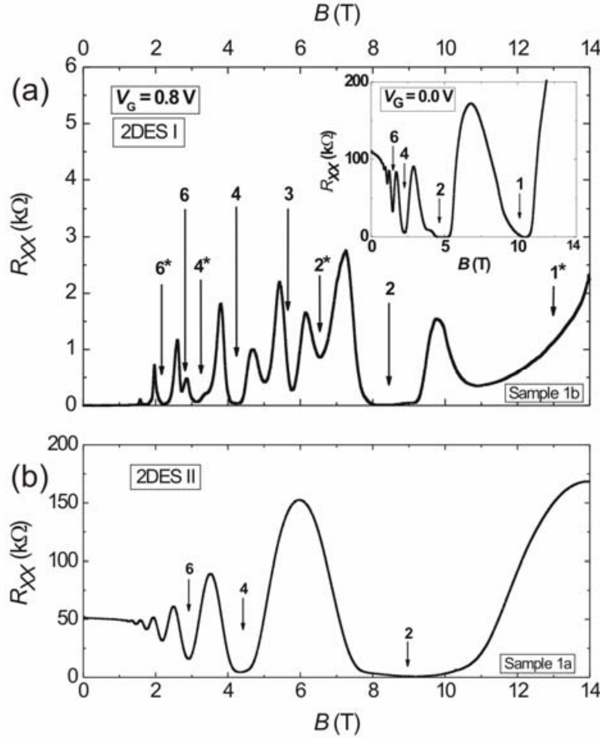

Fig. 2: *Shubnikov-de Haas oscillations of 2DES I (a) for $V_G = 0.8$ V and $V_G = 0.0$ V (inset) and 2DES II (b)*

The conductance along the vertical wire is quantized with changing sidegate bias. An ac-voltage of 100 µV is applied between a top finger-contact and the bottom contact. The current is measured with a lock-in amplifier at the excitation frequency of 17 Hz, while the sidegate voltage is sweeped. In Fig. 1b the conductance of Sample 1a after illumination is zero at a gate voltage of $V_G = 0$ V, but rises to a plateau value of about $0.3 \times G_0$ between $V_G = 0.03$ V and $V_G = 0.07$ V. A second plateau appears at $0.6 \times G_0$ between $V_G = 0.07$ V and $V_G = 0.09$ V, indicating 1D transport. Similar behaves Sample 2, with the conductance onset shifted to a slightly higher gate voltage and lower plateau values. The plateaus in both samples are strongly suppressed from G_0, due to the 2D lead resistance as well as possible 2D-1D scattering at the accumulation edge. The sidegate not only controls the occupation of the quantum wire, but also changes the 2D lead resistance continuously, so no constant series resistance can be substracted as in split gate wires.

---

supported by BMBF Project 'NanoQuit' 01BM469 and DFG Ab 35/4 & 35/5

Optical and magneto-transport properties of electrically gated CEO semiconductor nanostructures

Emanuele Uccelli[1], Johanna Simon[2], Jochen Bauer, Max Bichler, Anna Fontcuberta i Morral, Matthew Grayson, Jonathan Finley, and Gerhard Abstreiter

The ability to precisely control the growth of self-assembled semiconductor quantum dots is a topic that has recently attracted significant interest worldwide. Today, In(Ga)As and In(Al)As Stransky-Krastanov grown dot layers on GaAs or AlAs with reasonably well defined emission energy, dot density and size homogeneity can be obtained. However, to date it has been much more difficult to controllably position individual self-assembled quantum dots on the growth surface. Here, we apply the cleaved-edge-overgrowth technique (CEO) in two different ways for an ultimate position control of quantum dots (QD).

The first approach is based on the selective growth of InAs QD on AlAs (110) with respect to GaAs(110). As indicated in Fig. 1, a series of AlAs layers with different thicknesses are deposited on an [001] orientated GaAs substrate, separated by GaAs. This substrate is then cleaved in situ in ultra high vacuum, exposing an atomically clean (110) surface is used for the subsequent growth of InAs QD, which form a chain on the AlAs strips as shown by Atomic Force Microscopy measurements in Fig 1b.

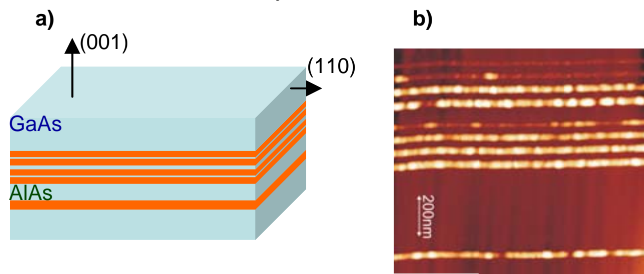

Fig. 1a) *Schematics of the CEO process for the realization of a well-ordered array of Quantum Dots.* ***b)*** *AFM measurement of an obtained QD array.*

We plan to deposit InAs QD on an isolated AlAs stripe and subsequently evaporate a thin and narrow (~500nm) Ta-gate over the heterostructure, as depicted in Fig.2, in order to split the buried AlAs 2DEG in two separated electron reservoirs. Electric transport can occur only through the chain of dots at the edge. In this way one can investigate the magneto-transport characteristics of electrons in a coupled array of self-assembled QDs.

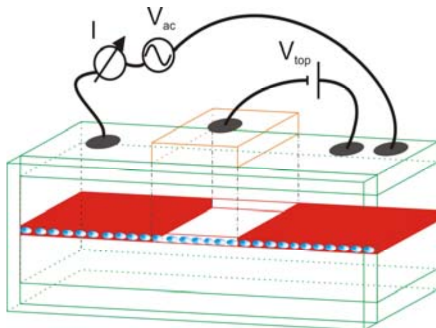

Fig. 2: *Schematics of the configuration to be used for the transport measurements.*

The second approach uses similar sample preparation techniques as far as CEO is concerned but aims at optical properties rather than transport properties. Another major difference is that in this part of the project, the QD are not grown in the self-assembly growth mode but are precisely defined at the intersection of three Quantum Wells.

As it has been reported before, it is possible to fabricate spatially and size controlled pairs of QD by double cleaved edge overgrowth [1]. Due to the planar configuration of the

---

[1]phone: +49-89-289-12783, fax: +49-89-289-12739, email: gjukic@wsi.tum.de

structure, this geometry is ideal to spectroscopic studies of the coupling of identical QDs. It allows also the application of an electric field across the nanostructures. This will be used to tune the coupling strength between the QDs. Up to date, only coupling between similar QD has been studied. The new method proposed here would enable us to study identical as well as intentionally different QDs under the influence of a tunable electric field.

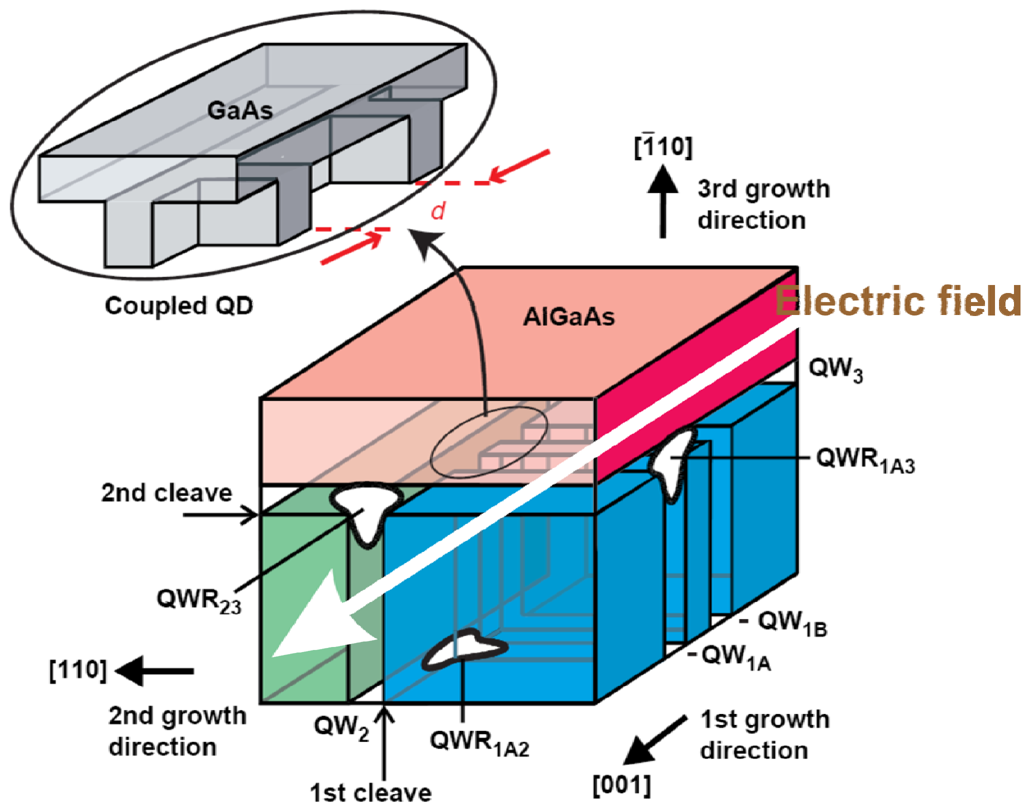

Fig. 2: *Schematical drawing of a QD structure (not to scale), which is formed by three growth steps and two in situ cleavage steps. The white arrow from back to front indicates the direction of the electric field. The inset shows the two crossings of three quantum wells, which constitute the coupled QD.*

[1] G. Schedelbeck, W. Wegscheider, M. Bichler, and G. Abstreiter, *Science* **279**, 1792 (1997)

supported by DFG (SFB 631, TP B1)

High-resolution X-ray diffraction study of stress relaxation in Si-doped AlN grown by plasma-assisted molecular-beam epitaxy

Martin Hermann[1], Florian Furtmayr, Martin Stutzmann, and Martin Eickhoff

The wide band gap semiconductor AlN ($E_{gap} = 6.2\ eV$) exhibits a high breakdown field of more than *3.3 MV/cm*, a high thermal conductivity of *3.2 W/cmK* and an excellent thermal stability with a decomposition temperature of more than *1000 °C* in vacuum. Therefore AlN, is considered as a promising material for high power and high temperature applications. Conductive AlN could be also applied in electronic devices and improve e.g. the performance of UV light emitters using AlN as a field emitter. For such applications controllable n-type conductivity is essential. For AlGaN alloys, Silicon is considered as the donor of choice. Si is a shallow donor in Ga-rich AlGaN alloys. However, with increasing Al-content it tends to form deep states, which makes it difficult to accomplish a significant conductivity in Si-doped AlN. A possible approach is the formation of an impurity band by increasing the Si impurity content above the Mott threshold concentration of about *1 at. %*. Such a high amount of Si has a severe impact on the crystal quality. Moreover, the incorporation of Si in AlN is found to depend strongly on the growth conditions.

Nitrogen-rich conditions during the growth of AlN:Si on c-plane sapphire by molecular-beam epitaxy have been found to allow a homogeneous Si incorporation of up to $[Si]=5.2\times10^{21}\ cm^{-3}$ [1]. Silicon is known to act as an anti-surfactant during the growth of GaN and AlGaN alloys with a low Al content (< *25 %*). However, in case of AlN, Si acts as a surfactant, most efficiently for $[Si]=5\times10^{20}\ cm^{-3}$. This results in a smooth surface morphology with an rms roughness below *1 nm* and a lateral crystal size of up to *2 μm*, as estimated from the rocking curves of the (00.2) reflex. The increase of the crystal size enables the accumulation of stress. From the shift of the lattice parameters and from Raman spectroscopy measurements the layers are found to be under biaxial comressive stress (up to *3 GPa*).

Once a critical stress is accumulated, the AlN:Si layers relax by the generation of dislocations. In AlN, pure edge and pure screw dislocations are the main types of dislocations. The densities of these two types of dislocations can be seperately extracted from high-resolution X-ray diffraction (HRXRD) measurements. Screw dislocations have a Burgers vector along the *c*-direction, $\vec{b} = [00.1]$, which results in a tilt of lattice planes. Therefore rocking curve measurement of a symmetrical reflex are sensitive to screw dislocations and their density ρ_{screw} can be estimated from $\rho_{screw} = \frac{\Delta\Omega^2_{screw}}{4.35 \cdot b^2_{screw}}$. Here $\Delta\Omega_{screw}$ is the width of the rocking curve recorded at the (00.2) reflex and $b_{screw} = c$ is the length of the Burgers vector. Edge dislocation have a Burgers vector $\vec{b} = \frac{1}{3}[11.0]$ which lies in the sample plane. The resulting twist of the crystallites can be extracted from the width of the rocking curve of e.g. the (10.0) reflex. The edge dislocation density is calculated from an analogous equation as for the screw dislocation density. However, for a diffractometer the (10.0) reflex is not accessible. Using a skewed geometry, where the normal vector of the sample plane is tilted by the angle Ψ with respect to the plane defined by the incident and the diffracted X-ray beam, rocking curve widths with different tilt angles can be used to extrapolate a value

[1]phone: +49-89-289-12755, fax: +49-89-289-12737, email: hermann@wsi.tum.de

for the (10.0) reflex (Ψ=90°), as shown in Fig. 1. The rocking curves have to be measured in this quasi-symmetric geometry with equal incident and reflection angles to avoid a faulty modification of the peak width.

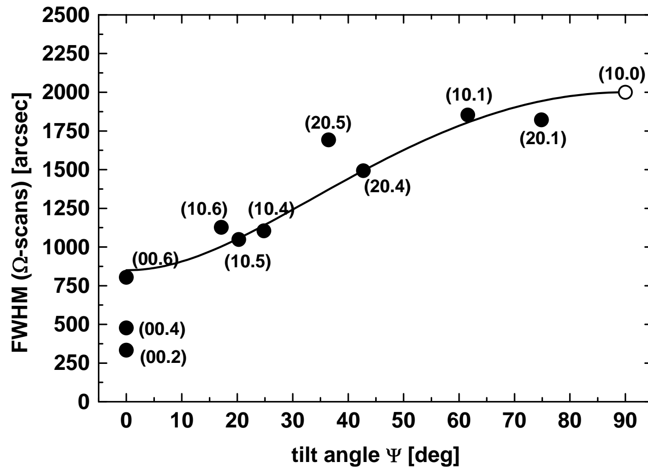

Fig. 1:
Width FWHM(Ω) of several rocking curves for various tilt angles Ψ. A fit of these widths allows the determination of the width of the (10.0) reflex.

The width of the (10.1) reflex is found to be a good approximation for the width of the (10.0) reflex. Therefore, the edge dislocation density can be solely estimated from the width of the (10.1) reflex. Figure 2 shows a summary of the *c* lattice parameter, the stress and the dislocation densities as a function of the Si concentration *[Si]*.

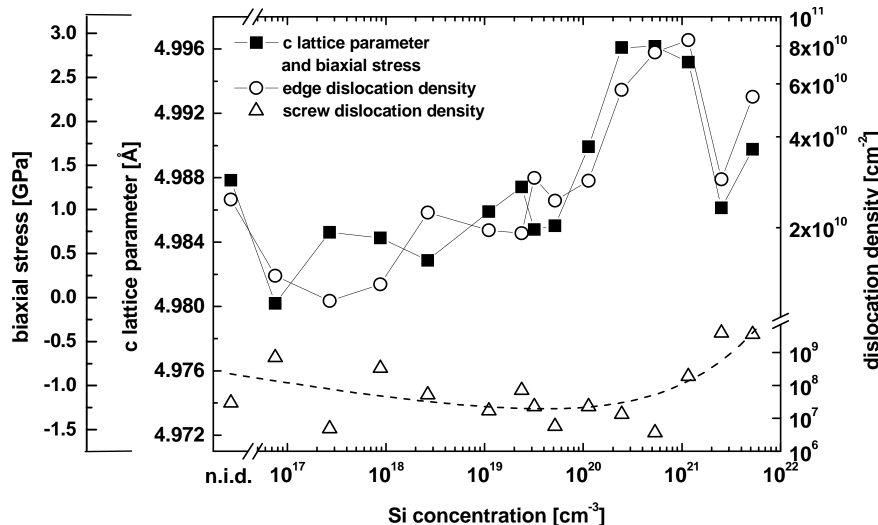

Fig. 2:
c lattice parameter, biaxial stress, screw, and egde dislocation densities vs. Si concentration.

Whereas the screw dislocation density shows no obvious correlation with the biaxial stress, the edge dislocation density and the stress are closely related. The biaxial stress, as calculated from the shift of the *c* lattice parameter, shows a pronounced maximum around $[Si]=5\times10^{20}\ cm^{-3}$. The variation of the edge dislocation density follows this trend, but with a shift towards higher *[Si]*, indicating that the increase of the edge dislocation density is due to a partial relaxation of the AlN:Si layer. Therefore the relaxation of epitaxial AlN:Si layers occurs by forming edge dislocations and not screw dislocations, which are already formed during the nucleation stage.

[1] M. Hermann, F. Furtmayr, A. Bergmaier, G. Dollinger, M.Stutzmann, and M. Eickhoff, Appl. Phys. Lett. **86**, 192108 (2004)
supported by Deutsche Forschungsgemeinschaft (Ei 518/1-1)

Electronic properties of AlN/diamond heterojunctions

Olaf Weidemann[1], Markus Maier, Martin Stutzmann, and Martin Eickhoff

Aluminum nitride as a wide bandgap semiconductor ($E_g = 6.2$ eV) is currently attracting increasing interest for the application in surface acoustic wave devices, high temperature electronics, field emitters or optoelectronic devices in the ultraviolet. While undoped AlN exhibits insulating behavior, the realization of conductive AlN films by silicon doping has been recently demonstrated. However, the fabrication of p-type AlN is still an unsolved problem and prevents the realization of even simple bipolar devices such as pn-diodes. In contrast diamond as a wide bandgap semiconductor ($E_g = 5.4$ eV) can be efficiently p-doped using boron as an acceptor, while reliable and controllable n-type doping still remains problematic. Therefore, the fabrication of n-AlN/p-diamond heterojunctions is an alternative approach for novel wide bandgap bipolar devices.

We have realized such heterojunctions by epitaxial growth of Si-doped AlN films on p-type (IIa) diamond substrates using plasma-assisted molecular beam epitaxy. For the electrical and optical characterization, heterodiodes were processed by mesa etching of the AlN-layer and deposition of ohmic contacts on diamond and AlN. These diodes exhibit a rectification ratio of more than four orders of magnitude (Fig. 1, left). Both series and shunt resistances, extracted from the I-V-characteristics, decrease with increasing temperature. A lower limit of 0.64 eV can be deduced for the effective barrier height at the heterojunction. The devices show a bright blue electroluminescence, characterized by two peaks at 2.1 eV and 2.9 eV, respectively. As shown in the right diagram in Figure 1, the emission intensity decreases in the temperature range between 325 K and 400 K.

For further investigations of the AlN/diamond interface, photoelectron spectroscopy measurements have been carried out using both X-ray and UV excitation sources (XPS/UPS). By sequential growth of the AlN with intermediate XPS and UPS measurements, information about the electronic structure of the hetero-interface can be obtained. It is possible to extract the band bending in the AlN layer, the band offsets of the valence band and conduction band and the influence of interface dipoles.

To carry out these kinds of experiments on small diamond substrates (3 mm x 3 mm),

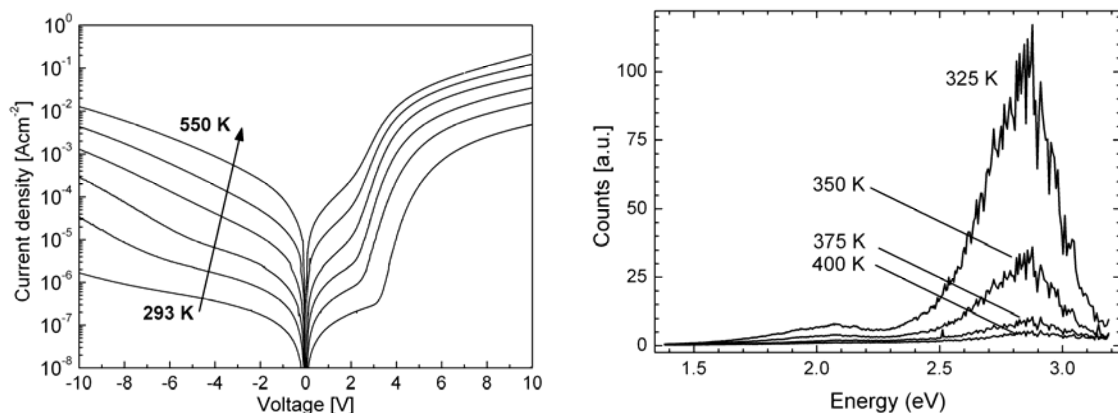

Fig. 1: *Temperature dependent I-V characteristics (left) and temperature dependent electro-luminescence (right) of AlN/diamond heterodiodes.*

[1]phone: +49-89-289-12768, fax: +49-89-289-12737, email: weidemann@wsi.tum.de

the surface analytic system was equipped with a specially adapted aperture for both the X-ray and UV source. In order to establish a well defined bias potential, which is a crucial issue for parts of the experiments, the sample holder was connected to a DC voltage source. An electron-emitting filament was used to compensate charging effects during the measurements.

We have compared H- and O-terminated diamond surfaces with (111) and (100) orientation as substrates for the AlN growth. The XPS measurements in Figure 2 show a difference in electron affinity between these surface terminations of 1.6 eV, which agrees well with reported data measured by other techniques. Nitrogen-plasma treatment, which is the first step in AlN growth, changes the electron affinity drastically for both terminations. A brief AlN growth leads to almost the same value for both surface terminations. The influence of the N-plasma is still not completely understood and will be further investigated.

As the AlN thickness increases, XPS measurements indicate decreasing band maxima in the AlN film which can be attributed to the presence of polarization charges in the pyroelectric AlN. The observed slope is consistent with N-face polarity of the AlN overlayer.

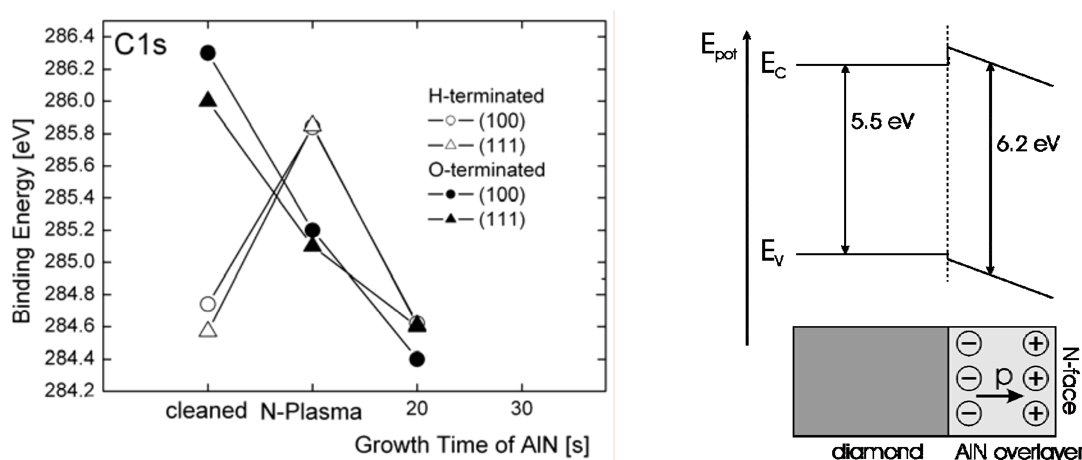

Fig. 2: *(Left) C1s XPS peak position for the clean and N-plasma treated diamond and after the growth of first AlN layer. (Right) Band bending in the AlN overlayer deduced from XPS measurements. The downward bending indicates N-face polarity of the AlN overlayer.*

Financial support by Deutsche Forschungsgemeinschaft (Ei 518/1-1)

Ferromagnetic GeMn nanostructures

Stefan Ahlers, Dominique Bougeard[1], Hubert Riedl, and Gerhard Abstreiter

Combining charge and spin degrees of freedom in single "spintronic" devices has opened new horizons for semiconductor based information processing technology. There are two possibilities to introduce the spin degree of freedom into a semiconductor device, firstly by polarisation of spins in a ferromagnetic metal and subsequent injection into the semiconductor. This method usually involves significant loss of spin polarisation across the metal-semiconductor interface. Secondly, magnetic semiconductors, especially diluted magnetic semiconductors (DMS), can be used. Although considerable progress towards spintronics devices has been made in this material system, e.g. with the realisation of group III-V- or II-VI-based all-semiconductor spin injectors, the essential importance of Si in traditional semiconductor technology make a realisation of a Si compatible, group IV-based DMS highly desirable. First publications on GeMn show promising results. We report on structural, magnetic and transport properties of GeMn layers fabricated by low temperature, solid source molecular beam epitaxy (LT-MBE).

Low substrate temperatures were chosen to overcome the low Mn solubility limit of approximately 10^{-5}% in thermodynamic equilibrium in the Ge matrix. The samples were fabricated at substrate temperatures of T_S=120 °C with a Mn concentration of x=3.4 %, and at T_S=70 °C with x=40.2 %, respectively. Mn concentrations were determined by elastic recoil detection analysis for layers with typical thicknesses of 200 nm. RHEED monitoring of the surface quality during MBE growth indicates the formation of a rough surface and an onset of two-dimensional island growth during co-deposition of Ge and Mn for

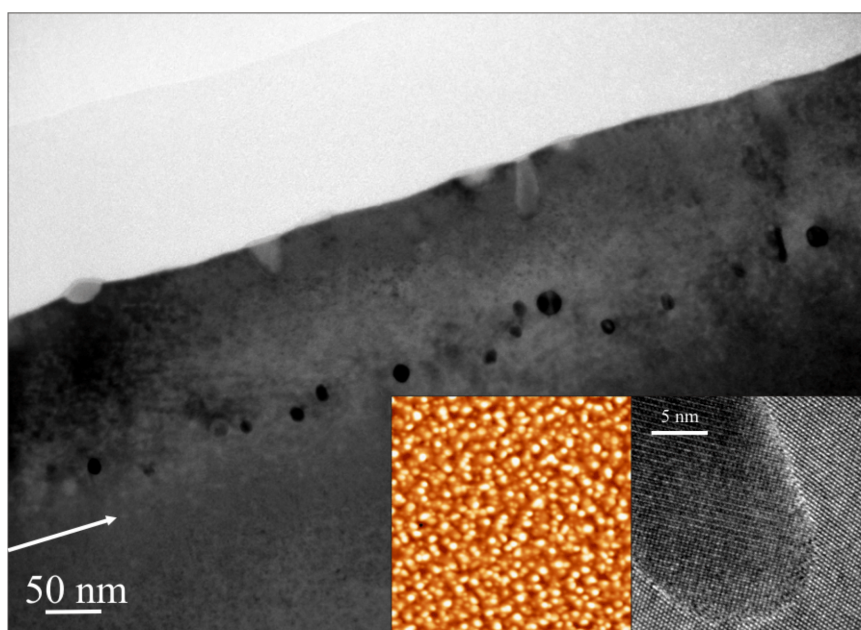

Fig. 1: *Cross-sectional TEM image of a sample with 3.4 % Mn and T_S=120 °C. Clusters accumulate at the interface between the Ge substrate and the GeMn layer (white arrow) and also near the surface. Left inset: AFM image of the sample surface. Image size 2x2 μm^2, dark to bright height scale 20 nm. Right inset: high resolution TEM image of a typical incoherent cluster.*

[1]phone: +49-89-289-12777, fax: +49-89-289-12739, email: bougeard@wsi.tum.de

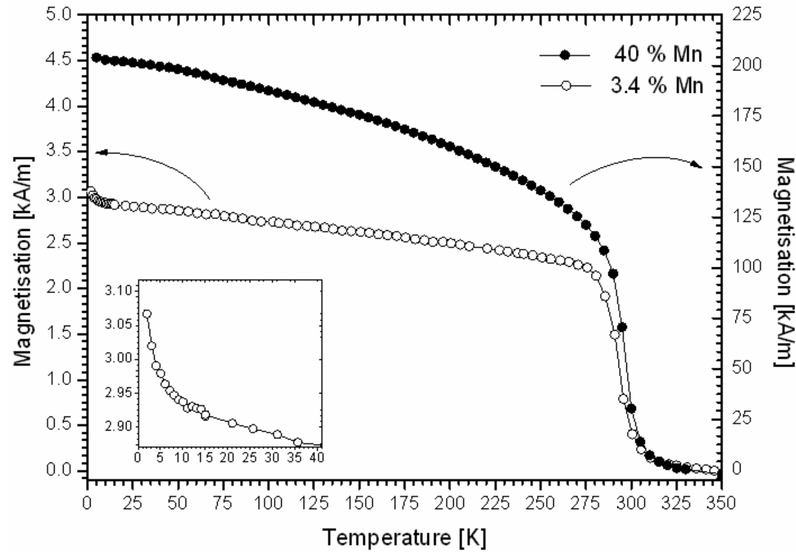

Fig. 2: *Magnetisation over temperature of GeMn with 3.4 % Mn and T_S=120 °C (open circles) and 40.2 % Mn, T_S=70 °C (full circles),H=1000 Oe=80 kA/m. The magnetisation curve is clearly reminiscent of Mn_5Ge_3. Inset: low temperature region of the 3.4 % sample.*

x=3.4 %. An AFM picture of this sample surface in the left inset of Fig. 1 shows island formation with diameters of ~100 nm and a root mean square roughness of 3.3 nm. While a Mn concentration of x=40.2 % leads to polycrystalline films the TEM analysis indicates good crystalline quality of the GeMn film without lattice defects or dislocation accumulation for x=3.4%. However, the TEM measurements also reveal the presence of clusters in the layer (Fig. 1). These clusters reveal a hexagonal structure and are incoherently included in the surrounding cubic matrix (right inset in Fig. 1). Cluster diameters range from 15 to 20 nm near the interface with the substrate, while slightly larger clusters with a diameter of ~30 nm in average occur at the surface of the sample. Moiré patterns are found for the bulk clusters. This suggests different cluster orientations.

The magnetic properties have been examined by SQUID magnetometry. Since low Mn solubility involves the risk of GeMn phase formation, particular attention was paid to signatures of these phases. The most stable intermetallic GeMn compound is Mn_5Ge_3 with a Curie temperature of T_C=296 °C and a magnetic moment of 2.6 μ_B per Mn atom at a temperature of 4.2 K. Thermomagnetic measurements (Fig. 2) show a curve shape reminiscent of the results for Mn_5Ge_3. Fitting the data according to the Curie-Weiss law leads to a transition temperature of 300 K independent on Mn concentration. The saturation magnetisation is 1.07 μ_B per Mn atom for x=3.4 % at 4.2 K if an equal contribution of all Mn atoms to the magnetisation is assumed, which is lower than the literature value of 2.6 μ_B per Mn atom for Mn_5Ge_3. On the other hand, polycrystalline samples with x=40.2 %, where an enhanced formation of the intermetallic phase formation is observed, have a calculated magnetic moment of 2.99 μ_B per Mn atom which matches the Mn_5Ge_3 value. It is therefore assumed that for x=3.4 %, a certain amount of Mn is dispersed into the Ge matrix.

High field room temperature Hall measurements indicate p-type conduction in the samples, with hole concentrations of $5 \cdot 10^{17}$ cm^{-3} for x=3.4 % and $7.2 \cdot 10^{19}$ cm^{-3} for x=40.2 %, respectively. As the determined Mn concentrations lie orders of magnitude above these values, only a small fraction of the incorporated Mn atoms is electrically active.

---

supported by DFG (SFB 631, Teilprojekt C4)
TEM in cooperation with A. Trampert, Paul-Drude-Institut für Festkörperelektronik, Berlin

Structural and magnetic properties of Mn_5Ge_3 clusters in a dilute magnetic germanium matrix

Christoph Bihler[1], Christian Jaeger, Thomas Vallaitis, Mario Gjukic, and Martin S. Brandt

One major problem in realizing spintronic devices is the injection of spin-polarized charge carriers into nonmagnetic semiconductors. Dilute magnetic semiconductors (DMS) are one promising approach to this problem. So far, most research has focused on III/V DMS such as $Ga_{1-x}Mn_xAs$, with Curie temperatures as large as $T_C = 172$ K. Mn-doped Ge, which as a group-IV element would be compatible with silicon-based microelectronics, has been studied to a much lesser extent. The first successful growth of DMS Mn_xGe_{1-x} layers has been reported in 2002 by Park *et al.* [Science **295**, 651 (2002)]. Since then, only a few further studies on Mn_xGe_{1-x} have been published. This is probably caused by the fact that the growth of the DMS Mn_xGe_{1-x} is complicated by its tendency to form thermodynamically favorable ferromagnetic intermetallic precipitates, e.g. Mn_5Ge_3. To gain further insight into the complex growth of this material system, we have performed a detailed structural and magnetic characterization of molecular-beam epitaxy grown Ge:Mn layers. The transmission electron microscopy (TEM) overview images in Fig. 1(a) and (b) show the existence of spherical to elongated clusters with a diameter of 10-15 nm. The precipitation does not start immediately at the wafer epilayer interface. Also, the distribution of clusters throughout the epilayer is inhomogeneous. Within almost all of these clusters, we observe well defined Moiré patterns which are a strong indication for precipitates which are monocrystalline and are embedded in a monocrystalline matrix. Furthermore, the clusters appear to be preferentially oriented, as the Moiré patterns of most clusters are parallel to the interface.

Figure 1(c) and (d) show TEM images of the $Mn_{0.03}Ge_{0.97}$ epilayer with atomic resolution. The images are cross sections of the Ge(110) plane. The orientation of the wafer/epilayer interface is marked by dashed lines. The well resolved lattice planes extending throughout the whole image reflect the high crystalline quality of the epilayer. The calculated fast Fourier transformation (FFT) pattern of Fig. 1(c), shown in Fig. 1(f), can be understood with the help of the theoretical diffraction patterns shown in Fig. 1(e). The main features of the FFT pattern are very well reproduced by the diffraction pattern of Ge(110) (Fig. 1(e), left panel). If one assumes an orientation of the hexagonal Mn_5Ge_3 phase ($a_{Mn_5Ge_3} = 7.184$ Å, $c_{Mn_5Ge_3} = 5.053$ Å) with $[0001]_{Mn_5Ge_3} \parallel [001]_{Ge}$ and $[\text{-}2110]_{Mn_5Ge_3} \parallel [110]_{Ge}$ for the cluster in Fig. 1(c), the corresponding diffraction pattern (Fig. 1(e), right panel) together with that of Ge(110) very well reproduces the FFT pattern. The lattice mismatch of 3.4% between $[03\text{-}30]_{Mn_5Ge_3}$ and $[2\text{-}20]_{Ge}$ parallel to the surface is apparently compensated a by homogeneous distortion (only one reflex is visible for both $[2\text{-}20]_{Ge}$ and $[03\text{-}30]_{Mn_5Ge_3}$). This is not possible any more for the much larger lattice mismatch of 11.1% between $[0001]_{Mn_5Ge_3}$ and $[001]_{Ge}$ in growth direction, where two separate diffraction reflexes for $[002]_{Ge}$ and $[0002]_{Mn_5Ge_3}$ are identifiable. Therefore, the corresponding interface has to be semi-coherent and has to exhibit misfit dislocations, which as a matter of fact are visible via tracking the progression of the atomic layers as indicated by the lattice planes in Fig. 1(c). Further evidence for a mismatch of 11.1% is provided by the cluster shown in Fig. 1(d). In this image, the geometric cluster to matrix relation gives rise to a pronounced

---

in cooperation with Eckhard Pippel, Jörg Woltersdorf, and Ulrich Gösele, MPI Halle
[1]phone: +49-89-289-12755, fax: +49-89-12737, email: bihler@wsi.tum.de

Moiré pattern parallel to Ge[001]. With a_{Ge} = 5.658 Å, a period of 2.4 nm for the Moiré pattern is expected, which is in good agreement with d = 2.1 nm observed experimentally in Fig. 1(d), particularly, as a possible superposition of homogeneous and periodic lattice strain caused by the interaction of the growth partners should be taken into consideration. We would like to point out that for the epitaxy relation determined above, there also is a mismatch of 11.4% between $[-2110]_{Mn_5Ge_3}$ and $[110]_{Ge}$ perpendicular to the HR-TEM cross section in Fig. 1(c), probably leading to further dislocations. The fact that the clusters are only observed after the growth of about 50 nm of Ge:Mn with 2% Mn suggests that the formation of Mn_5Ge_3 clusters at the growth temperature of 225°C can only occur when a large enough amount of Mn is accumulated at the growth front. When this is the case, homogeneous nucleation sets in at a well defined distance from the interface.

Temperature dependent magnetization measurements show the presence of a magnetic phase with a transition temperature of $T_C \sim 290$ K. This corresponds to the value $T_C = 296$ K reported for the intermetallic compound Mn_5Ge_3. Furthermore, the magnetic phase exhibits a magnetic anisotropy with the easy magnetic axis in out-of-plane direction and the hard axis in plane. According to our TEM analysis, the easy out-of-plane direction corresponds to the hexagonal [0001] direction of the majority of the Mn_5Ge_3 clusters in agreement with earlier work by Tawara *et al.* [J. Phys. Soc. Jpn. **18**, 773 (1963)].

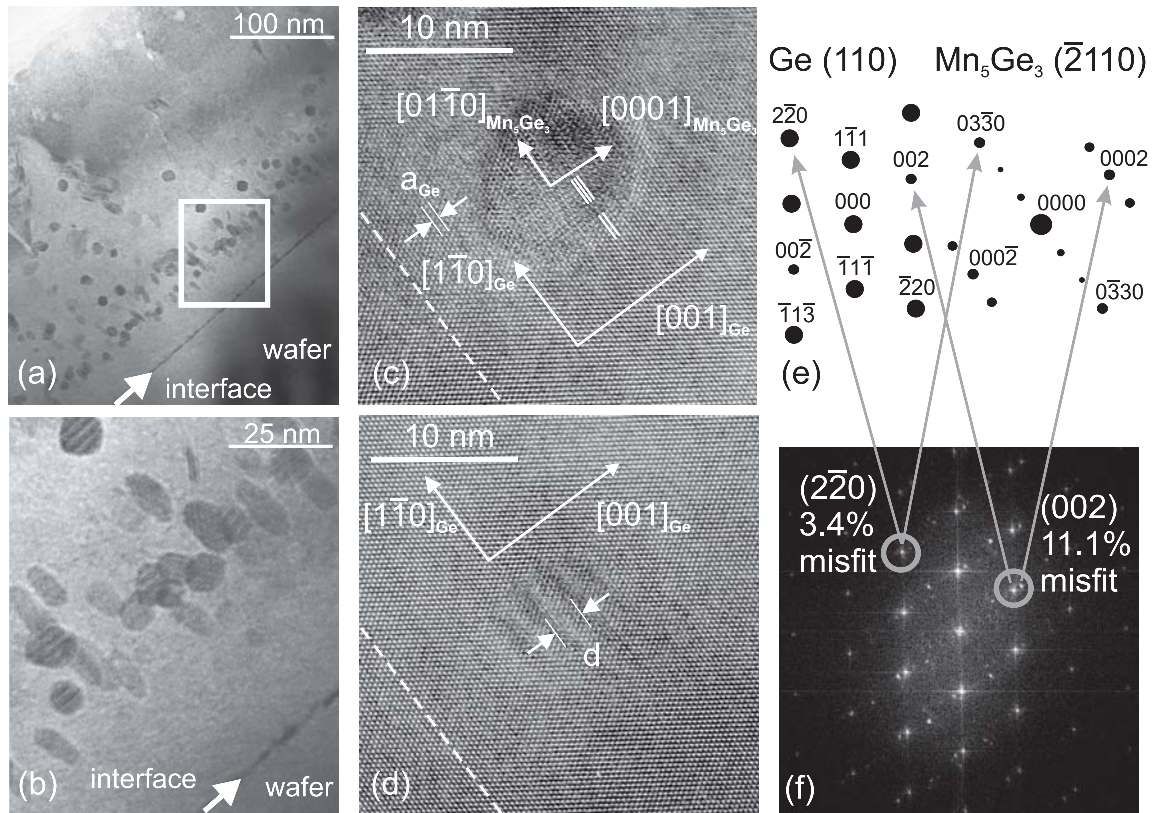

Fig. 1: *(a) TEM image of a $Mn_{0.03}Ge_{0.97}$ epilayer on a Ge wafer. (b) Magnified section. The arrows mark the interface between wafer and epilayer (c) and (d) High resolution TEM images of typical clusters in $Mn_{0.03}Ge_{0.97}$. The orientation of the wafer-layer interface is marked by dashed lines. (e) Standard diffraction patterns of Ge(110) and $Mn_{0.03}Ge_{0.97}$ (-2110). (f) Calculated FFT pattern of (c).*

supported by Deutsche Forschungsgemeinschaft (SFB 631, Project C3)

Aluminum-induced crystallization of amorphous silicon-germanium thin films for photovoltaic applications

M. Scholz[1], M. Gjukic, S. Gatz, T. Antesberger, and M. Stutzmann

In the rapidly growing photovoltaic market mono-crystalline silicon still plays a dominant role. However in order to avoid a silicon bottleneck, new technologies have to be developed to produce highly efficient and inexpensive thin film photovoltaic modules.
A great potential for cost reduction is expected from thin film silicon or silicon-germanium cells on low cost substrates. Here, a promising low-temperature approach is the recrystallisation of amorphous silicon or silicon-germanium layers. The most efficient silicon solar cell made so far at low temperatures on a foreign substrate material have an efficiency of 9.2% and were made by solid phase crystallisation of PECVD (**P**lasma **E**nhanced **C**hemical **V**apour **D**eposition) a-Si on a metal substrate by Matsujama in 1986. This is still far away from the performance of modern bulk Si solar cells with efficiencies of about 17%. Other low-temperature deposition methods have to be found to obtain high-quality material.

To this end, we are investigating on the crystallisation of amorphous Si or SiGe layers by Aluminium Induced Layer Exchange (ALILE). A bilayer structure of amorphous silicon–germanium ($a\text{-}Si_{1-x}Ge_x$) and aluminium (Al) is deposited on a quartz or glass substrate. An annealing process well below the eutectic temperature of the binary Al–Ge sys-

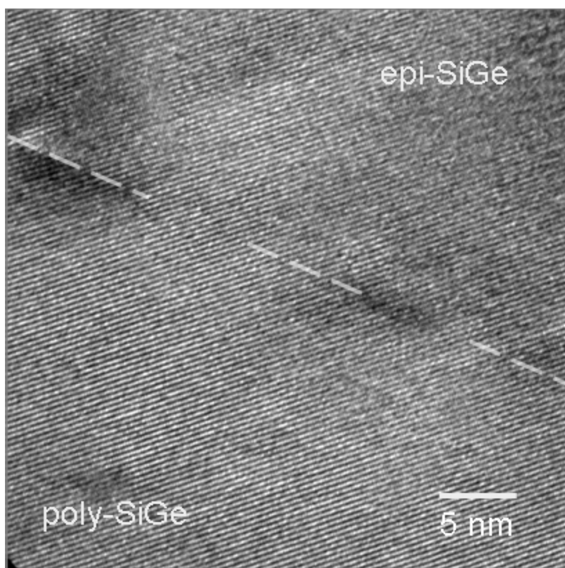

Fig. 1: *TEM micrograph of a homo-epitaxial thickened <112> oriented SiGe grain. The sample was thickened at 200°C by a PECVD - process. The dashed line indicates the position of the former poly-SiGe surface. Before growth the surface was passivated by a HF-dip and H-plasma.*

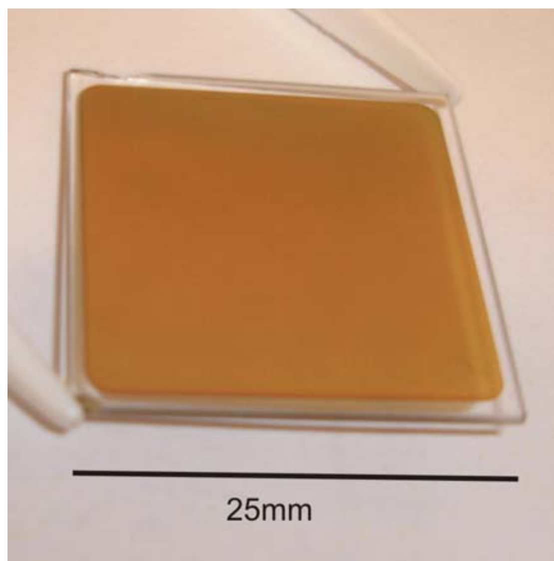

Fig. 2: *The ALILE process is capable also to very thin layers down to about 10 nm film thickness. The optical photograph shows a 40 nm poly-Si layer on quartz after the removal of the Aluminum. This example gives an impression of the homogeneity and the scalability of the process.*

[1]phone: +49-89-289-12769, fax: +49-89-289-12737, email: scholz@wsi.tum.de

tem (T_E=420 °C) results in a complete exchange of the position of the two layers and, at the same time, leads to the formation of a coherent polycrystalline $Si_{1-x}Ge_x$ thin film on top of an Aluminium back contact layer.

As the most promising material for solar cell application we investigated silicon-germanium alloys with a germanium content of about 80%. In the relevant range of the solar spectrum the absorption coefficient is at least one order of magnitude higher then in pure silicon because of the lower direct band gap. The indirect bandgap decreases from 1.15 eV (Si) to about 0.95 eV ($Si_{20}Ge_{80}$). As a result the maximum theoretical photovoltaic conversion efficiency decreases only slightly too about 27%.

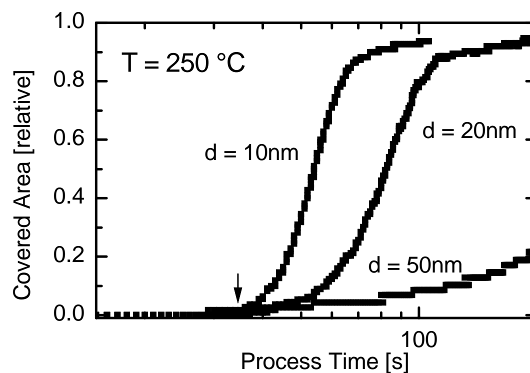

Fig. 3: *Three layers with different thickness (d = 10nm, 20nm, 50nm) were annealed at 250°C. In contrast to the nucleation time (small arrow) the total process time depends strongly on film thickness.*

Our recrystallized ALILE-Silicon-Germanium layers consist of very large crystallites of 10-100 μm size which are one to two orders of magnitude larger then the crystallites achieved by solid phase or laser induced crystallisation. This is quite remarkable in view of the low process temperature (< 550°). The layers feature a high carrier concentration (up to 5 x 10^{-20} cm^{-3}) and surprisingly high carrier mobility (up to 100 cm^2/Vs). The optical and electrical properties are more similar to crystalline than to amorphous or nano-crystalline material. These properties make ALILE-SiGe layers very attractive for the use as back surface field and seed layers for solar cells.

Our co-operation partners at the Forschungszentrum Jülich have already produced a first generation of silicon solar cells with efficiencies up to 4 % on Si-ALILE substrates. After a pre-treatment with HF to remove the natural oxide, the ALILE seed layers were epitaxially thickened in a PECVD process at 200°C with a 1µm thick p/i/n structure. The whole process took place at a temperature below 400°C. In Fig 1 a TEM micrograph of an epitaxial SiGe layer on an ALILE substrate is shown. The original <112> orientation of the substrate is well conserved.

In a further study we have investigated the possibility to produce ultra thin polycrystalline Si films on glass by the ALILE process. Layer thicknesses down to about 10nm were achieved. The total process time of the layer exchange decreases with decreasing layer thickness. In Fig. 2 a sample with a layer thickness of about 40nm is shown, demonstrating the scalability of the process and the homogeneity of the samples obtained.

---

supported by BMWA (contract No. 0329814A) 2002-2005
supported by BMU (contract No. 0329986) 2005-2007

Aluminum-induced crystallization of Si nanoparticle thin films dispersed from solution

Robert Lechner[1], Mario Gjukic, Nuryanti, André Ebbers[2], Frank-Martin Petrat[2], Martin S. Brandt, and Martin Stutzmann

The fact that amorphous semiconductors can be crystallized at moderate temperatures when annealed in contact with metals (metal induced crystallization, MIC) has been known for a long time. In recent years, especially a form of layer exchange process has gained a lot of interest which enables the realization of thin crystalline silicon films on glass substrates [1]. In our group, the possibility to apply this so-called aluminum induced layer exchange (ALILE) method to the binary silicon-germanium alloy system ($Si_{1-x}Ge_x$), a material with high potential for thin-film photovoltaics, has already been demonstrated [2].

In our current research, we focus on the properties of printed silicon nanoparticles as a cheap alternative to conventional thin-film deposition methods for various applications. This work is done in cooperation with Degussa AG, which developed reactors for the large-scale production of nanosize particles. There, also methods of dispersing the silicon nanoparticles in organic solvents and subsequent coating of glass substrates have been developed and optimized.

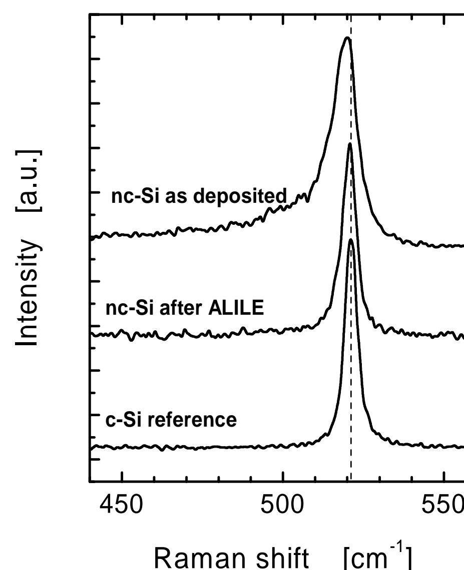

Fig. 1: *Room temperature Raman spectra of as deposited and ALILE crystallized nanocrystalline silicon samples in comparison to a crystalline silicon reference sample.*

The typical size distribution of the silicon nanoparticles ranges from 5-20 nm. As Fig. 1 shows, the Raman spectrum of the initial material already reveals its nanocrystalline nature. The shift of 1.1 cm^{-1} and the increased width of the phonon peak compared to the crystalline silicon reference wafer are a consequence of the small particle size [3]. The absence of major amorphous contributions to the spectra in the spectral range around 480 cm^{-1} is in good accordance with the TEM images that show no amorphous shell around the crystalline core of the particles.

The center curve in Fig. 1 shows the result of an ALILE recrystallization experiment with silicon nanoparticles. To this end, quartz substrates have been coated with a 250 nm film of aluminum and a 1 µm layer of silicon nanoparticles cast from solution. Subsequently, the samples have been annealed in nitrogen atmosphere at a temperature of 550°C for 20h. After the annealing, a film of crystalline silicon has formed on the substrate, still containing remnants of aluminum and nanocrystalline silicon. The degree of crystallinity in the obtained polycrystalline layer can be assessed from the Raman spectra in Fig. 1, which shows the prominent silicon TO phonon peak at 520 cm^{-1} without significant shift or broadening, and without amorphous contributions.

---

[1]phone: +49-89-289-12783, fax: +49-89-289-12737, email: lechner@wsi.tum.de
[2]Degussa AG, Marl

Similar conclusions can be drawn from optical spectroscopy in the UV, visible, and near infrared range. Fig. 2 shows the reflectivity spectra of samples before and after the ALILE process in comparison with a crystalline silicon reference sample. Before the annealing, the nanocrystalline silicon film shows only weak signatures around the positions of the van Hove peaks E_1 and E_2 at 3.4 and 4.5 eV, respectively. After the ALILE recrystallization, the reflectivity spectrum aligns well with that of the crystalline reference. Here, the thin-film interference fringes in the low energy spectral range confirm the successful layer exchange: After the process, the polycrystalline silicon film thickness resembles the thickness of the initial aluminum film (200 nm), whereas the initial nanocrystalline silicon layer had a thickness of 1.2 µm.

Thus, crystalline silicon nanoparticles may also be used as starting material for the ALILE process. Generally, the difference in the Gibbs free energy between the amorphous and the crystalline phase is considered to be the driving force behind metal induced crystallization phenomena. In this case, the initial material is already crystalline, so the transformation of the loosely packed nanoparticles into a polycrystalline silicon film is quite surprising. It can only be enabled by the small size of the particles with a high surface energy. The small difference in Gibbs free energy between the nanoparticles and the growing polycrystalline silicon grains compared to the case of an amorphous silicon precursor can explain the significantly retarded crystallization kinetics.

Still, this method comprises the possibility to realize polycrystalline silicon films on glass substrates at temperatures below 600°C and without the need to deposit the silicon in a vacuum deposition system.

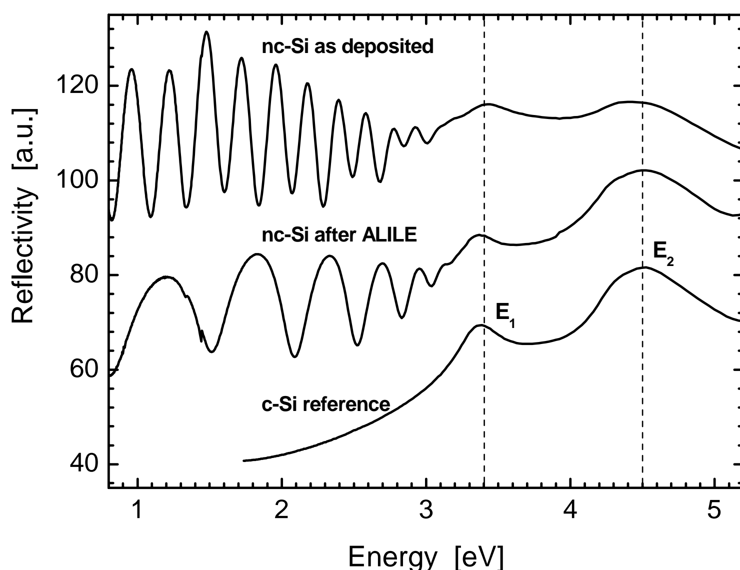

***Fig. 2:** Optical reflectivity spectra of as deposited and ALILE recrystallized nanocrystalline silicon samples in comparison with a crystalline silicon wafer reference.*

[1] O. Nast, T. Puzzer, L.M. Koschier, A.B. Sproul, and S.R. Wenham, Applied Physics Letters **73**, 3214 (1998).

[2] M. Gjukic, M. Buschbeck, R. Lechner, and M. Stutzmann, Applied Physics Letters, **85**, 2134 (2004).

[3] I. H. Campbell and P. M. Fauchet, Solid State Communications, **58**, 739 (1986).

This work is done in cooperation with Degussa AG, Marl,
supported by EU

Molecular beam epitaxy of metal oxides

Thomas Wassner[1], Bernhard Laumer, Martin Stutzmann, and Martin Eickhoff

During the last years metal oxides have gained increasing interest for a wide range of applications. Examples are front surface electrodes of solar cells or transparent conductive oxides in flat-panel displays. In addition, metal oxides films (e.g. tin oxide) are one of the most important material systems in todays solid state gas sensor technology. Zinc oxide (ZnO) as a prominent example for semiconducting metal oxides, has attracted considerable attention in the recent years because of its wide bandgap of 3.4 eV at room temperature and its large exciton binding energy of 60 meV. These properties are ideal for optoelectronic applications in the UV-region and thus can possibly compete with GaN with a similar bandgap, but a much smaller exciton binding energy of about 24 meV.

Since a high crystal and surface quality as well as well controlled electronic properties are desirable for most of the applications mentioned above, different techniques for epitaxial growth of high quality thin film oxides are used. The most promising are pulsed-laser deposition (PLD), metal-organic chemical vapour deposition (MOCVD), and plasma-assisted molecular beam epitaxy (PAMBE). The advantages of the latter are the realization of sharp heterointerfaces and doping profiles, good control of alloy composition as well as in-situ analytics during the growth process.

The metal oxide PAMBE system (Riber MBE 32), schematically shown in Figure 1, consists of several metal effusion cells as the sources for ultra pure metal atoms. Oxygen radicals are supplied by an rf-plasma cell (Oxford). Heteroepitaxial growth is performed on 2” c-plane sapphire substrates.

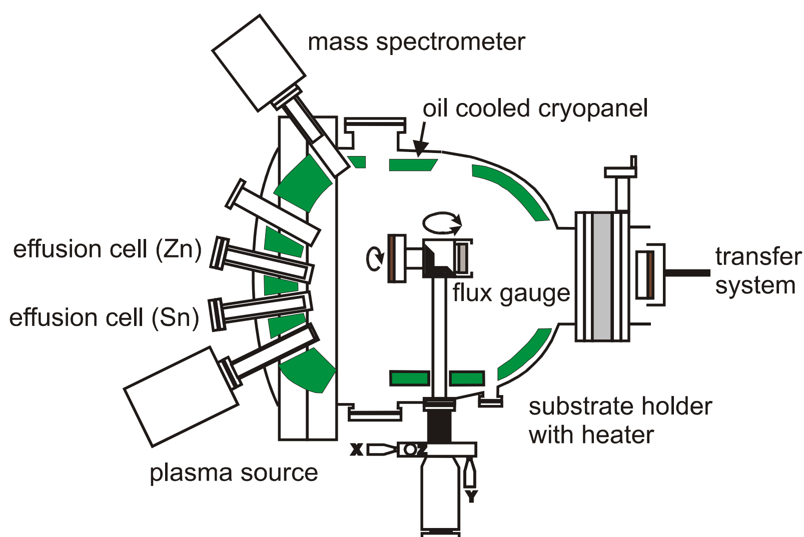

Fig. 1: *Schematic layout of the metal oxide PAMBE System*

[1]phone: +49-89-289-12769, fax: +49-89-289-12737, email: wassner@wsi.tum.de

The most important growth parameters which need to be optimized in order to achieve a high crystal quality are the substrate temperature and the Zn/O ratio during the growth process. The influence of these growth parameters on the resulting layer quality can be monitored by the structural quality as well the surface morphology of the resulting films. The structural quality was analyzed by high resolution X-ray diffraction (HRXRD). In Figure 2 the full width at half maximum (FWHM) of the Ω-scan of the (00.2)-reflex is shown as a function of the substrate temperature during growth. At a substrate temperature of 650°C a minimum is observed. The band edge photoluminescence of a ZnO epilayer grown under optimized conditions is shown in the inset of Figure 2. At approximately the same temperature, the root mean square surface roughness (rms) is also minimized (Fig. 3). The existence of such a minimum reflects the two competing processes, enhancement of the surface mobility of adsorbed species and an increase of the desorption of Zn-atoms. The resulting concentration of free carriers is 2×10^{18} cm^{-3}, which will be further reduced by optimization of the growth parameters.

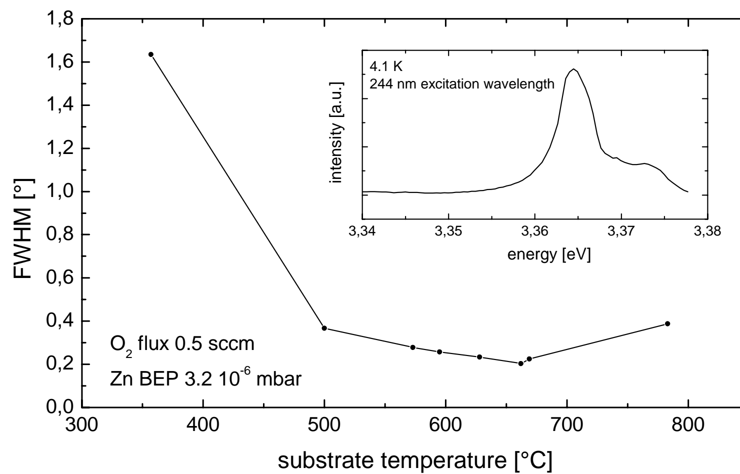

Fig. 2: *The FWHM of the 00.2 Ω-Scan versus substrate temperature. The insert shows a PL spectrum taken at 4.1K.*

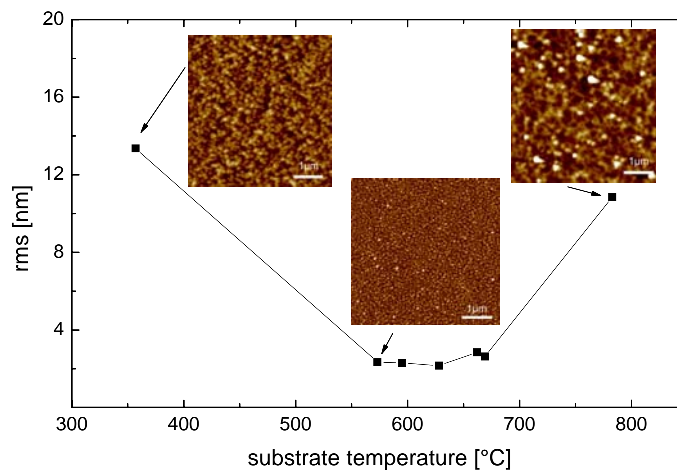

Fig. 3: *The rms roughness of ZnO epilayers versus substrate temperature. The AFM pictures display the dependence of surface morphology on substrate temperature.*

Low resistive *p*-GaSb / *n*-InAsSb tunnel-junctions homogeneously doped with silicon for intra-device contacts

Oliver Dier[1], Christian Lauer, and M.-C. Amann

Recently, the broken gap band alignment of InAs-GaSb lattice-matched to InAs or GaSb substrates has drawn very much attention for various interesting devices such as resonant interband tunneling diodes (RTID), low power logics, or photodiodes. We intend to transfer the successful buried tunnel-junction (BTJ) concept for intra-device contacts in vertical cavity surface emitting lasers (VCSELs) from InP to GaSb substrates. A low-resistive tunnel-junction is crucial for the device to minimize heating due to ohmic losses and leakage currents, which would deteriorate current confinement. Especially in low-bandgap materials as GaSb the voltage-drop over the tunnel-junction has to be extremely low, otherwise the leakage-currents over the reverse biased *p*/*n*-junction around the tunnel-junction hinder current confinement. Therefore we explore a GaSb/$InAs_{0.91}Sb$ tunneling structure based on GaSb-substrates homogeneously doped with Silicon.

To remove all parasitic resistivities, our samples just contained the tunnel-junction and the metal-semiconductor interfaces, as shown in Fig. 1. All MBE-grown layers were doped with Si, which due to its amphoteric nature at the same time acts as donor in InAsSb and as acceptor in GaSb. Therefore no diffusion of dopants at the junction can occur, as it was observed for beryllium. On *p*-type (1×10^{18} cm^{-3}) Zn-doped GaSb-substrates we deposited a 2 µm thick GaSb:Si buffer (doped 1×10^{18} cm^{-3}) to prevent diffusion of Zn into the structure. The tunnel-junction itself was formed by a highly doped, 20 nm GaSb:Si / 20 nm InAsSb:Si heterojunction. The doping levels for different samples were 1×10^{19} cm^{-3} and 1×10^{20} cm^{-3}, respectively. At these doping levels almost no band-bending occurs at the GaSb / InAsSb interface. For the *n*-side contact two different doping levels of 1×10^{19} cm^{-3} and 1×10^{20} cm^{-3} were applied to determine the influence of doping on the contact resistance. The samples were processed to circular mesas with diameters varying from 4 µm to 23 µm and passivated with SiO_2. The low-resistive metal-semiconductor contacts on *n*-InAsSb as well as on the *p*-GaSb substrate consisted of sputtered and annealed Ti/Pt/Au layers, the processing details are described in the last yearbook.

Independent of the doping level at the tunnel-junction as well as the doping level at the metal-semiconductor contact, all samples showed ohmic I-V-curves, as measured with four-point probe measurements. The resistivity measurements for different mesa diameters are given in Fig. 2. The measurements for different mesas of the same size yielded almost the same values, so no error bars are given. The contact resistivity was calculated using a point-contact geometry method. For the substrate resistance 7.7×10^{-3} Ωcm were assumed according to the substrate material data sheet. The lowest values of 2.4×10^{-6} Ωcm^2 were achieved for the highly doped (1×10^{20} cm^{-3} in both junctions) sample. The homogeneously low doped sample (1×10^{19} cm^{-3}) showed a similar resistivity of only 2.5×10^{-6} Ωcm^2, while the sample with low-doped tunnel-junction and highly-doped contact layers exhibited a larger resistivity of 3.5×10^{-6} Ωcm^2. This phenomenon isn't understood yet, we assume that the change of doping concentration in InAsSb led to a compositional change of the As/Sb fraction in the material and therefore to barrier spikes in the conduction band. From these results can be deduced that the resistivity of $3.3\times10^{-6}\Omega cm^2$ for the metal-semiconductor junction as it was found in our previous work is mainly dominated by the *n*-GaSb / n^+-

[1]phone: +49-89-289-12788, fax: +49-89-3206620, email: dier@wsi.tum.de

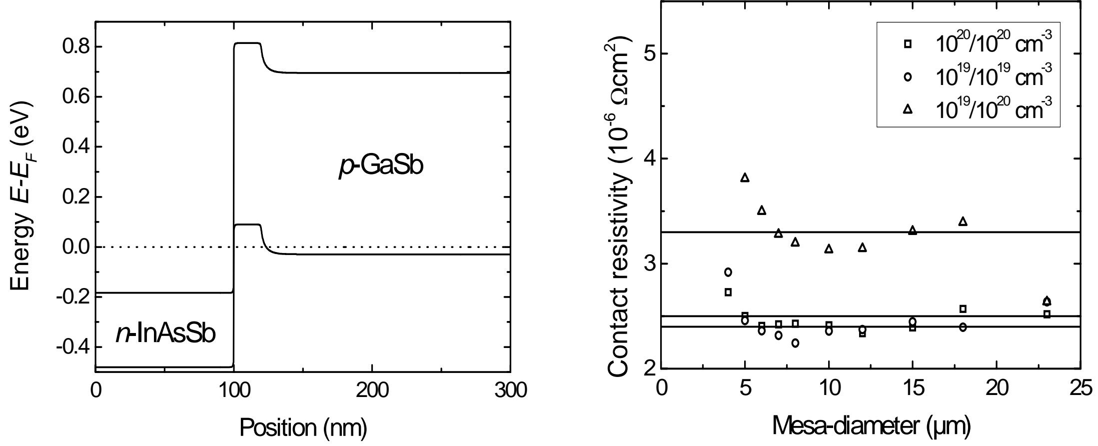

Fig. 1: *(a) Band structure diagram for a n-InAsSb / p-GaSb tunnel junction homogenously doped with Si (1×10^{20} cm^{-3}) on both sides of the junction. Due to the high doping almost no band-bending occurs at the interface. (b) From the measurement extracted resistivities as derived by a point-contact method. Almost the same low values were achieved for a dopant concentration of 1×10^{20} cm^{-3} and 1×10^{19} cm^{-3} on both the tunnel-junction and the metal-semiconductor interface. The sample doped with 1×10^{19} cm^{-3} at the tunnel-junction and 1×10^{20} cm^{-3} at the contact showed a three times larger resistivity.*

InAsSb heterojunction, because without this junction, as shown here, even lower values are reached. The same conclusion can be drawn for previously reached tunnel-junction results, where two *n*-GaSb / *n*-InAsSb heterojunctions led to a resistivity of $2.6\times10^{-5}\Omega cm^2$. For application as intra-device contacts the resistivity of the tunnel-junction is low enough, but the effects of GaSb / InAsSb heterobarriers have to be reduced furthermore by higher doping concentrations or compositional gradings. The use of Si as dopant on both sides of the junction should provide a long-term stability of a device, especially in high current-density areas as in the current-confined regions of VCSEL devices, where 20 $kAcm^{-2}$ and more can be reached and therefore diffusion of dopants or electromigration is an issue. Summarizing it can be stated that using high Si-doping for both *n*-InAsSb and *p*-GaSb, we achieved extremely low-resistive tunnel-junctions with a resistivity of 2.4×10^{-6} Ωcm^2. This value is well suited for intra-device contacts to be implemented in GaSb-based VCSELs.

n-doped epitaxial AlAsSb/GaSb distributed Bragg reflectors on GaSb substrate

Christian Lauer[1], Oliver Dier, and Markus-Christian Amann

GaSb-based semiconductor diode lasers with emission wavelengths above 2µm are interesting light sources for tunable diode lasers absorption spectroscopy (TDLAS) applications. TDLAS requires the tuning of the emission over a small wavelength range of about 5nm. It is difficult or expensive to reach this tuning range with edge-emitting lasers, but vertical-cavity surface-emitting lasers (VCSELs) exhibit enough inherent wavelength tuning with the injected electrical current due to ohmic heating of the small volume of the device. VCSELs are commercially available in the AlGaIn(N)As system on GaAs substrate for wavelengths below 1.3µm and in the AlGaInAsP system on InP substrate between 1.3µm and 2µm. For longer wavelengths the AlGaInAsSb system on GaSb substrate would have to be used with AlAsSb/GaSb distributed Bragg reflectors (DBR). Compared to the AlInAs/AlGaInAs-DBRs used on InP substrate they offer a higher index step between the two concerned materials of Δn = 0.62 (InP: 0.28). Therefore, the number of layer pairs required to reach a desired reflectivity is significantly reduced. The reflection spectrum of an AlAsSb/GaSb-DBR n-doped with a concentration of 5×10^{17} cm^{-3} is displayed in Fig. 1a). It exhibits a broad stop band with of 175nm and high reflectivity, here a calculated 99.99% at the center wavelength of 2352nm (0.527eV). The thermal conductivity of ≈ 8 W/Km also outperforms the InP-based DBR (≈ 0.6 W/Km) by over an order of magnitude.

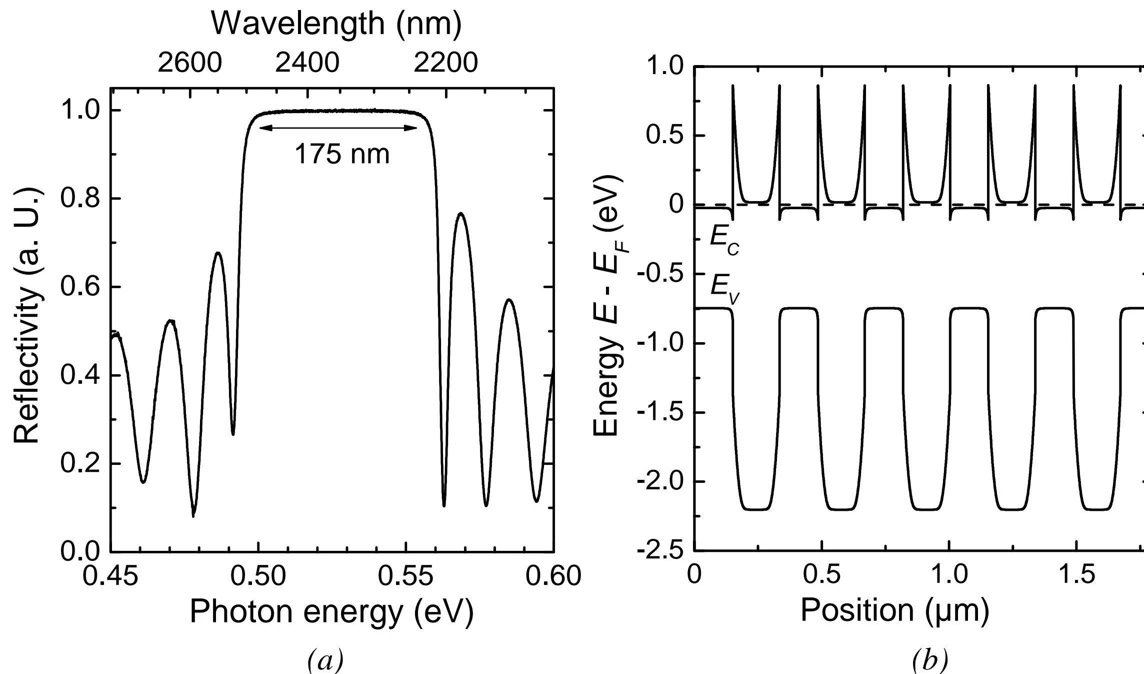

Fig. 1: *(a) Measured reflection spectrum of a DBR with 24 layer pairs of AlAsSb/GaSb, n-doped with tellurium with a concentration of* 5×10^{17} *cm*$^{-3}$*. (b) Corresponding band structure for 5 periods with abrupt interfaces. The band bending at the interfaces leads to the formation of large peaks in the conduction band.*

[1]phone: +49-89-289-12788, fax: +49-89-3206620, email: lauer@wsi.tum.de

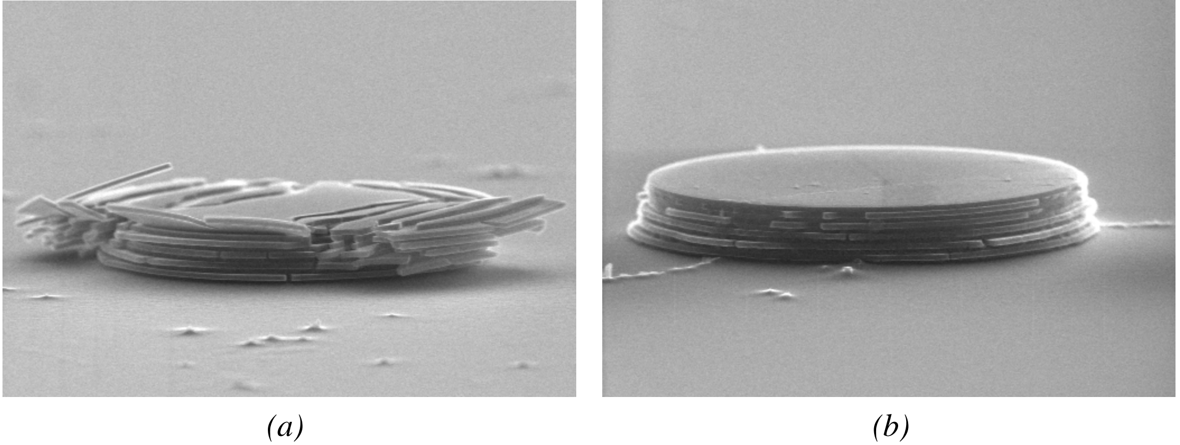

(a) (b)

***Fig. 2:** SEM images of AlAsSb/GaSb-DBR mesas fabricated by dry-chemical etching. (a) After 7 days of exposition to ambient oxygen, lateral oxidation of the Al containing layers and their subsequent expansion have destroyed the initially circular mesa. (b) Coating the mesa slopes with sputtered SiO_2 immediately after structuring of the mesa prevents significant lateral oxidation.*

Unfortunately, the drawback manifests in rather poor electrical performance, giving rise to ohmic losses. Fig. 1b) shows the band structure of several periods of an AlAsSb/GaSb λ/4-layer stack for an *n*-doping level of 5×10^{17} cm^{-3}. The band bending at the interfaces leads to the formation of high and broad peaks in the conduction band, hampering the flow of electrons and causing high electrical resistance. The measured electrical contact resistivity of mesa test structures is as high as 1.2×10^{-5} Ωcm^2 per layer pair for abrupt interfaces between AlAsSb and GaSb. In other material systems the impact of barriers at heterojunctions can be reduced by employing short-period super-lattices (SPSLs) with increased doping at the junctions. These break the band bending into smaller steps or thinner barriers and facilitate tunneling. Unfortunately, it proves difficult to achieve satisfying morphology during growth of such super-lattices in the AlGaInAsSb system. In addition, the doping efficiency of dopant atoms in the host crystal is strongly dependent on the local Al content of the material, which is almost impossible to control in an SPSL. For these reasons first samples with SPSLs at the interfaces exhibited an only marginally improved contact resistivity of 9.3×10^{-6} Ωcm^2 per layer pair. We expect to further decrease the resistivity by a more sophisticated design and improved growth parameters for the SPSLs.

Another problem of the AlAsSb/GaSb-DBRs is the lateral oxidation due to the high Al content. During oxidation the material expands in size by ≈ 20% which destroys the layer stack. We fabricated test structures by etching circular mesas out of an AlAsSb/GaSb layer stack with alternating layer thicknesses of 184nm and 150nm, respectively. Fig. 2a) shows a scanning electron microscope (SEM) image of a mesa containing 5 layer pairs. The stack was almost completely destroyed after exposition to ambient air for only one week. Coating the slopes of the mesas by 50nm of rf-sputtered SiO_2, immediately deposited after the structuring of the mesas, effectively inhibited lateral oxidation. A mesa of a corresponding sample is shown in Fig. 2b), also after one week of exposition to ambient oxygen. Fig. 2b) illustrates the importance of preventing Al containing layers from having contact with oxygen during the processing of devices.

Biochemical Semiconductor Applications

Light-induced manipulation of DNA on amorphous silicon surfaces

Marco Höb[1], Martin S. Brandt, and Martin Stutzmann

As one of the most interesting biomolecules, DNA is currently subject to intensive research. For about one decade, single molecule manipulation has been possible using optical tweezers, which allowed many properties of DNA to be explored. Lately, interest focuses on lab-on-a-chip technologies making use of electrokinetic forces to transport, segregate or concentrate DNA. In this context we explored new possibilities to manipulate DNA through electric fields.

In principal objects can be manipulated in an electric field due to two physical processes: Electrophoresis, where a dc electric field couples to the charge of DNA molecules or dielectrophoresis (DEP), where the induced dipole moment couples to an ac field. To realize an optical tweezer based on electric fields, we have developed a setup for the manipulation of DNA based on photo-induced changes of the conductivity of hydrogenated amorphous silicon (a-Si:H), which allows the electric field distribution to be tailored at will.

Central parts of the setup are electrodes consisting of hydrogenated amorphous silicon on highly doped zinc oxide (ZnO), as schematically depicted in Fig. 1. In darkness, the semiconductor layer behaves like an insulator with a typical conductivity between 10^{-8}-10^{-10} $(\Omega cm)^{-1}$. In contrast the conductivity of the electrolyte used between the semiconductor and the Pt counter electrode is about $0.8 \cdot 10^{-6}$ $(\Omega cm)^{-1}$. Accordingly, an applied ac voltage mainly drops across the amorphous silicon layer and the electric field in the electrolyte effectively vanishes. The situation changes significantly when we illuminate the semiconductor with a focused laser beam. Local illumination at a wavelength of 685 nm increases the conductivity of the a-Si:H layer by several orders of magnitude and leads to the formation of a 'virtual electrode'. Combining this with the counter electrode and applying an ac voltage, we can generate an inhomogeneous electric field distribution in the electrolyte with the help of the laser.

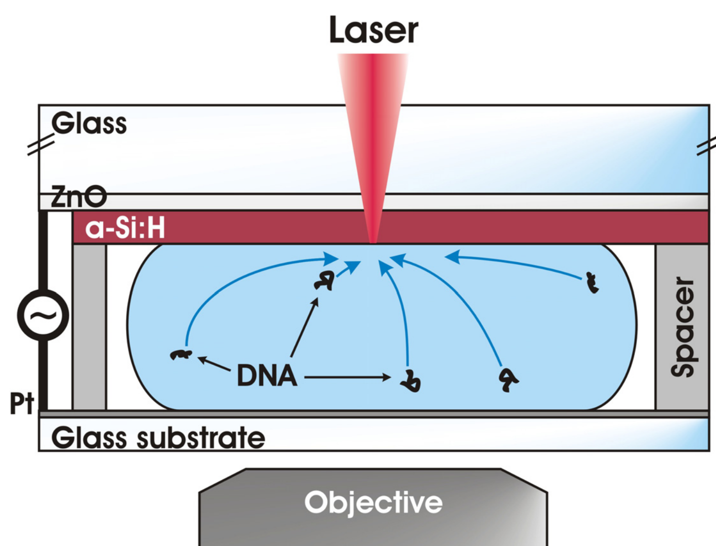

Fig. 1: *Schematic diagram of the experimental setup used to observe light-induced dielectrophoretic motion of DNA molecules.*

[1]phone: +49-89-289-12739, fax: +49-89-289-12737, email: hoeb@wsi.tum.de

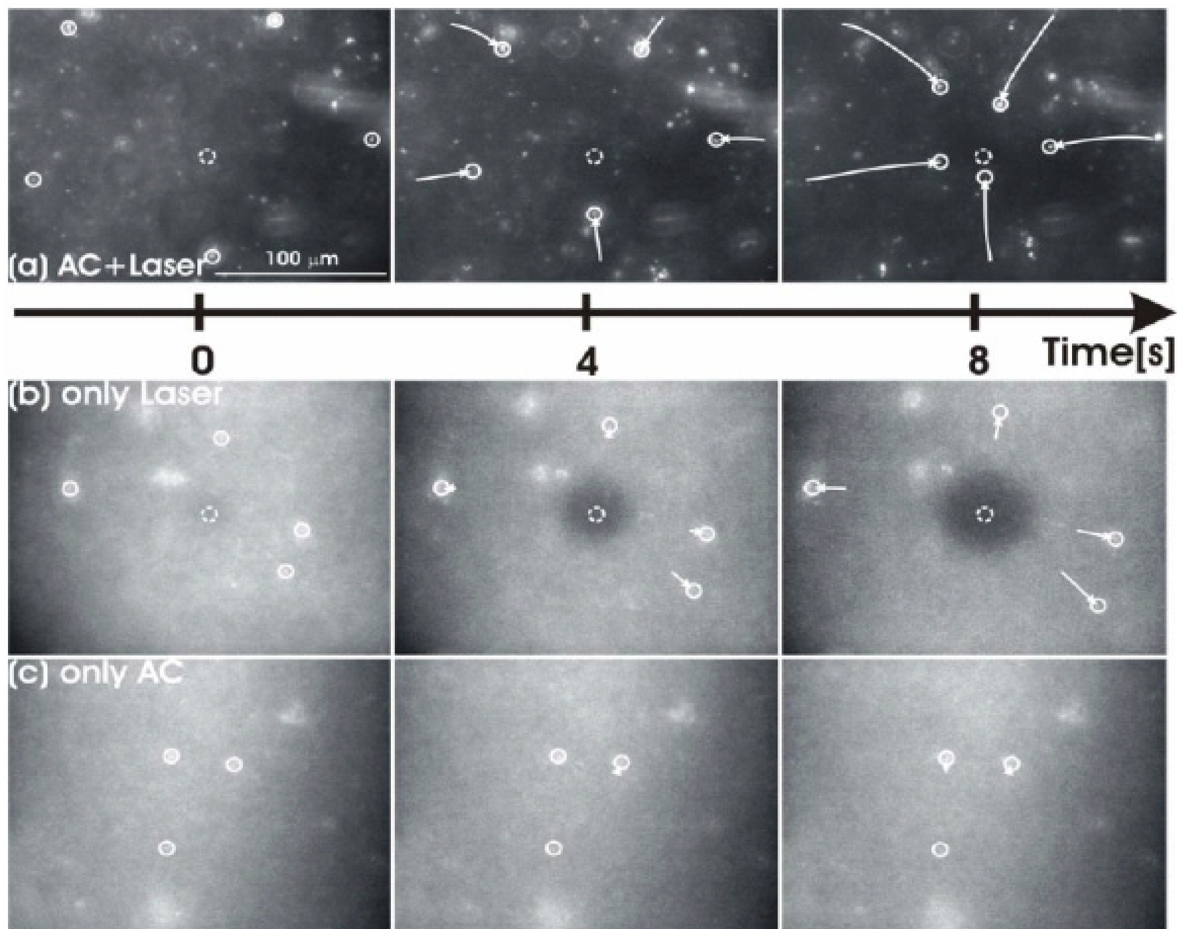

__Fig. 2:__ Motion of DNA molecules. The arrows indicate the spatial change of the DNA position (closed circles) with respect to the first picture. (a) Under illumination and applied ac voltage, the macromolecules move to the laser spot (dashed circle) driven by dielectrophoretic forces. (b) and (c) show the same sequence with only ac voltage or laser illumination, respectively. In both cases, the molecules are not attracted to the center.

An inhomogeneous ac electric field such as generated in the manner described, creates a dipole moment in a polarizeable object like DNA, which, dependent on the frequency of the ac voltage, leads to dielectrophoretic forces, which push the dipole towards strong (positive DEP) or weak (negative DEP) field regions.

Using this setup on a fluorescence microscope, we have observed light-induced dielectrophoresis of biomolecules for the first time as shown in Fig. 2. At a frequency of 200 kHz and a peak-to-peak voltage of 10 V, the DNA molecules are attracted to the high field region, represented by the laser spot.

---

supported by SFB 563, Teilprojekt B2

Kinetic behavior of electrically manipulated DNA tethered to a gold surface

Ulrich Rant[1], Kenji Arinaga[1,2], Marc Tornow[1], Yong Woon Kim[3], Roland R. Netz[3], Shozo Fujita[2], Naoki Yokoyama[2], and Gerhard Abstreiter[1]

We report on the electrical manipulation of single and double stranded oligodeoxynucleotides which are end-tethered to gold surfaces in electrolyte solution. The response to alternating repulsive and attractive electric surface fields is studied by time resolved fluorescence measurements, revealing markedly distinct dynamics for the flexible single stranded and stiff double stranded DNA, respectively. Hydrodynamic simulations rationalize this finding and disclose two different kinetic mechanisms: Stiff polymers undergo rotation around the anchoring pivot point; flexible polymers, on the other hand, are pulled onto the attracting surface segment by segment.

The intrinsically negatively charged DNA is either repelled from, or attracted to the surface upon inducing a charge reversal on the electrode. Information about the position of the DNA's top end with respect to the surface is obtained by optical means. Owing to non-radiative energy transfer to the metal substrate, the fluorescence intensity (F) emitted from the fluorophores attached to the DNA's top end depends on their distance (d) to the surface.

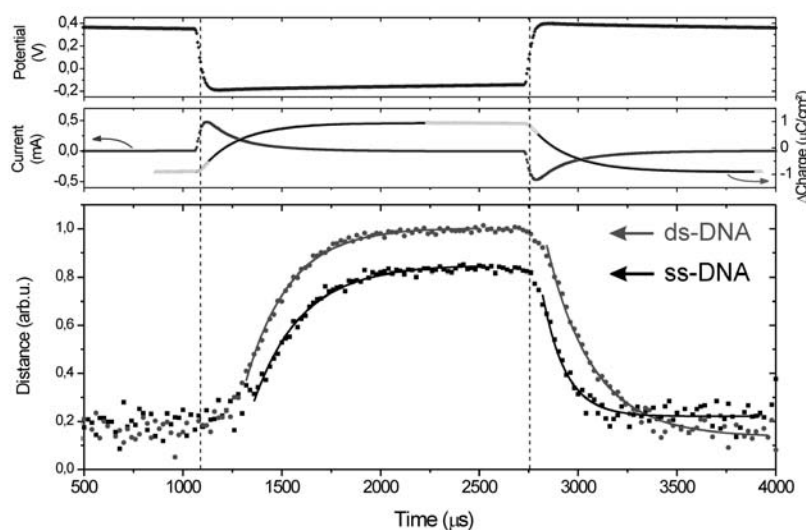

Fig. 1: Time resolved measurements of the electrically induced, mechanical switching of a 48 mer oligonucleotide layer in electrolyte solution. Upper panels: electrochemical response of the electrode. Lower panel: distance of the DNA's top end to the surface, inferred from the measured fluorescence intensity. Solid lines are single exponential fits.

In order to elucidate the dynamics involved in the molecular switching process we present the time resolved response of a 48 mer DNA layer to a square wave bias potential

[1] WSI. Corresponding author: UR, phone: +49-89-289-12776, email: rant@wsi.tum.de
[2] Fujitsu Laboratories Ltd. Japan
[3] Physik Department, Technische Universität München

which is applied to the supporting electrodes. A potentiostat, driven at 300 Hz, is used to control and measure the potential of the gold electrode (topmost panel in Figure 1). The applied bias steps induce charge reversals on the polarizable electrode as revealed by peaks in the electrochemical current (middle panel in Figure 1). Integrating the current over time yields the difference in charge which has been accumulating at the electrode surface. We assign the transient currents to the transport of ions from the bulk solution to the electrode interface, that is, the build-up of the electrochemical ‘double-layer’, which constitutes the polarization of the interface on the solution side.

In order to understand the observed difference in the motion of ss- and ds-DNA, we performed Brownian dynamic simulations treating the DNA as a chain of elastically connected beads with full hydrodynamic interactions between monomers. We find good qualitative agreement between experiment and simulation: the ensemble layer height for repulsive potential is reduced for ssDNA compared to dsDNA and the shape of the averaged transitions resembles the experimentally observed features.

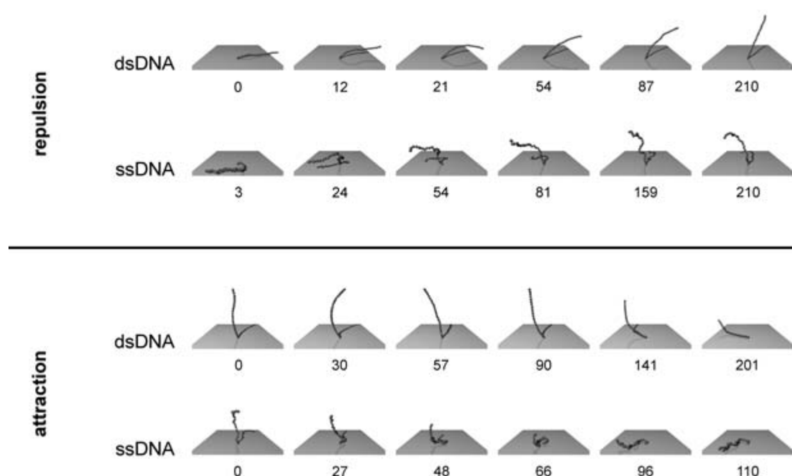

Fig. 2: *Representative snapshots of the simulation data. The numbers denote timing information in units of 10^3 simulation steps.*

The electrical manipulation of the oligonucleotides’ conformation relies on the enhanced field within the ionic polarization layer (double-layer) in solution; thus, the electrically induced motion of DNA at the interface is correlated to the characteristic charging time of the electrochemical double layer. The equilibrium conformations for repulsive and attractive surface fields as well as the dynamic transitions between them are predominantly governed by interactions of the short-ranged electric field with merely a few DNA segments which are closest to the surface. For that reason, the stiffness of the polyelectrolyte largely determines its behavior on the surface; for instance, rigid dsDNA can be aligned more efficiently by repulsive electrode potentials than flexible ssDNA.

The dissimilar dynamic behavior which is observed for ss- and dsDNA can be related to the distinct flexibilities of the molecules. When switching from repulsive to attractive surface potentials the molecular kinetics are particularly interesting: whereas the orientation of the rigid dsDNA is governed by stochastic motions before it ‘tips over’ and falls onto the surface, the flexible ssDNA shows a sudden onset and swift transition from an extended to a condensed state on the surface. It is facilitated by an efficient ‘pulling’ of the lowest nucleotides by virtue of the short-ranged field.

supported by Fujitsu Laboratories Ltd.

Controlling the surface density of DNA on Au by electrically induced desorption

Kenji Arinaga[1], Ulrich Rant, Jelena Knezevic, Erika Pringsheim, Marc Tornow, and Gerhard Abstreiter

Self-assembled DNA layers on solid surfaces have been of great interest and widely introduced to various techniques for bio-molecular investigations. Recently, we have investigated the active electrical manipulation of oligodeoxynucleotides on Au, employing optical measurements to probe the orientation of the surface grafted DNA strands. We showed that the packing density within the DNA layer crucially determines the free mobility of individual DNA molecules on the surface [1] which could work as a probe layer or a support layer of the probe for biosensors based on DNA layers. Further, it means that this parameter has a considerable influence on the functionalities of the probe layers and the accessibility of target molecules. While this parameter bears a particular significance, very few investigations have been reported that address methods for controlling the surface density of DNA on Au.

We have already demonstrated that the surface density of thiol-derivatized DNA on Au can be controlled by changing the immersing time or/and salt concentration in DNA containing aqueous solution [2]. Since the adsorption of molecules on substrates strongly depends on these parameters (time and concentration), it is still very challenging to control extremely low surface densities, which has recently been recognized to be very important for bio-sensing schemes using molecular motion.

Here, we introduce an accurate control method based on the electrically induced desorption of tethered molecules. It enables us to exactly achieve a desired low surface density of DNA with very good reproducibility.

In our measurements DNA is tethered on Au by a thiol linker, which is attached on one end of the DNA, using S-Au bond. On the other end, a fluorescence dye marker, which enables us to observe conformational changes and desorption of DNA from the surface, was attached [1].

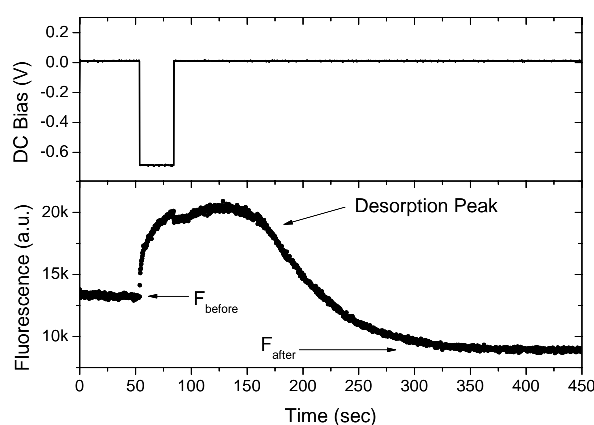

Fig. 1: *Electrically induced desorption of ds-48mer DNA on Au under negative DC bias (-0.7V).*

Figure 1 shows a typical desorption peak under the influence of negative bias pulse (-0.7 V). Before applying the pulse, fluorescence from initially adsorbed DNA is observed (F_{before}). During negative DC bias, a strong desorption peak is observed. The desorption signal continues while the DNA diffuses out of the detection volume. Finally, fluorescence reaches the decreased value (F_{after}) corresponding to the amount of the desorbed DNA ($F_{before} - F_{after}$). DNA is tethered by S-Au bond which involves the

[1]phone: +49-89-289-12775, fax: +49-89-3206620, email: arinaga@wsi.tum.de

oxidation of S. Under conditions of negative DC bias, the S-Au bond can be broken by electrochemical reduction of S. Further, DNA is highly negatively charged along its phosphate backbone in aqueous solution, and therefore is repelled from a negatively charged surface, which facilitates rupturing the Au-S bond.

Figure 2 depicts the desorption ratio for DNA of different lengths (ds-24mer and ds-48mer). Here we define the desorption ratio as the normalized difference between F_{before} and F_{after} by F_{before} as can be seen in the insert in Fig. 2. The shorter DNA (ds-24mer) already reaches a saturated desorption rate at -0.7 V, while in case of longer DNA saturation cannot be observed in Fig. 2. When DC bias is applied to the substrate in electrolyte solution, ions redistribute in the interface region and form the double layer. Due to the screening effect of ions, electric potentials decay rapidly within short distance. In case of the present measurement condition (monovalent salt concentration: 60 mM), almost no electric field exists at the distance of 10 nm from Au surface. Considering the different length of DNAs (ds-24mer ≈ 8 nm, ds-48mer ≈ 16 nm), a large part of shorter DNA is located in the electric field. On the contrary, the longer DNA can not feel the electric field with whole part. Consequently, the shorter DNA can get out from DNA layer and diffuse out from the surface. In addition, a diffusion velocity of shorter DNA is higher than that of longer DNA. It can explain the efficient desorption in ds-24mer DNA, while still increasing the desorption rate in ds-48mer DNA.

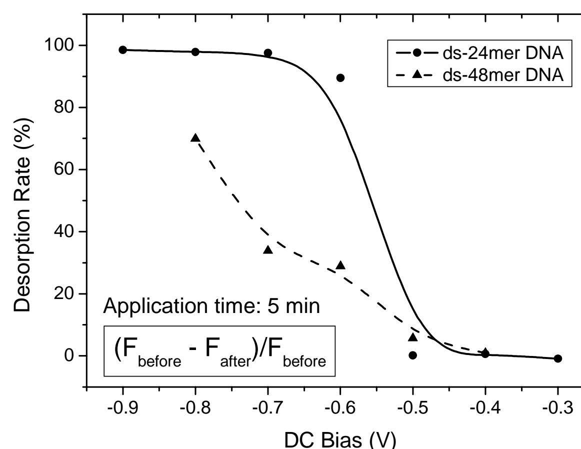

Fig. 2: Desorption ratio of ds-24mer DNA and ds-48mer DNA under different DC bias.

Figure 3 compares the fluorescence intensity with the electrochemically measured surface density from samples prepared by electrical desorption. The proposed method enabled us to vary the surface coverage in the range between 8×10^{10} cm^{-2} and 1×10^{12} cm^{-2}.

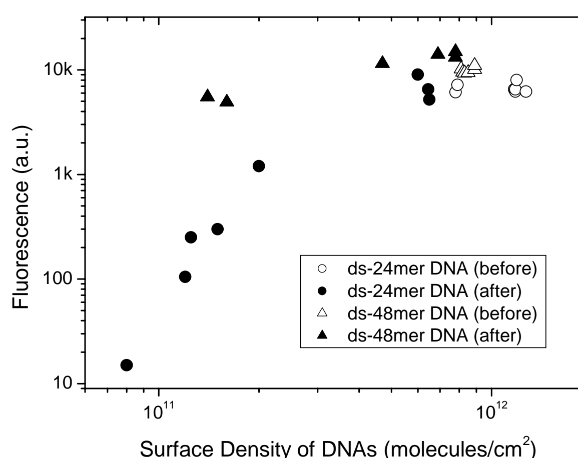

Fig. 3: Fluorescence vs. Surface Density of DNAs which were achieved by electrically induced desorption.

[1] U. Rant et al., Nano Letters 2004, 4, 2441.

[2] K. Arinaga et al., WSI-Jahrbuch 2003

supported by Fujitsu Laboratories of Europe and DFG (SFB563)

Functionalization of ultrananocrystalline diamond thin films by biphenyl diazonium cations

Simon Quartus Lud[1], José Antonio Garrido Ariza, and Martin Stutzmann

Diamond offers several potential advantages as a platform material for bioinorganic interfaces, including chemical and biological inertness. A growing field of interest has been the development of so-called third generation biosensors, which are based on the rapid electron transfer between an immobilized electrocatalytic enzyme and the sensor surface. The electrochemical activity, e.g. electron-transfer processes between the enzyme and the electrode, can be accelerated with covalently attached biphenyl-rings on the diamond substrate mimicking the photosynthetic antenna complex in nature.

We have investigated the grafting of ultrananocrystalline diamond films with highly reactive 4-nitro-biphenyl-4-diazonium cations on 200 nm thick CVD ultrananocrystalline diamond layers. Ultrananocrystalline diamond consists of 5 nm sized grains of sp^3 bonded carbon, separated by mainly sp^2 bonded carbon, so-called high energy grain boundaries. XPS results indicate a sp^2 carbon content of 5 % within the hydrogenated UNCD surface.

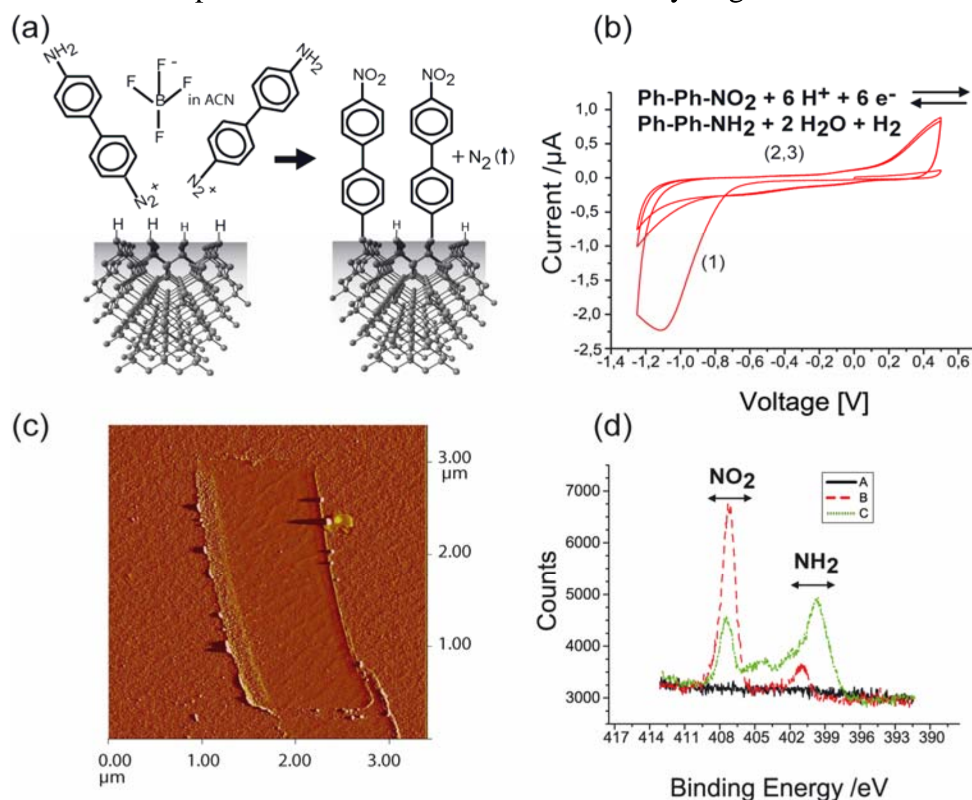

Fig. 1: *(a) Scheme of the grafting process used for chemical functionalization of the diamond surface performed in acetonitrile. (b) Cyclic Voltammetry of a functionalized electrode. The reduction peak in the first scan can be assigned to the reduction of the nitro end groups. (c) Tapping mode AFM image of a trench in the biphenyl layer formed by contact mode AFM. (d) N1s XPS Spectra of three different samples: A hydrogenated sample, B functionalized sample, C functionalized electrode which was used to perform the CV experiments.*

[1]phone: +49-89-289-12765, fax: +49-89-289-12739, email: lud@wsi.tum.de

The formation of a covalently bonded organic monolayer of biphenyl diazonium salts was observed and characterised by cyclic voltammetry, AFM and XPS measurements. From the N/C atomic peak ratio of 1/12 the surface coverage is estimated to be 63 %, additionally an increasing sp^2 peak in the C1s spectra, data shown, also indicates the existence of a monolayer. In electrochemical studies the surface grafted nitro-biphenyl groups could be reduced to amino groups. The first CV scan (1) in *Fig.1b* shows a cathodic current peak. This reduction peak disappears in the following scans (2,3), indicating an irreversible electrochemical reduction. The measured charge consumption leads to a coverage of 73 % with nitro groups, if a six electron process is assumed for the reduction according to Jian and co-workers. Primary amine groups are also an attractive starting point for further chemical modification of diamond surfaces.

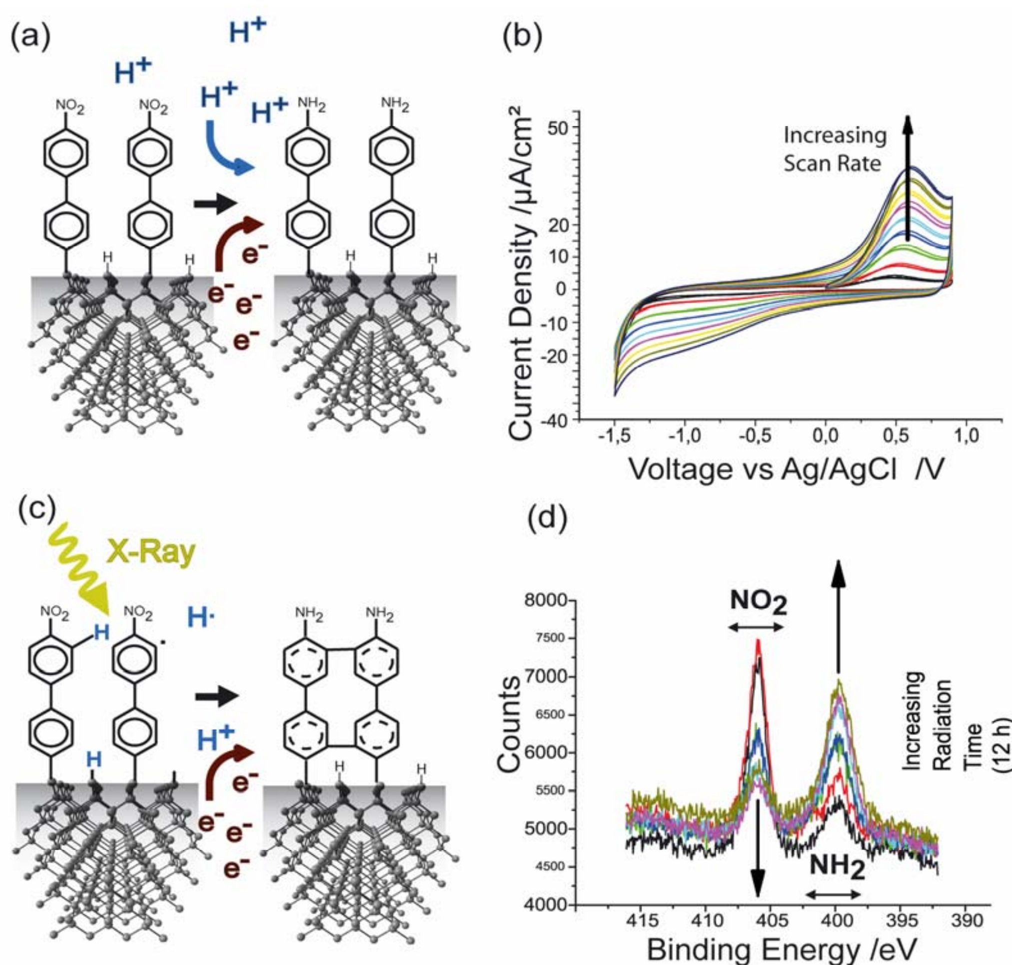

Fig. 2: *(a) Scheme of the reduction process occurring in electrolyte solution at negative apllied potential. (b) Cyclic Voltammetry of a converted electrode showing a reversible oxidation reduction peak with a broadened corresponding reduction peak. (c) Mechanism of radiation induced conversion and cross-linking of the 4-nitro-biphenylfilm. (d) Time evolution of the N1s region of a functionalized sample.*

The nitrobiphenyl groups could also be reduced by x-ray or e-gun radiation. Even though X-rays interact only slightly with matter, they generate primary and secondary electrons inducing a cross-linking process involving radical hydrogen or protons from bond scission of surrounding phenyl rings caused by the ionizing radiation.

This work was supported by SFB563 B15

Characterization of a chemically passivated GaAs based sensor device in electrolytes

Sebastian M. Luber[1], Daniel Gassull[2], Dieter Schuh, Motomu Tanaka[2], Marc Tornow, and Gerhard Abstreiter

Functionalized field effect devices are promising candidates to act as smart substrates for sensor applications. For a use in biological systems a functional layer has to provide stability against electrochemical decomposition, and allow effective coupling of the surface potential to the conductive channel. We investigated a resistor device passivated with a 4'-substituted 4-mercaptobiphenyl (MBP) self-assembled monolayer (SAM) for sensing applications. Base material was a GaAs-AlGaAs heterostructure containing a quasi 2D electron gas 60nm beneath the surface.

In the first part of our study we focused on the enhanced stability of mercaptobiphenyl coated devices in aqueous environments. Two substitutional groups were investigated (methyl ($-CH_3$) and hydroxyl (-OH)). Comparable measurements of the coated and uncoated samples in phosphate buffered salt solution (PBS) clearly demonstrated the enhanced stability of the passivated samples. As examples of the results obtained, figure 1 compares the resistance of the unpassivated and passivated samples as a function of time.

The enhanced stability enabled a systematic investigation of the influence of the pH-value of the electrolyte solution onto the surface potential of the sample. To do this, we recorded the resistance change of the 2DEG in a PBS solution and varied the pH value by titration. By using a reference measurement we could extract a value for the equivalent sample potential as a function of the pH value. For both samples a linear variation of the sample potential with pH was observed (not shown). The observed effective modification

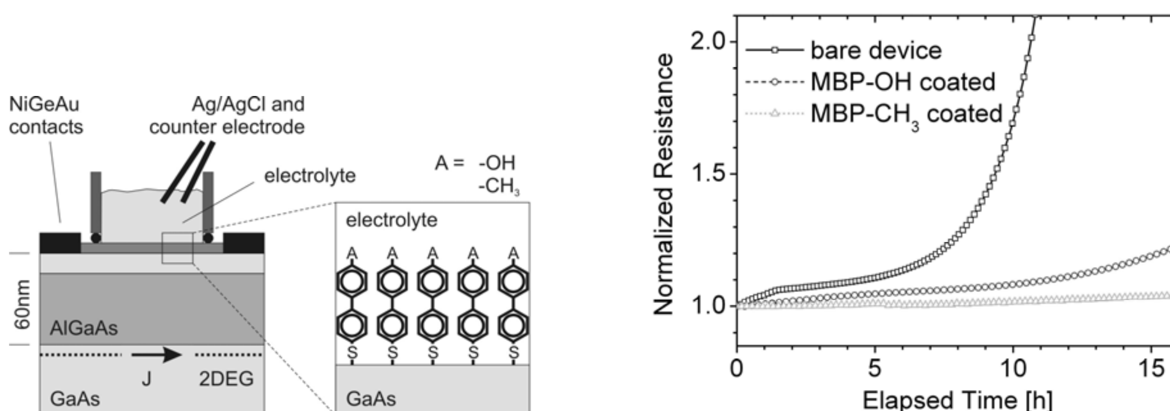

Fig. 1: *Left panel: Schematic representation of the GaAs-AlGaAs heterostructures investigated containing a near surface 2DEG. The figure also shows schematically the experimental geometry used.*

Right panel: Characteristic time dependent variation of the sample resistance in 10mM phosphate buffered salt solution (PBS, 100mM NaCl, pH = 6.8), comparing an uncoated sample (-□-) with a MBP-CH_3 (-Δ-) and a MBP-OH (-○-) coated sample. The potential of the samples were held at -0.4V relative to the Ag/AgCl electrode.

[1]phone: +49-89-289-12776, fax: +49-89-320-6620, email: luber@wsi.tum.de
[2]Lehrstuhl für Biophysik – E22, TU München, 85748 Garching

of the sample potential can be explained by a pH dependent modification of the surface charge. For most surfaces, the site-binding model is applicable. This approach treats the positive charging as a result of binding of protons to OH-groups of the surface and the negative charging as a result of loss of protons with associated reaction constants K_a and K_b. For the MBP-CH_3 coated sample the reaction of the H^+ ions with the apolar endgroups of the passivation layer is expected to be highly unlikely. Instead, the adsorption of OH^- groups onto a hydrophobic surface, described by a "Stern" adsorption layer, can be a very probable mechanism. Both models allow for an interpretation of the experimentally measured values for the MBP-CH_3 passivated sample. Figure 2, left panel, compares experimental data with the curves deduced from the models. What speaks against the site – binding model are the large values of the density of surface sites N_S, which had to be assumed in the simulations. Even if every atom of the GaAs crystal surface would be available for a charging reaction, the resulting value of $N_S \sim 3 \cdot 10^{14}$ /cm² would still be smaller by one order of magnitude compared to the model calculation.

We also investigated the response of the 2DEG sensor vs. changes of the salt concentration at constant pH. Figure 2, right panel, shows the results of model calculations together with experimentally determined values at three different pH values for a MBP-CH_3 passivated device. Surprisingly, a very good agreement between experiment and simulation is obtained when assuming the surface charge as independent of salt concentration, i.e. neglecting the models described above. However, a mechanism that could induce such effect is not evident. A possibility would be the additional adsorption of counter-ions onto the surface. For a comprehensive assessment further simulations will be required. Moreover, the influence of additional constant surface charges arising from occupied GaAs surface states has not yet been investigated.

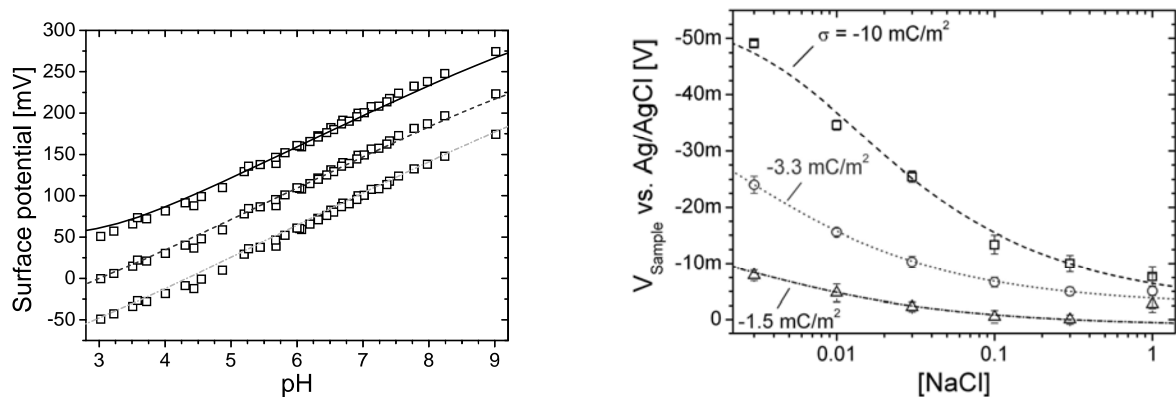

Fig. 2: *Left panel: Comparison of experimental data of a MBP-CH_3 passivated sample (□) (in 1mM PBS with 100mM NaCl with results of simulations of Stern Adsorption (—) and site – binding models (1: – – und 2: −·−). Used parameters: —: $N_S = 2 \cdot 10^{15}$ /cm², pK_a = 5.4; – –: $N_S = 2 \cdot 10^{15}$ /cm², pK_a = 5.4, pK_b = -0.6; −·−: $N_S = 4 \cdot 10^{14}$ /cm², pK_a = 7.5 , pK_b = -4.5; N_S is the maximal surface density of adsorbed ions.*

Right panel: Salt dependence of the equivalent surface potentials of a MBP-CH_3 passivated sample at different pH values in 1mM PBS: pH 7.0 (□); pH 5.1 (○) and pH 3.3 (Δ). The curves are simulations according to the Poisson-Boltzmann theory assuming a salt independent surface charge.

supported by the DFG (SFB 563 B1) and in part by the Fujitsu Laboratories of Europe

Enzyme-modified AlGaN/GaN field effect transistors

Barbara Baur[1], Yvonne Gawlina, Georg Steinhoff, John Howgate, Hans-Georg von Ribbeck, Martin Stutzmann, and Martin Eickhoff

Since Bergveld introduced the first miniaturized semiconductor-based biochemical sensor in 1970, potentiometric biosensors based on ion sensitive field effect transistors (ISFETs) have been developed in numerous studies. These devices represent functional hybrid systems consisting of two basic components, the bioreceptor and the electrochemical transducer. As enzymes provide the capability of specific recognition and catalytic activity, the concept of enzyme based field effect transistors (EnFETs), first realized in 1980 by Caras and Janata, attracts considerable attention for biomedical applications.

AlGaN/GaN electrolyte gate field effect transistors (EGFETs) are promising devices for electronic detection of biochemical processes, as they combine excellent electronic characteristics with long term stability in liquid electrolytes. In addition, they show a high pH sensitivity, allowing quantitative monitoring of enzymatic reactions accompanied by local pH changes (Fig. 1). For this purpose, penicillinase as a suitable model system was immobilized on AlGaN/GaN EGFET gate areas.

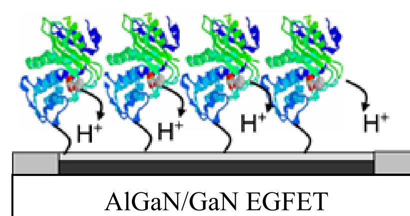

Fig. 1: *Structure and principle function of an enzyme modified AlGaN/GaN FET. The enzyme is immobilized on top of the pH sensitive gate*

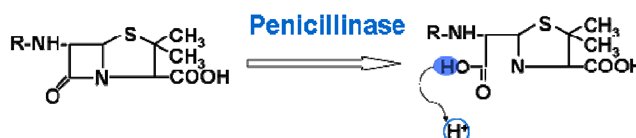

Covalent immobilization of enzymes on GaN-surfaces was carried out by Schiff base formation using glutaraldehyde as crosslinker[2]. For comparison, physisorption of penicillinase was achieved by incubating the pure GaN-surface in enzyme solution.

In the case of covalent immobilization, fluorescence microscopy indicates the specific chemical binding of enzymes on glutaraldeyde modified surface areas, whereas the non-specific physisorption due to electrostatic interaction is suppressed (Fig. 2).

The biocatalytic activity of immobilized penicillinase is detected electronically, employing the ion sensitivity of the underlying AlGaN/GaN EGFETs (3 nm GaN / 25 nm AlGaN barrier / 3,8 µm GaN buffer, $n_{2DEG} \approx 0.8\text{x}10^{13}$ - $1.2\text{x}10^{13}$ cm^{-2}, $\mu \approx 1000$-1500 cm^2/Vs) The channel width of the mesa structured functionalized gate area was 0.5 mm, the length of the exposed gate area ~ 1.2 mm after encapsulation.

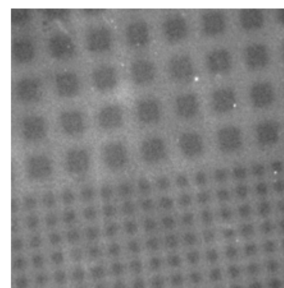

Fig. 2: *Fluorescence image of covalent immobilized penicillinase on a microstructured, silanized GaN surface[4].*

[1]phone: +49-89-289-12769, fax: +49-89-289-12737, email: barbara.baur@wsi.tum.de

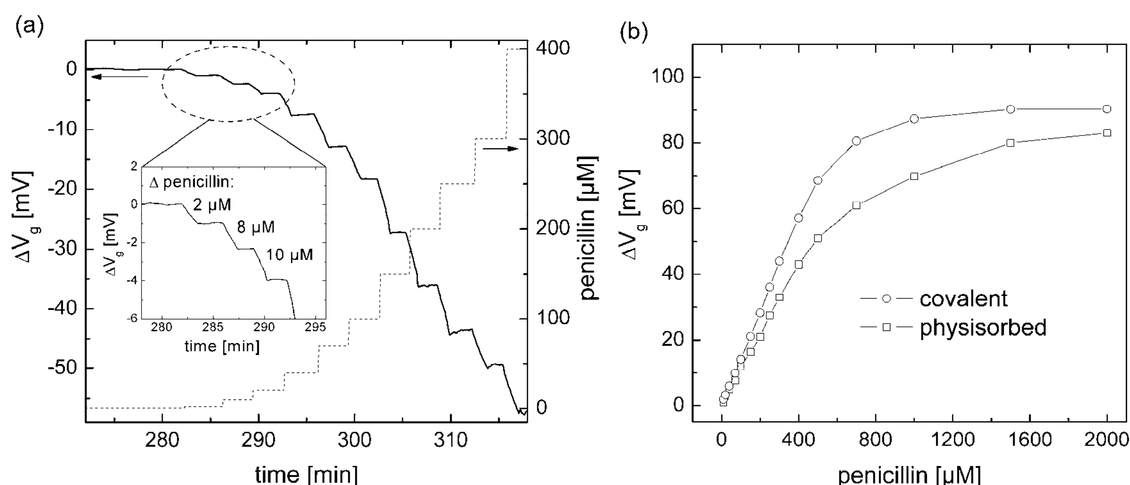

Fig. 3: *(a) Transient response of present AlGaN/GaN penicillin EnFET with a covalently immobilized enzyme monolayer. The detection limit of penicillin is 2 µM as demonstrated in the inset. (b) Calibration curves of penicillin EnFETs prepared by covalent bonding (circles) versus physisorption (squares).*

All measurements were carried out using a three electrode setup where the EnFET (working electrode) was operated with a constant drain-source voltage. In the computerized measurement the channel current was kept constant and the respective change of the surface potential applied via the electrolytic gate was monitored as the output signal (ΔV_G). Glutaraldehyde modified EGFETs exhibited a slightly smaller pH sensitivity of 54 mV/pH than untreated devices (56 mV/pH)[3].

Electronic measurements of the enzyme activity were performed in a sodium phosphate buffer solution (pH 7, 0.5 mM) by titration with penicillin solution in different concentrations. Figure 3(a) shows the transient response of an AlGaN/GaN EnFET with a covalently immobilized enzyme monolayer. An almost immediate response is observed and penicillin concentrations as low as 2 µM can still be resolved. The calibration curves, shown for a sample with covalent immobilization versus a sample with simple physisorption in Fig. 3(b), exhibits a linear dependence of the output signal at low substrate concentrations (2 µM – 500 µM) revealing a sensitivity of 0.14 mV/µM and 0.10 mV/µM, respectively[4]. For high substrate concentration the response signal tends to saturate. Future work will concentrate on the investigation of the relation between the immobilization process and the enzyme activity.

---

[2]B. Baur, G. Steinhoff, J. Hernando, O. Purrucker, M. Tanaka, B. Nickel, M. Stutzmann, and M. Eickhoff, Appl. Phys. Lett. 87, 263901 (2005)
[3]G. Steinhoff, M. Hermann, W. Schaff, L. F. Eastman, M. Stutzmann, M. Eickhoff, Appl. Phys. Lett. 83, 178 (2003)
[4]B. Baur et al., submitted for publication

supported by the Deutsche Forschungsgemeinschaft (SFB563, B11) and by the European Community within the strategic research GaNano (Contract No. NMP4-CT-2003-505641)

Nano-engineering of III-V semiconductor cleaved planes for molecular electronics applications

Sebastian M. Luber[1], Fan Zhang, Allan Hansen, Simone Lingitz, Felix Scheliga[2], Emma Thorn-Csányi[2], Max Bichler, and Marc Tornow

One of the major challenges to realize molecular electronic hybrid systems that comprise molecules as functional units is the reproducible fabrication of the inorganic contact electrodes. These 'nanogap electrodes' have to be prepared such that they allow for a reliable contacting to molecules with a predetermined spacing on the nanometer scale.

We have been developing a novel technique to prepare nanogap electrodes in a very precise manner, based on GaAs/AlGaAs heterostructures grown by MBE. As illustrated in Fig. 1, a few nm thick layer of GaAs is embedded into a 1500nm thick $Al_{0.3}Ga_{0.7}As$ MBE grown layer. After lateral patterning of the heterostructure by conventional optical lithography and deposition of Ti/Au metal contact pads the sample is cleaved, exposing an atomically flat and perfectly clean (110) surface of the AlGaAs-GaAs sandwich structure. After that, the embedded GaAs layer is etched selectively versus the outer AlGaAs layers using a wet chemical etchant. A subsequently deposited thin film metal layer already forms the contact pair on the AlGaAs surfaces. These electrodes are macroscopically flat (less than typically 1 nm, as determined by AFM), coplanar and exceedingly clean since being protected throughout the entire photolithographic process. The final gap size between the electrodes is mainly determined by the layer thickness set during MBE growth.

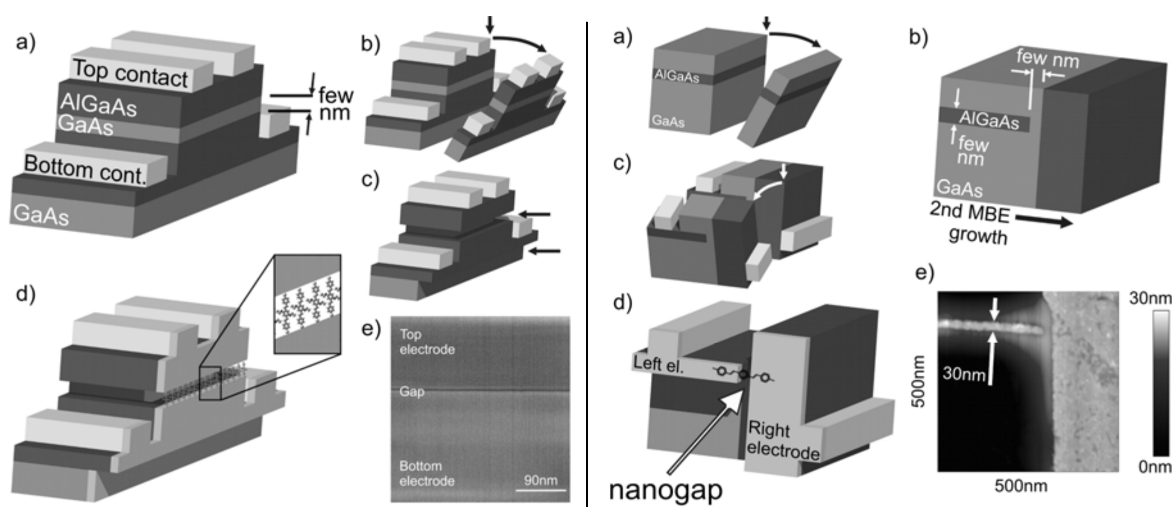

Fig. 1 *(Left): Schematic fabrication of a nanogap device. a) GaAs/AlGaAs heterostructure with contacts. b) Crystal cleavage. c) selective etching of embedded GaAs layer. d) thin film metallization forming the nanogap electrodes, to be bridged by molecules. e) SEM image (30° tilted) of a completely processed 5nm GaAs sample.*

Fig. 2 *(Right): Nanogap electrodes for few molecule measurements by CEO. a) Crystal cleavage in-situ (MBE). b) Regrowth on the cleaved plane. c)2nd cleavage. d) selective etching and metallization. e) AFM image of a CEO sample after selective etching. A ~30 nm wide AlGaAs bar is separated from the opposing AlGaAs plane by ~25nm.*

[1]phone: +49-89-289-12776, fax: +49-89-3206620, email: luber@wsi.tum.de
[2]Technical and Macromolecular Chemistry, University Hamburg

To enable the measurement of a few or eventually a single molecule a further lateral constriction of at least one of the electrodes down to a few nm is required. Fig. 2 shows how such shrinking can be achieved by employing the technique of MBE "cleaved-edge overgrowth" (CEO). After the first epitaxial growth the sample is cleaved in-situ and regrown a second time onto the cleavage plane. The subsequent second crystal cleaving and thin film metallization yields a t-shaped electrode structure with one thin electrode finger opposing a wider contact area, both separated by a few nm only.

π-conjugated, rod-like molecules having an extended, delocalized electron system are best suited as molecular wires bridging the nanogap electrodes. We evaluated the functionality of our devices by carrying out first electrical transport measurements on dithiolated Oligo(*p*-phenylenvinylen) (OPV) derivatives of length 8.5 nm. The molecules were self-assembled on the electrodes from dichloromethane organic solvent. We investigated the properties of the films in advance by ellipsometric thickness experiments on planar Au surfaces. The results were consistent with a ~40° tilted monolayer corresponding to a relative layer thickness of ~0.74 molecule lengths. Fig. 3 shows first current-voltage characteristics on such deposited OPVs on a 5nm GaAs nanogap structure at T=4.2K, compared to the control measurement before assembly. The observed exponential increase of current above approximately ±0.3 V is in good agreement with our recent calculations of the transport properties of a simplified OPV molecule covalently attached to Au electrodes, using available Density Functional Theory, Extended Hueckel Theory and Non-equilibrium Green's function formalism codes (not shown). In a qualitative picture, for low bias voltage the Fermi level (of the metal electrodes) lies within the HOMO-LUMO gap of the molecule which makes tunneling the dominant transport mechanism in this regime. Due to the relatively large electrode distance of the order of 5nm in our case only negligible small current amplitudes can be observed. At higher bias, molecular energy levels successively enter the energy window spanned by the applied voltage allowing for resonant transmission through one or more molecular orbitals.

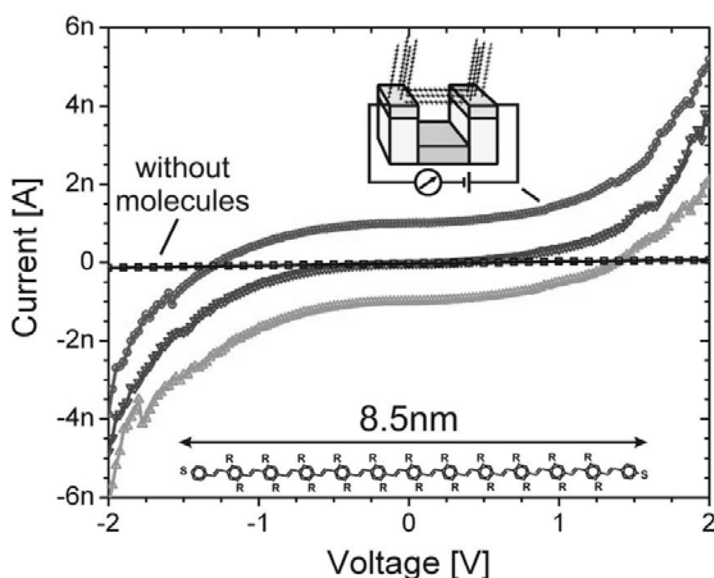

Fig. 3: *Current-voltage characteristics of OPV molecules assembled on a 5nm GaAs nanogap device, in comparison to the non-functionalized case. The three displayed curves were measured consecutively at T=4.2K (shifted vertically by 1nA for visibility). Bottom region of graph: simplified molecular structure of the used OPV. Top: possible molecular configuration in the gap region.*

Supported by the BMBF under grant 03N8713 (Junior Research Group "Nanotechnology") and by the Fujitsu Laboratories of Europe.

Biochemical Semiconductor Applications

The 3D nanometer device simulation project next**nano**++

A. Trellakis[1], T. Zibold, T. Andlauer, S. Birner, R. Morschl, and P. Vogl

next**nano³** is a versatile software for the simulation of nanometer-scale quantum structures and devices. With this simulator, we can calculate the strain and the associated piezoelectric and pyroelectric charges, the electronic structure in external electric and magnetic fields, optical properties such as excitonic energies and transition matrix elements, or also carrier densities and currents. Almost arbitrary device geometries and material compositions consisting of the zincblende or wurtzite crystal systems are supported [1]. In the following, we will outline some of the basic physical concepts and numerical methods that have been developed for next**nano³** or are being developed for the ongoing next**nano**++ project, an international collaborative effort involving many physicists, mathematicians, and programmers. In addition, we will present a few application examples.

The electronic structure is calculated in terms of envelope function in the oneband or multiband k·p-equations. For the latter it is well established that discretization on a grid may result in spurious energy solutions and discontinuities in the wave functions. For this reason, we have developed a new dimension independent box discretization scheme of the multi-band k·p-Hamiltonian that virtually eliminates these problems. Within this method, an artificial diffusion term similar to upwinding schemes is added to the Hamiltonian in order to stabilize the discretization. In addition, the operator ordering employed here avoids singularities in the wave functions.

Another barely recognized problem is that it is numerically extremely difficult to find the correct solution of Schrödinger’s equation in the presence of an external magnetic field. Since the magnetic vector potential is spatially unbounded, every naive discretization of the standard minimal coupling Hamiltonian violate the inherent gauge invariance and consequently leads to huge errors in the numerically obtained solutions. We have developed a gauge invariant discretization scheme of the multiband k·p-Hamiltonian that is based on Wilson’s formulation of lattice gauge theories. This allows us to calculate the electronic structure and the carrier transport even in the quantum Hall regime.

We have developed and implemented various numerical algorithms to improve the performance and stability of the coupled Poisson-Schrödinger system. For example, the extremal eigenvalues of the k·p-Hamiltonian are calculated using ARPACK in conjunction with a spectral transformation based on Chebyshev polynomials in order to emphasize all relevant eigenstates and to suppress all others. For 8-band calculations, the interior eigenvalues and wave functions are needed. In this case we employ a block variation of the Rayleigh quotient iteration. An efficient and stable block preconditioner, which approximately decouples the electronic components from the spatial variations, is then used to invert the resultant indefinite linear system of equations.

Finally, in order to solve the coupled Poisson-Schrödinger system, we employ an approximate quantum charge density inside of Poisson's equation in order to estimate the dependence of the density on the potential through Schrödinger's equation. Using this estimator the coupling between both equations is much decreased and rapid convergence is achieved. Recently, we have refined this technique further by projecting the Hamiltonian

[1]phone: +49-89-289-12741, fax: +49-89-289-12737, email: alex.trellakis@wsi.tu-muenchen.de

into the subspace spanned by all already known eigenvectors, and then diagonalizing this small subspace matrix. With this method only half as much work is needed to obtain the correct solution.

Carrier transport is currently calculated either as ballistic current using the contact block reduction (CBR) method [2] or in terms of an empirical quantum drift-diffusion method. We are currently working on a generalized CBR method that includes scattering within a Büttiker probe model.

In order to achieve a high degree of code reuse we heavily rely on object-orientated programming techniques. An inheritance based class hierarchy combined with the widespread use of C++ templates results into a very efficient and compact implementation without code duplication. All input files use a powerful hierarchical syntax that can easily describe even complicated device geometries. These input files are then parsed using a BISON generated parser module and validated for errors using an approach similar to the one used for validating XML files.

Currently we are using next**nano³** and next**nano**++ extensively to model devices and quantum structures in the Si-SiGe and III-V material systems. Examples for such applications are for instance strained p-channel inversion layers, double gate and wrap-gate MOSFETs (Fig. 1), or also strain-induced T-shaped InAlAs quantum wires, InGaAs/GaAs quantum dot molecules (Fig. 2), and GaN based ISFETs for biosensing applications. CPU time is no longer an issue with next**nano**++, as a self-consistent and fully quantum mechanical 3D electronic structure calculation of a HEMT-type AlGaAs/GaAs device with a total of 4×10^5 grid points requires only about an hour on a standard PC with 2 GB RAM.

The new version next**nano**++ will be made available later this year. In addition to the already extensive documentation tutorials on our website; consulting services are available through Stefan Birner's company next**nano** [1].

[1] See *http://www.wsi.tum.de/nextnano3* for executables and documentation, and *http://www.nextnano.de* for consulting services.

[2] D. Mamaluy, D. Vasileska, M. Sabathil, T. Zibold, and P. Vogl, Phys. Rev. B 71, 245321 (2005), Phys. Rev. B **71**, 245321 (2005).

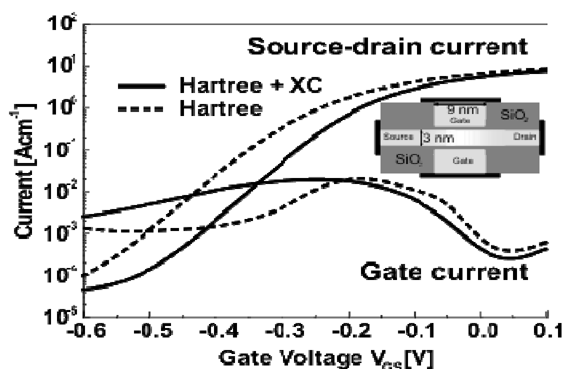

Fig. 1: Quantum drift-diffusion currents for the 9nm DGFET shown in the inset. Results from a pure Hartree calculation and one including exchange-correlation are shown.

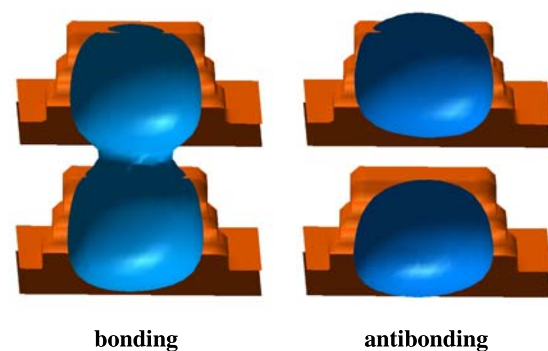

Fig. 2: Isosurfaces of bonding and antibonding electron wave functions in two adjacent InGaAs/GaAs quantum dots 6 nm apart from each other.

Supported by the Deutsche Forschungsgemeinschaft (SFB 631), the Österreichische FWF (Projekt IR-ON F025), and the Office of Naval Research (Contract No. N00014-01-1-0242).

Black silicon surfaces – vanishing reflectivity via nano-scale texturing

Svetoslav Koynov[1], Martin S. Brandt, and Martin Stutzmann

Silicon with various structural morphologies is widely used for applications in solar cells and optoelectronic devices. However, flat Si surfaces have a high natural reflectivity, which requires specific treatments for the minimization of optical losses. Anti-reflection coatings and deep (several µm) surface texturing are commonly used for this purpose. These approaches, however, suffer from a number of optical and technological limitations. An appealing approach is the use of a fine surface texture, comprising features on the nanometer scale. The optical effects of such a texture were first investigated theoretically by Stephens and Cody using the effective medium approximation. They have shown that suitably textured surfaces can exhibit vanishing reflectivity at all wavelengths below a cut-off threshold. Several nano-texturing techniques, based on reactive ion etching (RIE), have been developed recently. However, the ion damage associated with RIE, difficulties with obtaining a uniform texturing and the limited productivity are obstacles for large scale applications.

We have developed a new method for nano-scale texturing of silicon surfaces, which utilizes simple wet chemical etching, enhanced by the catalytic action of small metal clusters. The texturing process, referred to as "black etch" below, is performed in three steps:

i) A small amount of gold is deposited onto the flat Si surface by vacuum evaporation or sputtering to obtain a coverage with a nominal thickness of 1-2 nm. Such ultra-thin layers are discontinuous, comprising clustered Au grains of several nanometer size with about 40% -20% of exposed Si surface between them.

ii) The so prepared Si substrates are etched at room temperature by immersion in a water solution of Hydrofluoric Acid (HF) and Hydrogen Peroxide (H_2O_2). The duration of this step can be controlled visually, as the Si surface turns from highly reflecting to black within 50-90 sec.

iii) Finally, the remaining Au is removed from the textured Si surface by room temperature etching in aqueous solution of Iodine and Potassium Iodide**.**

Figure 1 illustrates the major optical effects of the "black etch" treatment, applied as an

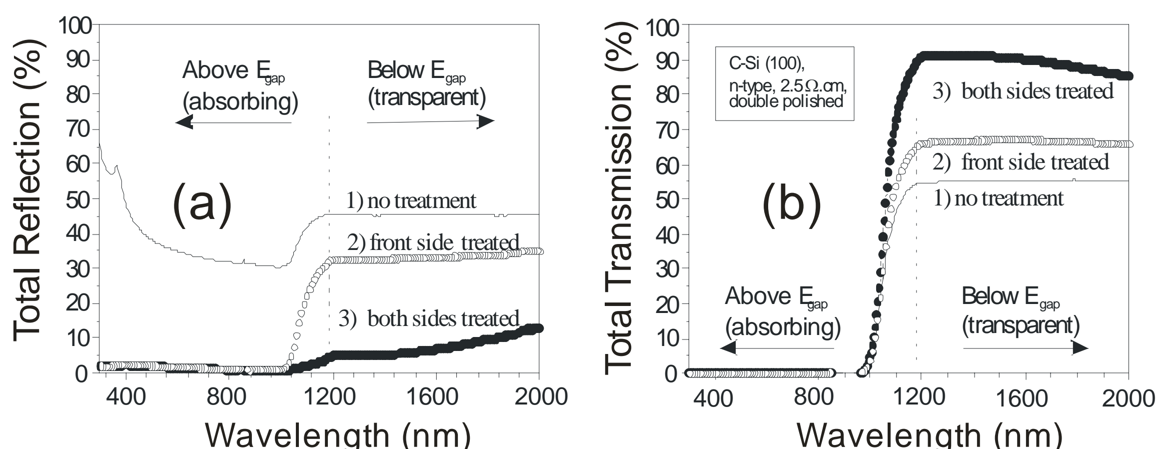

Fig. 1: *(**a**) Total reflection spectra and (**b**) total transmission spectra **of** black etched c-Si surfaces. The spectra were measured with an integrating sphere.*

[1]phone: +49-89-289-12765, fax: +49-89-289-12737, email: koynov@wsi.tum.de

example to a single crystalline Si sample with initially double-side polished surfaces. Figure 1a shows that the black etch treatment results in an almost complete suppression of optical reflectivity in the whole region of Si absorption. A comparison of the reflection and the transmission of all samples in the region of Si transparency indicate that the suppressed reflection of the treated surfaces is accompanied by corresponding increase of the transmission. In the region below E_{gap}, the sum of reflection and transmission for each couple of spectra equals 100%. This clearly demonstrates that there is no additional absorption in the modified surfaces – i.e. they are genuinely anti-reflecting.

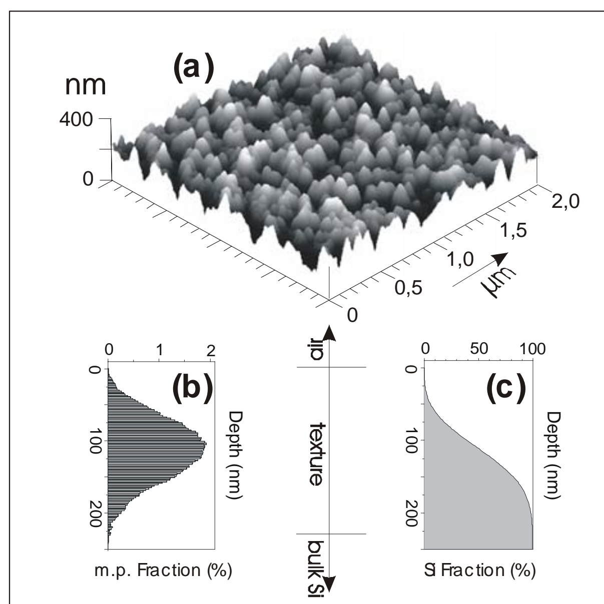

Fig. 2: (a) AFM image of textured c-Si surface. (b) Depth histogram of the image. (c) Variation of the Si fractional area across the textured layer.

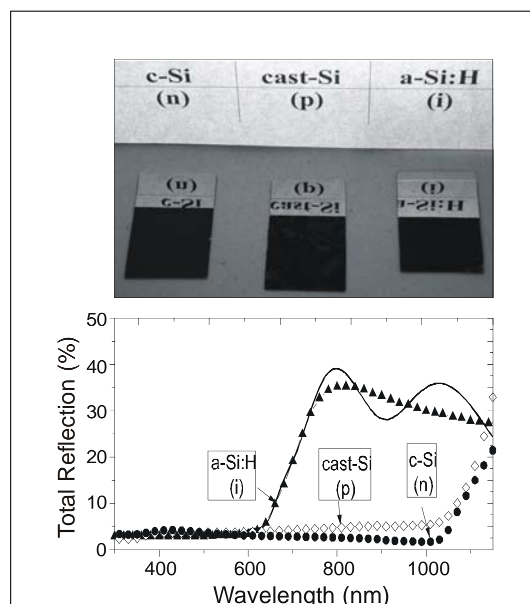

Fig. 3: (a) Photograph of different black Si samples. (b) Total reflection spectra of the treated areas of the same samples.

The origin of the optical effects produced by the "black etch" can be understood from the morphology of the etched Si surface shown in Figure 2. The distinct texture, comprising features of lateral sizes within 50-100 nm range (Fig. 2a) should comply with the effective media approximation. Figures 2b and 2c reveal that the textured surface is a medium with a very smooth increase of density (optical constants) up to 250 nm depth. According to the model of Stephens and Cody, such a graded layer should exhibit a reflectivity cut-off for all wavelengths below the Si absorption edge as observed.

The fact that an up to 250 nm deep Si texture has been formed within 90 seconds of wet etching in the presence of Au clusters, while the etch rate of clean Si in the same etching solution is lower than 1 nm/min, clearly shows the catalytic action of the Au clusters.

Figure 3 illustrates the ability of the "black etch" treatment to produce the desired optical properties on silicon surfaces of different crystalline structure and doping - single crystalline (n), multi-crystalline (p) and even on thin amorphous Si films (500 nm thick-i). Moreover, an apparent red shift of the absorption edge has been observed with thin Si films, which indicates an efficient light trapping. The optical effects, described here, open new opportunities for the design of efficient solar cells and optoelectronic devices.

Micro mechanically tunable long wavelength VCSEL with extended tuning range of 60nm

M. Maute[1], B. Kögel[2], G. Böhm, P. Meissner[2], and M.-C. Amann

Widely tunable long-wavelength vertical-cavity surface-emitting lasers (VCSELs) are highly attractive light sources for telecom applications within wavelength division multiplexing (WDM) systems. Fixed wavelength laser replacement, single transverse-mode operation with high side mode suppression, and high coupling efficiency into an optical fiber are some of the main benefits of those devices. Various monolithic concepts of tunable VCSELs based on a micro-electro-mechanically system (MEMS) have been presented to date. Here, we investigate an approach based on a two-chip concept that allows for a separate optimization of the components. The device (see Fig. 1) consists of a "half-VCSEL" and a movable top mirror membrane.

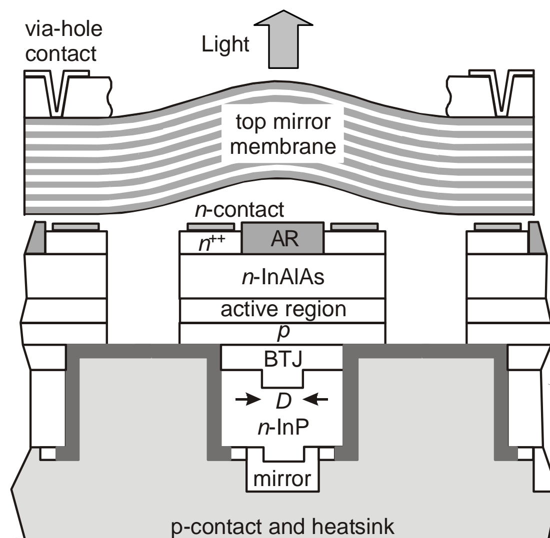

Fig. 1:
Schematic cross section of a tunable two-chip VCSEL.

The current confinement in this structure is realized by the use of a buried tunnel junction (BTJ) of a given diameter *D* and the back reflector is formed by a dielectric mirror. Since the membrane is much bigger in size compared to the half VCSEL surrounding devices are used as a contact surfaced. The micro-mechanically tunable mirror is an MBE-grown ($In_{0.05}$)GaAs/AlGaAs-Bragg-mirror of 22.5 periods leading to a theoretical reflectivity of 99.9%. After defining the shape of the membrane and partial removal of the semi-insulating GaAs substrate the additional 5% indium content in some of the GaAs-layers leads to a stress-gradient and therefore to a rotation-symmetric concave curvature with a radius of about 2-3mm. Due to this curvature the necessary assembling step of the mirror in respect to the active part is rather insensitive to tilt and the variable air gap of approximately 12µm is formed without the need for additional spacing elements. Deflection of the membrane, i.e. wavelength tuning, can be achieved by electro-thermal heating of the thin suspension beams by injecting a small current using the via-hole contacts through the substrate (see Fig. 1).

Without an antireflection coating (AR) at the semiconductor-air interface, the device consists of two coupled cavities which gives rise to a non-linear tuning behavior and to a

[1]phone: +49-89-289-12786, fax: +49-89-3206620, email: maute@wsi.tum.de
[2]Institute of Microwave Engineering, Darmstadt University of Technology, 64283 Darmstadt

limited tuning range. Previously, we reported a maximum tuning range of 43nm for this layout (see anual report 2004).

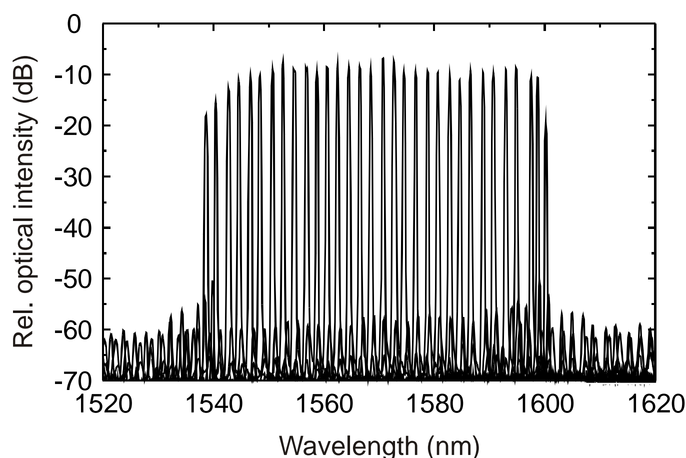

Fig. 2:
Laser spectra of widely tunable VCSEL with D=14µm.

By the use of an AR coating based on aluminum oxide which reduces the partial reflectivity at the transition from the semiconductor part to the air gap from about 32% to 2%, we were able to extend the tuning range to more than 60nm. Typical laser spectra for this kind of device are shown in Fig. 2. As can be deduced, the side mode suppression ratio regarding transverse and longitudinal modes is very constant and between 40 and 50dB even for a relatively large BTJ diameter *D* of 14µm. The fiber coupled power was between 0.1 and 0.5mW and the threshold current density reached a minimum value of $2kA/cm^2$ at a wavelength of 1560nm.

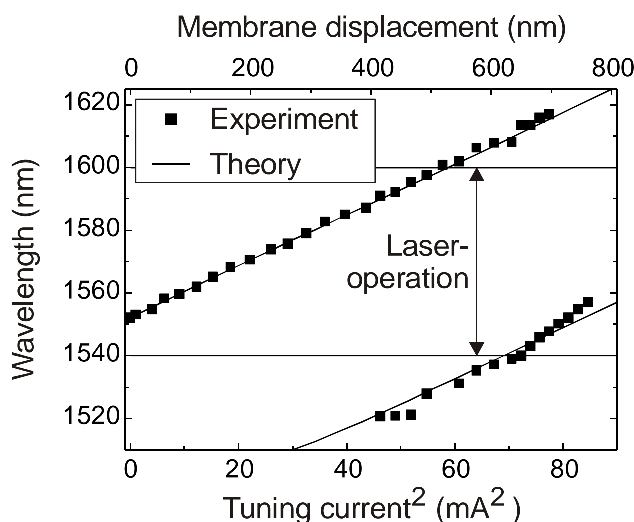

Fig. 3:
Tuning behavior of MEMS-VCSEL with AR coating.

Due to the decoupling, any non-linearity in the tuning behavior is suppressed, the wavelength shift is proportional to the dissipated tuning power, i.e. to the square of the tuning current and the experimental data can well be reproduced by theoretical calculations based on one dimensional transfer matrix calculations (see Fig. 3). These results represent the best laser performance obtained for this kind of devices so far and are directly related to the described advantages of the used two-chip-concept.

---

supported by BMBF (contract No. 01BP270)

1.55 µm Vertical-Cavity Laser Diodes at 10 Gb/s

W. Hofmann[1], M. Ortsiefer, and M. C. Amann

The vertical cavity surface emitting lasers (VCSELs) developed by us are generally well suited as transmitters in optical communication networks. Firstly, these lasers based on InP substrate show best performance at the telecommunication-wavelength of 1.55 µm. Secondly, the buried tunnel junction features low resistance n-type material resulting impedance around 50 Ω. Therefore this VCSEL can be driven without additional impedance-matching circuits. Furthermore the required operation voltage is only around 1 V, making this device compatible with nowadays CMOS technology. Last but not least, these lasers excel in their cost-structure. On the one hand the laser itself is less costly due to on-wafer testability; on the other hand the VCSEL also saves on system-level with its electrical compatibility and low power consumption. Several bandwidth-limiting effects have to be overcome to present a suitable light source for high-bit-rate data communications.

The VCSEL shown in Fig. 1 features an experimentally found effective reduction in capacitance from 1.8 pF to 1.0 pF by replacing the outer parts of the diode by an insulation layer of 10 µm BCB (Cyclotene 3022-57). Dry-etch BCB was chosen, because it combines a low dielectric constant around 2.5 up to 20 GHz with superior planarisation capabilities. Additionally, the required large film thickness can be achieved. The chip has two coplanar contact pads in order to enable the direct connection of the laser to a network analyzer using RF-probes. Therefore, measurements can be done without additional bonding wire inductance. This new design enables the investigation of the high-speed characteristics of our lasers.

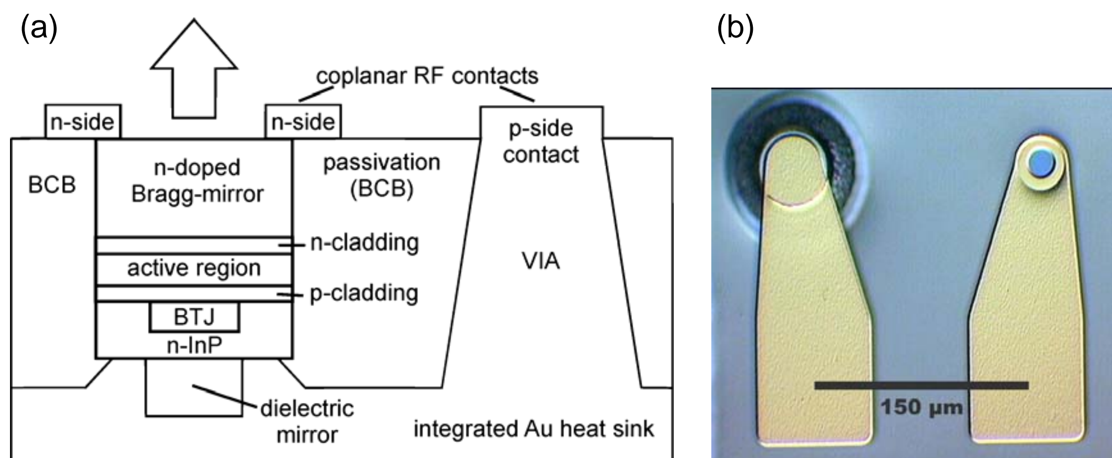

Fig. 1: *(a) Schematic diagram of BCB passivated BTJ-VCSEL. Coplanar contact pads enable the direct connection of the laser to a network analyzer using RF-probes.*
(b) Top view of the VCSEL-chip. Coplanar Contacts with 150 µm pitch to match GS 150 RF-microprobes.

[1]phone: +49-89-289-12786, fax: +49-3206620, email: hofmann@wsi.tum.de

The small-signal analysis of the rate equations above threshold yields a two-parameter modulation transfer function characterized by the relaxation resonance frequency f_R and the damping factor γ. Where f_R scales with the square-root of the current above threshold, proportional to the D-factor. Above threshold the damping factor γ is proportional to the square of the resonance frequency with damping offset γ_0 and the K-factor K, both used as fitting parameters to be extracted from S_{21} measurements.

In practice, the modulation response $H(f)$ of long-wavelength VCSELs is usually determined also by external parasitics e.g. contact pad capacitances so that a three-pole filter characteristic is more appropriate with f_{par} as cut-off frequency of the low-pass filter characterizing the parasitics. With higher bias currents, f_R rises and at the same time the response flattens due to increased damping limiting the maximum modulation bandwidth to $f_{3dB,\ damping}$. Near the thermal roll-over of the VCSEL, the resonance frequency saturates at a certain level also limiting the bandwidth to $f_{R3dB,\ thermal}$. Finally, assuming no thermal limitation and negligible damping, the modulation bandwidth is limited by parasitics.

From small-signal modulation experiments (S_{21}) which are presented in Fig. 2 we have deduced a D-factor of 5.8 GHz/(mA)$^{1/2}$ and 3dB cut-off frequencies up to around 8.9 GHz for 6 mA bias current.

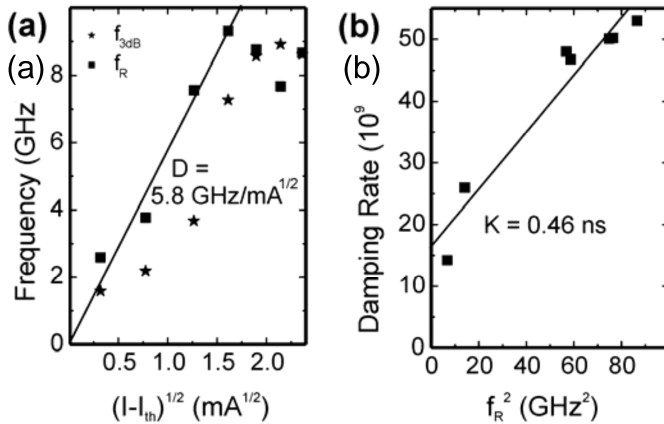

Fig. 2: *(a) 3dB and extrapolated resonance frequency versus square root of the driving current above threshold. A D-factor of 5.8 GHz/mA1/2 is demonstrated.*
(b) Damping rate γ above the square of relaxation resonance frequency revealing a K-factor of 0.46 ns.

Plotting the damping rate γ versus f_R^2 reveals a K-factor of 0.46 ns. Therefore, the intrinsic bandwidth $f_{3dB,\ damping}$ can be calculated to be 19.3 GHz including carrier transport effects and gain compression, neglecting heating effects and external parasitics. Around the thermal roll-over of the VCSEL the relaxation resonance frequency f_R saturates at around 9 GHz which leads to a thermally limited bandwidth $f_{R3dB,\ thermal}$ of 14 GHz. The parasitic pole f_{par} around 8 GHz yields a parasitic limitation $f_{3dB,\ parasitics}$ of 11.4 GHz (neglecting damping and assuming $f_R / f_{par} = 9/8$).

Therefore the modulation response of the investigated device is limited by parasitics, damping and thermal effects. External parasitics are significantly reduced by the BCB-passivated high-speed design which is very important due to high damping and the thermal limitation of f_R.

We acknowledge Prof. Ninghua Zhu from the National Research Center for Optoelectronic Technology, Beijing, for his support in RF-characterization of our VCSELs.

State-of-the-art widely tunable laser diodes with distributed feedback

René Todt[1], Thomas Jacke, Ralf Meyer, and Markus-Christian Amann

Widely tunable laser diodes with tuning ranges of several tens of nanometers are key components for fiber-optical communication system as well as for various sensing applications.

Even though such devices have been extensively investigated in recent years, presently available monolithic widely tunable lasers suffer from complex tuning schemes, requiring *three or even more tuning currents* to set the emission wavelength. Accordingly, device characterization and control is complicated, time-consuming and, hence, expensive.

A significant improvement on this issue has been achieved by our group with the realization of thermally as well as electronically widely tunable lasers that employ distributed feedback (DFB) to achieve a high spectral purity. While offering highly competitive performance characteristics, these lasers require *only two tuning currents* to set the emission wavelength, which eases the device control significantly.

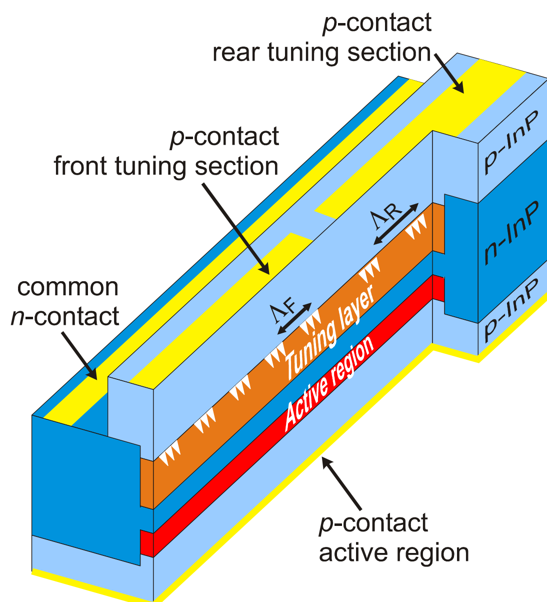

Fig. 1:
Schematic drawing of an electronically widely tunable twin-guide laser diode with sampled gratings.

A schematic drawing of such a device is shown in Fig. 1. From an optical point of view, the sampled grating (SG) tunable twin-guide (TTG) laser forms a single-mode waveguide that contains two layers (hence the name twin-guide): the active region and the tuning layer. The later one is longitudinally split into two sections that contain sampled gratings. The reflection spectrum of each SG can be shifted (independently from the other SG) by several nanometers by varying the carrier density inside corresponding tuning section.
Wide quasi-continuous wavelength-tuning is accomplished by utilizing the Vernier-effect. Continuous wavelength-tuning is obtained by tuning both reflectors simultaneously, whereas large wavelength jumps, so-called supermode hops, are obtained by tuning one reflector while leaving the other one unchanged.

[1]phone: +49-89-289-12767, fax: +49-89-3206620, email: todt@wsi.tum.de

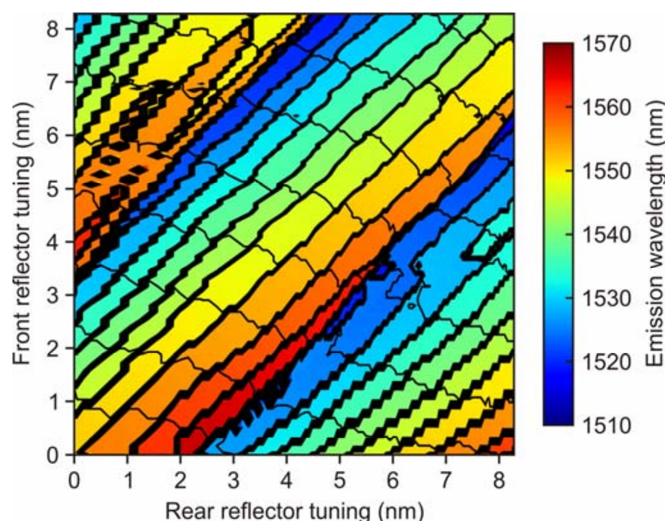

Fig. 2:
Wavelength map of a SG-TTG laser diode, illustrating the absolutely regular tuning behavior of the device.

The emission wavelength of a SG-TTG laser as a function of the two tuning currents is shown in the wavelength map in Fig. 2. One can easily recognize the absolutely regular tuning behavior. The wavelength map reveals also the location of the various supermodes, which are enclosed by thick solid lines. Within these supermodes, the emission wavelength can be continuously and mode-hop-free tuned by up to 8.2nm. Only minor variations in the side-mode suppression ratio (SMSR) are observed during the continuous tuning.

The tuning performance is of the SG-TTG laser is summarized in Fig. 3. Generally, the device provides excellent spectral purity, characterized by a SMSR in excess of 35dB, as well as high output powers above 10mW over a wavelength range of more than 40nm.

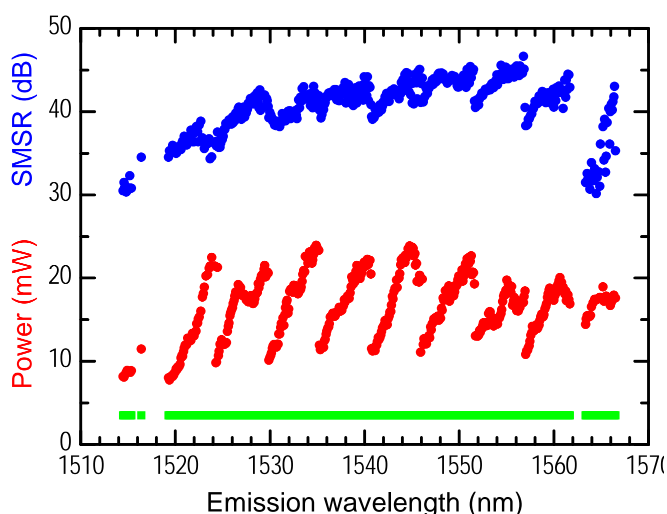

Fig. 3:
Output power and SMSR of a SG-TTG laser diode versus emission wavelength.
The green line at the bottom of the graph is shown as a visual guide to easily locate gaps within the tuning range.

In summary, the performance of the fabricated DFB-like widely tunable laser diodes compares well to that of other state-of-the-art monolithic widely tunable laser diodes. The large continuous tuning range of the SG-TTG laser as well as its simple wavelength tuning scheme, which requires only two tuning currents, are unmatched hitherto.

---

supported by the European Union via the IST-project IST-2000-28244 "NEWTON"

Widely tunable Mach-Zehnder interferometer lasers

Thomas Jacke[1], René Todt, Ralf Meyer, and Markus-Christian Amann

Widely tunable semiconductor lasers are deployed as versatile optical sources in fiber-based communication architectures. The lasers presented here use a vertically integrated Mach-Zehnder interferometer (VMZ) to control the laser wavelength. The advantage of the VMZ-concept is its simplicity and compactness: the wavelength is controlled by one current only and the discrete output spectrum exhibits an apropriate mode spacing for DWDM applications. Device dimensions and required fabrication technology are similar to that of conventional DFB-lasers.

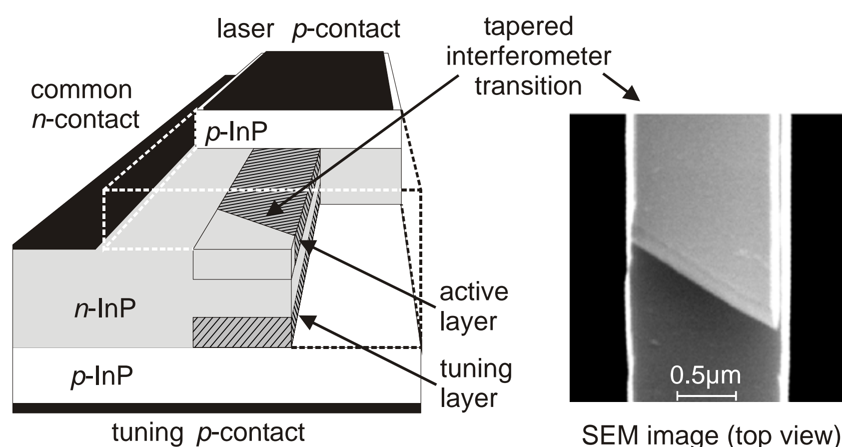

Fig. 1: *VMZ laser with tapered waveguide transitions*

The wavelength selection of the filter is accomplished by interference at the transition between interferometer section (two supported modes) and single-waveguide sections (one supported mode). At certain wavelengths, constructive interference leads to high filter transmission allowing laser emission to take place. By injection of carriers into the tuning layer the transmission maxima can be changed (plasma effect) and, thereby, the laser wavelength can be shifted.

Recently, electrical and optical design improvements have been conceived to prevent leakage currents and internal backward reflections. Internal reflections are critical to all forward coupling lasers as they heavily impair the tuning performance: typically, only a fraction of the available longitudinal modes could be accessed so far. The fabricated lasers now show the desired regular tuning characteristics and follow precisely the theoretical predictions. For the first time full mode accessibility has been achieved over the entire tuning range.

The output power characteristic of two different VMZ designs is presented in figure 2. The active region of one laser is composed of a multiple quantum well (MQW) structure, the other laser's active region is built of bulk material. The cavity length of both lasers is 750 µm, the waveguide width is 1.3 µm.

[1]phone: +49-89-289-12785, fax: +49-89-3206620, email: jacke@wsi.tum.de

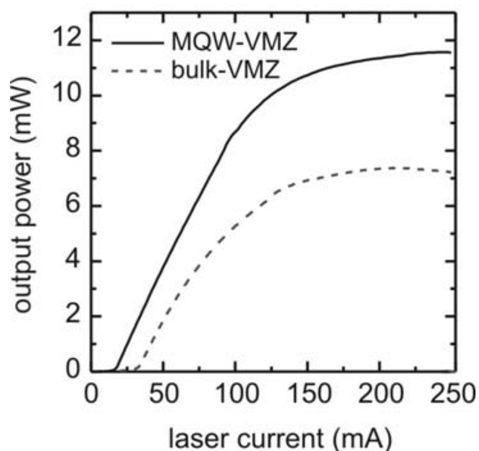

***Fig. 2:** LI-characteristic of VMZ lasers*

The power characteristic of both lasers is comparable to typical state-of-the-art Fabry-Pérot lasers. The threshold current of the bulk laser is 31 mA and a maximum power of 7.4 mW is reached. The corresponding figures of the MQW laser is 16 mA as threshold current and a maximum power of 11.5 mW.

In figure 3 the laser peak wavelength of a bulk-VMZ laser is plotted against the tuning current at a laser current of 25mA. The length of the cavity and the interferometer are 515µm and 465µm, respectively. Due to the optimized design, all 53 modes within the tuning range can be regularly addressed. At a tuning current of 3.5mA the free spectral range (FSR) of the VMZ limits the tuning range and causes a repeat mode hop followed by a second tuning branch with an equal wavelength pattern. The wavelength grid corresponds to a channel spacing of 73GHz. The strong filter shift of 10nm per mA tuning current reflects a “smooth filter design” with a small effective group index difference in the two interferometer arms.

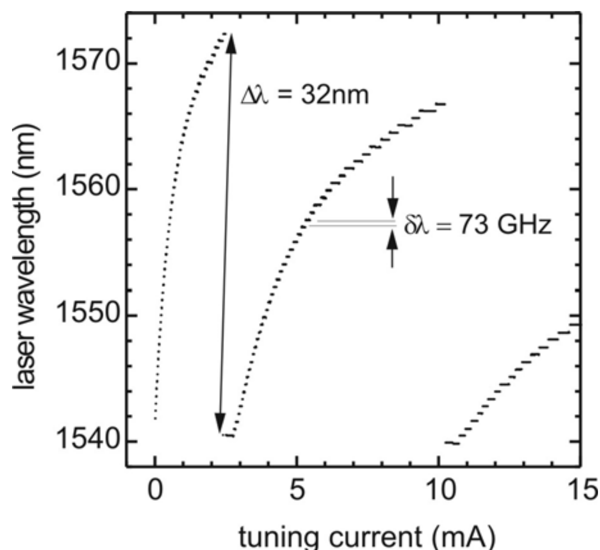

***Fig. 3:** Tuning characteristics of bulk-VMZ*

Subsequently, in the present design the devices only provide a modest level of side-mode suppression. This makes, on the other hand, the result of regular and complete longitudinal mode access still more valuable, since it has been achieved despite the poor spectral selectivity of the actual smooth filter design.

The longitudinal integration of a second interferometer in one laser cavity furthermore enlarges the possibilities of the VMZ design. Due to the additional VMZ filter the FSR is a multiple of the single-VMZ’s FSR. In this way a total tuning range of 67nm (127 wavelength channels) has been obtained with the bulk laser design. Double-VMZ lasers based on MQW-structures achieved an FSR of more than 80nm. According to the application needs this method can also be used to enlarge the filter selectivity (“strong filter design”) without the disadvantage of a reduced tuning range.

With the presented lasers the theoretically deduced device principles and the predicted tuning performance has been verified and important design parameters could be extracted from the measurements. Large tuning ranges (>80nm), high output powers (up to 10mW) and a single-current controlled regular tuning scheme (full mode accessibility) has been demonstrated. From the present results also other application-specific tuning characteristics can be straightforwardly designed and manufactured.

Low-threshold injectorless quantum-cascade lasers emitting at ~7.9 μm

Andrea Friedrich[1], Gerhard Boehm, and Markus-Christian Amann

Quantum-cascade (QC) lasers are capable light sources in the mid- and far-infrared spectral region with several potential applications, especially gas detection. Usually, QC lasers consist of a periodic repetition of active sections and so-called injector regions. These injector regions have been considered as an essential requirement for laser action in QC lasers. In the active sections the photons are generated, while the injector regions enable the transfer of the electrons from the lower states of one active section into the upper state of the next section. Furthermore, due to the doping of these regions, they act as an electron reservoir and provide stable current flow. Apart from these benefits, the main disadvantage of the injector regions is the lengthening of the active stage with optically passive and slightly absorbing material and therefore a reduced overlap of the waveguide mode with the active sections. QC lasers without injector regions are expected to yield improved performance, provided that the electron transfer can be managed otherwise.

Previously, we have realized injectorless QC lasers (λ~10 μm) operating above room temperature with comparable low threshold current densities, but shorter wavelengths remain a challenge in this design scheme.

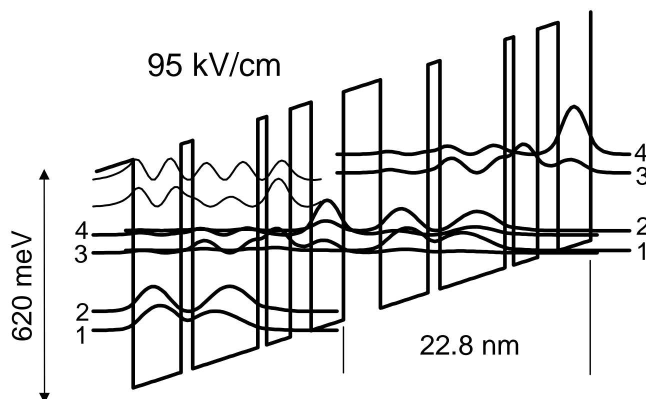

Fig.1: *Conduction-band profile and moduli squared of the wave functions. The layer sequence (in nm) of one period of the active region starting at the left-most barrier is:*

3.4/4.4*/1.1/6.0/0.8/2.2/1.9/****3.0****.* *Layers in bold face are Si-doped to* $n = 8\times10^{16}$ *cm*$^{-3}$.

Recently, we have demonstrated improved injectorless QC lasers, emitting at λ~7.9 μm. Fig. 1 shows the conduction-band structure of two successive active sections and the moduli squared of the wave functions for an applied bias field of 95 kV/cm. Here, levels 1 and 2 of one stage are resonant with levels 3 and 4 of the following stage. Therefore, the electrons are transferred directly from one active section into the next. The transition energy is calculated to E_{32}=159 meV (λ≈7.8 μm), the optical dipole matrix element is z_{32}=2 nm and the scattering times are τ_3=1.48 ps and τ_{21}=0.34 ps.

The whole structure, including a thick InP cladding layer, was grown by solid-source molecular beam epitaxy on a n-type InP substrate. The active region is realized in the material system $Ga_{0.4}In_{0.6}As/Al_{0.56}In_{0.44}As$ and contains 65 periods. The upper cladding consists of a 0.5 μm thick n-$Ga_{0.47}In_{0.53}As$ layer (Si, 6×10^{16} cm^{-3}), followed by a 2.3 μm thick n-InP (Si, 1×10^{17} cm^{-3}) and a 1 μm thick n+-$Ga_{0.47}In_{0.53}As$ (Si, 1×10^{19} cm^{-3}) cap layer. A

[1]phone: +49-89-289-12767, fax: +49-89-3206620, email: friedrich@wsi.tum.de

0.5 μm thick n-$Ga_{0.47}In_{0.53}As$ layer (Si, 6×10^{16} cm^{-3}) and the InP substrate serve as the lower cladding. The wafer was processed into ridge-waveguide lasers. A 400 nm thick SiO_2-layer was used as insulation. The top-contacts are made of Ti/Pt/Au and, after thinning, Ge/Au/Ni/Au bottom-contacts were evaporated. The devices were cleaved and mounted on copper heat sinks, the facets left uncoated.

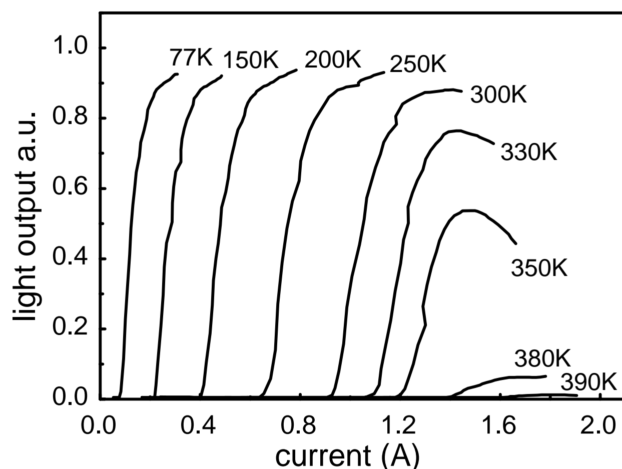

Fig.2:
Pulsed light output against current characteristics of a 3.2 mm long and 12 μm wide device at various heat sink temperatures.
Pulse width: 250 ns
Repetition rate: 250 Hz

All devices were contacted with wire bonding and placed in a cold finger cryostat, typically operated between 77 K and 500 K. The light is collected with an f /1 Au-coated parabolic mirror and detected with a liquid nitrogen-cooled HgCdTe detector. In Fig. 2 the pulsed light output-current characteristics of a representative device with 3.2 mm cavity length and 12 μm width is shown for various heat-sink temperatures. The maximum operating temperature is about 400 K. The values of the threshold current density are exceedingly low with 210 A/cm^2 at 77 K and 2.4 kA/cm^2 at 300 K.

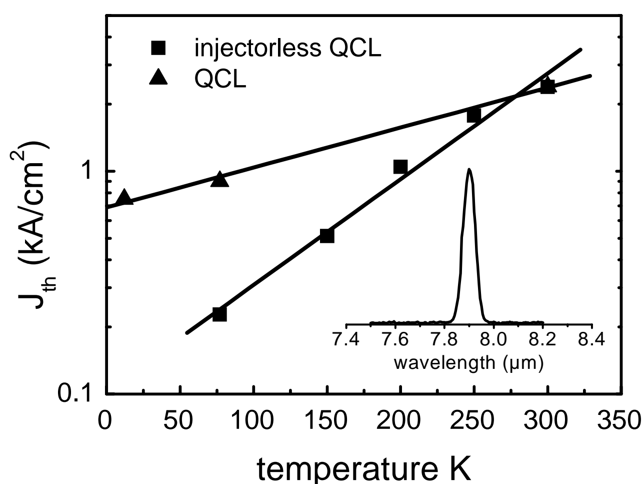

Fig.3:
Comparison of our injectorless QC laser with a usual QC laser (λ~7.9 μm):
Threshold current density against heat sink temperature of devices with ~2 mm length.

The inset shows the spectrum at 300 K.

In comparison with conventional QC lasers in this wavelength region, at 77 K the threshold current densities of our injectorless QC lasers are significantly smaller, while at room temperature the values are well comparable, as shown in Fig. 3. The inset of Fig. 3 contains the spectrum, measured with a grating spectrometer. At 300 K the laser wavelength is about 7.9 μm, which is in good agreement with our model calculations.

Progress towards an electrically driven single photon source based on two dimensional photonic crystal nanocavities

M. Kaniber[1], F. Hofbauer, A. Kress, S. Grimminger, M. Bichler, and J. J. Finley

One of the major requirements for building efficient systems for quantum cryptography and quantum computation processing based on linear optics, is the development of a device capable of efficiently generating single photons with a high degree of photon indistinguishability. One approach is to utilize the Purcell effect to efficiently funnel photons emitted from individual self-assembled InGaAs quantum dots (QDs) into a single optical mode of an optical nanocavity. The strong (~20x) enhancement of the radiative rate guarantees that emitted photons are Fourier limited.

Over the past year we have studied the influence of a tailored photonic environment on the strength of the light-matter coupling with individual QDs. Photonic nanostructures are realized by 2D photonic crystal (PC) nanostructures containing a dilute array of QDs. The radiative properties of isolated dots have then been investigated using time resolved and CW spectroscopy to probe the influence of the PC nanocavity and the 2D photonic bandgap.

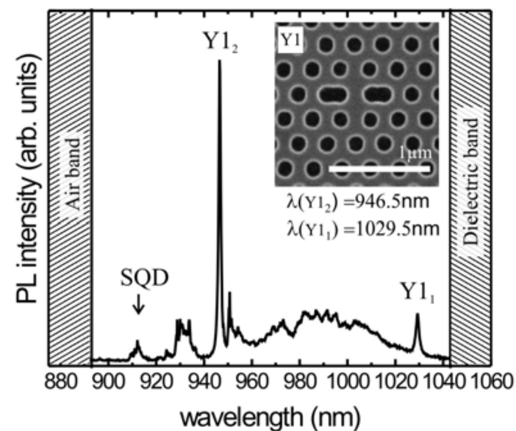

Fig. 1: *Typical PL-spectrum and SEM image (inset) of a 2D PC nanostructure.*

A SEM picture of such a PC containing a so-called Y1 defect nanocavity at its center is shown in the inset of figure 1. For such cavity designs we obtain very high mode quality factors in excess of ~10000. The main panel of figure 1 depicts a typical spatially resolved photoluminescence (PL) spectrum recorded from one of our photonic nanostructures. In addition to emission from several isolated QDs, two cavity resonances labeled as $Y1_1$ and $Y1_2$ are clearly observed, the frequency of which and dependence on structural parameters are found to be in very good agreement with 3D bandstructure calculations of theses cavities (not shown here).

We investigated in detail the lines marked with SQD in figure 1. A PL spectrum of these lines recorded with higher spectral resolution (Fig. 2 (a)) reveals two peaks, labeled as X and 2X. Power dependent CW measurements on these lines (Fig. 2 (b)) exhibit a clear linear and quadratic behaviour, characteristic of recombination from the exciton (X) and biexciton (2X) states of a single QD. In order to probe the temporal statistics of the emitted photons and study the photon extraction efficiency, we recorded photon correlation measurements using a Hanbury-Brown-Twiss photon correlation setup. From these measurements we could determine the second-order correlation function $g^{(2)}(\tau)$ (Fig. 2 (c)), where we obtain a clear dip at zero delay time ($g^{(2)}(0)=0.3$) and a very long correlation time $\tau_{cor}=8.1\pm0.8$ ns. The pronounced dip indicates that the measured light is predominantly emitted by a single quantum state from an anharmonic quantum emitter. Furthermore, we measured the spontaneous emission decay lifetimes for the X and 2X transitions using

[1]phone: +49-89-289-12784, fax: +49-89-3206620, email: kaniber@wsi.tum.de

time-correlated single photon counting (Fig 2d). The lifetimes thus measured (τ_X=13±1 ns and τ_{2X}=9.0±0.5 ns) are extremely long for self-assembled QDs, due to suppression of the radiative emission due to the 2D photonic bandgap. This suppression of emission in the plane of the 2D photonic crystal results in a spatial redistribution of the spontaneous emission and we estimate that ~30x more photons are emitted from the surface of the device when compared with similar material without the photonic bandgap. Until now single photon emission was not observed for dots on resonance with the cavity mode, a finding that may be due to the onset of low threshold lasing as has been recently reported.

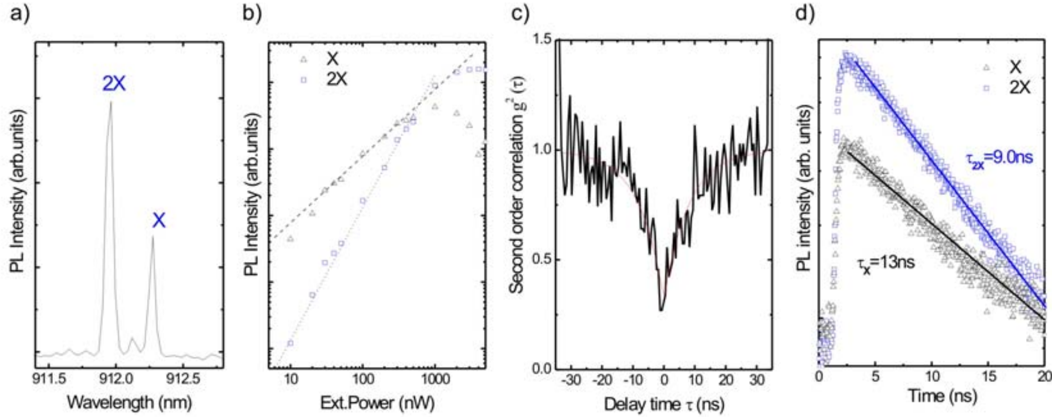

Fig. 2: *(a) PL spectrum of the lines marked with SQD above. (b) PL intensity as a function of excitation power. (c) Second order correlation function for the line labeled as 2X. (d) Time-resolved decay transients for the exciton and biexciton line.*

We are also investigating the potential to control the QD-cavity coupling using the quantum confined Stark effect. Membrane PC nanocavities were fabricated containing thin p-i-n diodes (Fig 3 inset). By reverse biasing the p-i-n junction electric fields up to F~200kV/cm can be applied parallel to the QD growth direction. Quenching of the QD PL is observed for F_c~40-50kV/cm, since electron tunneling escape from the QDs then occurs faster than the radiative lifetime (Fig 3). By measuring the field at which the PL quenches as a function of position on the PC we *electrically* probe the local density of photonic states. Furthermore, Stark shifts of the QD emission up to a few meV was already observed, demonstrating that the devices have strong potential to study cavity-QED phenomena using an electrically tunable system.

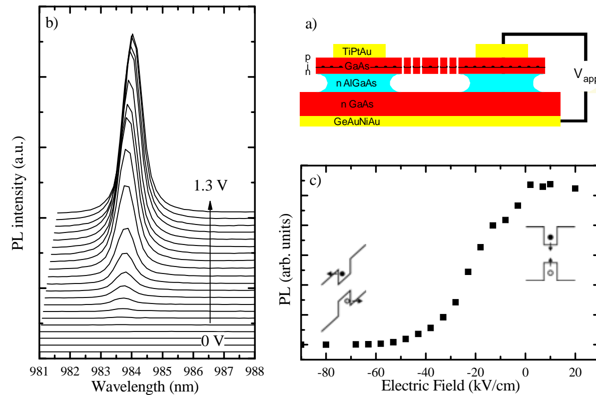

Fig. 3: *(a) Schematic of electrically active photonic crystal nanostructures (b) Field induced quenching of cavity mode (c) Intensity versus electric field.*

supported via Sonderforschungsbereich 631 - B3

3. Research Funding and Collaborations

Many of our research projects have benefited from very fruitful collaborations with external groups either via joint projects, individual collaborations, exchange programs, or through direct interaction with visitors. The major external collaborations are based on joint projects which are financially supported by different organizations.

Funded Projects

1. Bundesministerium für Bildung und Forschung (BMBF)

- Kompetenzzentrum Nanop: „Anwendung von Nanostrukturen in der Optoelektronik“
- Förderschwerpunkt MultiTeraNet: “Mikromechanisch abstimmbare VCSEL für den Wellenlängenbereich 1,5 µm“
- Förderschwerpunkt neue Materialien: “Materialien für Infrarotkonverter“
- „Halbleiter-Nanostrukturen für molekulare Bioelektronik“
- „EXIST-SEED; nextnano^3 – Entwicklung von Simulationssoftware“
- nanoQuit: „Gekoppelte Quantenpunkttransistoren in präziser Kettenanordnung“,
  „AlAs Nanostrukturen als quantengekoppelte Systeme“,
  „Entwicklung von quantenpunktbasierenden Einzelphotonenquellen für Emissionswellenlängen um 1,55 µm“

Bundesministerium für Umwelt, Naturschutz und Reaktorsicherheit (BMU)

- Kristalline Silizium-Legierungen für Dünnschicht-Solarzellen

2. Deutsche Forschungsgemeinschaft (DFG)

- Sonderforschungsbereich „Bioorganische Funktionssysteme auf Festkörpern“ (SFB 563)
- Sonderforschungsbereich „Festkörperbasierte Quanteninformationsverarbeitung“ (SFB 631)
- Schwerpunktprogramm „Quanten-Hall-Systeme“
- Schwerpunktprogramm „Optische Übermittlungsverfahren in der Informationstechnik“
- Forschungskooperation „FORMEDIAN“
- Am 101/7-1: „High-speed vertical-cavity laser-diodes at 1,55 µm“
- Ei 518/1-1+2: „Heteroepitaxie von Gruppe III-Nitriden auf Diamantsubstraten für optoelektronische und elektronische Anwendungen“

3. Bayerische Forschungsstiftung

- Langfristprogramm Neue Werkstoffe

4. Bayerisch-Französisches Hochschulzentrum / BFHZ-CCUFB

- „UV electroluminescent diodes based on AlN/diamond heterojunctions. From materials to devices”

5. Bayerisch-Kalifornisches Hochschulzentrem - BaCaTeC

- ”New Materials for Spintronics“
- “High-speed Data-Com-Lasers (VCSELs) for injection locking experiments”

6. DAAD

- Acciones Integradas Hispano-Alemanas – PPP mit Spanien
- PROCOPE – PPP mit Frankreich
- Projektbezogener Personenaustausch mit der VR China”

7. Elitenetzwerk Bayern

Int. Graduate School “Materials Science of Complex Interfaces (CompInt)”

8. European Union

- COLLECT (Collective electronic states in nanostructures)
- DRIVE (Diamond Research on Interfaces for Versatile Electronics)
- GANANO(New Generation of GaN-based sensor arrays for nano- and pico-fluidic systems for fast and reliable biomedical testing)
- NEWTON (New Widely Tunable Lasers for Optical Networks)
- PSY-NANO-Si: Nanosilicon-based photosynthesis for chemical and biomedical applications

9. Industry

- Degussa AG Düsseldorf, Germany:
  „Funktionsschichten aus Silizium-Nanopartikeln“
  „Silizium-Nanopartikel für Hybride Solarzellen“
  „Lumineszierende Silizium Nanopartikel für smart label Anwendungen“
- EADS Deutschland GmbH, München, Germany:
  „NANOS4 (Nano-structured solid-state gas sensors with superior performance)”
- Fujitsu Laboratories of Europe Ltd., Hayes Park, UK: “Bio-Nanotechnology”
- ρ-BeSt, Innsbruck, Austria: “Nano Diamond Network”
- Mettler-Toledo, Urdorf, Switzerland: “AlGaN/GaN pH-Sensor Entwicklung”
- Rhode & Schwarz, München, Germany: „Zero-Bias Schottky-Diodes“
- Siemens University Embrionic Program (UEP), Erlangen, Germany:
  „Integrierte Gassensoren und UV-Detektoren zur drahtlosen Überwachung von Verbrennungsprozessen“
- Vertilas, Garching, Germany: „Langwellige VCSEL“

9. FWF - Fonds zur Förderung der wissenschaftlichen Forschung, Wien, Austria

„SFB F025: InfraRed optical nanostructures“

Other collaborations and project partners:

RWTH Aachen, Arizona State University, University of California at Berkeley, TU Braunschweig, Universität Bremen, Wacker Siltronic Burghausen, MIT Cambridge, TU Darmstadt, TU Delft, Intune Dublin, Universität Duisburg, Universität Erlangen-Nürnberg, FHG IPM Freiburg, General Electric Garching, Vertilas Garching, Walther Meißner Institut Garching, Gayton Photonics (UK), IMEC Gent, Universität Gießen, Universität Graz, Universität Hamburg, Universität Hannover, Foundation for Research and Technology-Hellas (FORTH) Heraklion, University of Crete Heraklion, City University of HongKong, TU Ilmenau, FZ Jülich, Institute of Nuclear Physics Krakow, Universität Leoben, Interuniversitair Micro-Electronica Centrum Leuven, Linköping University, Universität Linz, King's College London, Universidad Politecnica de Madrid, Universität Marburg, Fraunhofer Institut IZM München, Infineon München, LMU München, Siemens München, General Electric Finance Holding GmbH Neu-Isenburg, EADS Deutschland Ottobrunn, Universität Paderborn, Centre National de la Recherche Scientifique Paris, SNS Pisa, Institute of Physics Prague, Universität Regensburg, Weizmann Institute Rehovot, Università Rom II Tor Vergata, UCSB Santa Barbara, ρ-BeSt coating Hartstoff-beschichtungs GmbH Steinach, MPI FKF Stuttgart, Universität Stuttgart, University of Tokyo, Rensselaer Polytechnic Institute Troy, Diamond Research Center Tsukuba, National Institute of Materials Science Tsukuba, Universität Ulm, High Pressure Research Centre (Unipress) Warsaw, TopGaN Ltd. Warsaw, University of Warwick, TU Wien, Nanoplus Würzburg, Universität Würzburg, Bookham Zürich, ETH Zürich.

4. Members of the Institute, Postdocs, and Guest Scientists

Faculty Members and Scientific Staff

Gerhard Abstreiter
Markus-Christian Amann
Gerhard Böhm
Martin S. Brandt
Dominique Bougeard
Manfred Claassen
Martin Eickhoff
Jonathan Finley
Anna Fontcuberta i Morral
Jürgen Freyer
José Antonio Garrido Ariza
Matthew Grayson
Ralf Meyer
Ulrich Rant
Dieter Schuh
Martin Stutzmann
Mark Tornow
Alexandros Trellakis
Peter Vogl

Administrative and Technical Staff

Wolfgang Bendak
Max Bichler
Veronika Enter
Michael Fischer
Alicia Fraile
Joseph Grottenthaler
Rosemarie Heilmann
Daniela Huber
Bernhard Kratzer
Liane Lindner
Sonja Matich
Linda Mora
Irmgard Neuner
Claudia Paulus
Hubert Riedl
Edith Sckopke
Friedrich Sedlmeir
Angelika Stumpf
Ralf Wasserrab
Adolf Ziegltrum

Doctorate Candidates (thesis completed*)

Stefan Ahlers
Till Andlauer
Silvia Baldovino
Jochen Bauer*
Andrea Baumer*
Barbara Baur
Christoph Bihler
Stefan Birner
Ingo Bormann*
Dominique Bougeard*
Karin Buchholz*
Emily Clark
Susanne Dachs
Shivaji Dasgupta
Oliver Dier
Frank Ertl
Frank Fischer*
Andrea Friedrich
Florian Furtmayr
Wojciech Gajewski
Mario Gjukic
Markus Grau*
Andreas Härtl
Dominik Heiss
Martin Hermann
Felix Hofbauer
Werner Hofmann
Michael Huber
Hans Hübl
Nebile Isik
Thomas Jacke
Michael Kaniber
Fabian Köhler
Hubert Krenner

Andreas Kreß*
Miroslav Kroutvar
Tillmann Kubis
Christian Lauer
Robert Lechner
Sebastian Luber
Simon Lud
Markus Maute
Ulrich Rant*
Sebastian Roth
Michael Scholz
Robert Shau*
Johanna Simon
Georg Steinhoff
Lucia Steinke
Sebastian Strobel
René Todt
Emanuele Uccelli
Thomas Wassner
Olaf Weidemann
Tobias Zibold

Diploma Students (theses completed*)

Philipp Achatz*
Christian Ammann*
Tobias Antesberger
Alexander Bachmann
Dominic Dorfner
Roland Enzmann
Sebastian Gatz
Yvonne Gawlina
Simon Grimminger
Benno Grolik
Christine Hautmann
Dominik Heiss*
Rolf Helmes
Marco Höb*
Andreas Huber*
Christian Jäger
Michael Kaniber*
Claudius Knaak
Michael Kraus
Bernhard Laumer
Simone Lingitz
Markus Maier*
Franz Mayer
Richard Morschl
Marco Neumair
Christian Nömeier*
Stefan Nowy*
Carola Oberhüttinger
Daniel Pedone
Andreas Popp
Norbert Reinelt*
Jürgen Sailer
Stefan Schäck
Simon Scherer
Albert Schließer*
Bernhard Schmid
André Stegner*
Hans-Georg von Ribbeck*
Andreas Wieczorek*
Ying Xiang

Master Students

Emily Clark*
Nuryanti*
Tahmineh Pourrastami*
Mohamed Rahim*
Alexander Solovev*
Xie Yi
Fan Zhang*

Postdocs

Anna Cattani-Scholz
Jorge Hernando Garcia
Allan Hansen
Svetoslav Koynov
Joel Moser (until 09/2005)
Erika Pringsheim

Guest Scientists:
Kenji Arinaga, Fujitsu Laboratories LTD, Kanagawa, Japan
Jorge Hernando Garcia, Universidad Autónoma, Madrid, Spain
Wayne Hutchison, ARC Centre of Excellence for Quantum Computer Technology University of New South Wales, Canberra, Australia
Gabri Lansbergen, Kavli Institute of Nanoscience, Delft University of Technology, The Netherlands
Dane McCamey, ARC Centre of Excellence for Quantum Computer Technology, University of New South Wales, Sydney, Australia
Toshihiro Nakaoka, University Tokyo, Japan
Hermann Sellier, Kavli Institute of Nanoscience, Delft University of Technology, The Netherlands
Michael Shur, Electrical, Computer and Systems Engineering Rensselaer Polytechnic Institute, Troy, NY, USA (Senior Humboldt Fellow)
Kent Smith, Purdue University, USA
Gangyi Xu, Shanghai Institute of Microsystem and Information Technology, China

5. Doctoral, Diploma, Bachelor, and Master Theses

Doctoral Theses

1. *Growth and electronic properties of two-dimensional systems on (110) oriented GaAs*
   Frank Fischer (15.6.2005)

2. *Electrical manipulation of DNA on gold surfaces*
   Ulrich Rant (22.8.2005)

3. *Molekularstrahlepitaktische Herstellung von antimonidischen Laserdioden für die Gassensorik*
   Markus Grau (25.8.2005)

4. *Intersubband Spektroskopie an Silizium-Germanium Quantenkaskadenstrukturen*
   Ingo Bormann (5.9.2005)

5. *Langwellige oberflächenemittierende Laserdioden mit hoher Ausgangsleistung und Modulationsbandbreite*
   Robert Shau (7.9.2005)

6. *Spektroskopische Charakterisierung von Germanium-Quantenpunkten in Silizium*
   Dominique Bougeard (16.9.2005)

7. *Manipulation of the ligth-matter-interaction in photonic crystal nanocavities*
   Andreas Florian Kreß (27.10.2005)

8. *Structural and electronic properties of hydrosilylated silicon surfaces*
   Andrea Baumer (28.10.2005)

9. *Microprocessing of silicon on insulator substrates and biofunctionalisation of silicon dioxide surfaces for sensing applications in fluids*
   Karin Buchholz (6.12.2005)

10. *Untersuchungen zum kontrollierten Wachstum von InAs-Nanostrukturen auf Spaltflächen*
    Jochen Bauer (21.12.2005)

Diploma Theses

1. *Optically induced electron spin storage in quantum dots*
   Dominik Heiss (3/2005)

2. *Optical investigations of photonic crystal nanocavities for solid state quantum optics*
Norbert Reinelt (4/2005)

3. *Structural, optical and electronic properties of nanocrystalline diamond thin films*
Philipp Achatz (5/2005)

4. *Abbildung der strukturellen Eigenschaften von SiC mittels IR-Nahfeldmikroskopie*
Andreas Huber (7/2005)

5. *Electron spin resonance of self assembled quantum dots*
Christian Nömeier (7/2005)

6. *Kohärente Infrarotspektroskopie und -mikroskopie*
Albert Schließer (7/2005)

7. *Electrical and optical characterization of diamond AlGaN interfaces*
Markus Maier (9/2005)

8. *Herstellung und Charakterisierung von Quantenkaskadenlasern*
Andreas Wieczorek (10/2005)

9. *Magneto-optical properties of semiconductors in ultrahigh magnetic fields*
Christian Oliver Moritz Ammann (11/2005)

10. *Manipulation von DNA durch elektrische Felder*
Marco Andreas Höb (11/2005)

11. *Manipulation of quantum dot spontaneous emission in GaAs photonic crystal nanostructures*
Michael Kaniber (11/2005)

12. *Spin properties of phosphorus donors in silicon epilayers*
André Stegner (11/2005)

13. *Wasserstoff im ferromagnetischen Halbleiter GaMnAs*
Christoph Bihler (12/2005)

14. *Diamond based ion sensitive field effect transistors*
Stefan Nowy (12/2005)

15. *Elektrochemische Charakterisierung von biofunktionalisierten Gallium-Nitrid-Oberflächen*
Hans-Georg von Ribbeck (12/2005)

Bachelor Theses

1. *Characterization of photonic crystal nanostructures for molecular cryptography*
   Markus Hallermann (8/2005)

2. *Controlled self-assembly of DNA layers on gold surfaces*
   Jelena Knezevic (8/2005)

Master Theses

1. *Electric field controlled tunnel coupling in individual quantum dot molecules*
   Emily Clark (8/2005)

2. *Diamond surfaces for affinity biosensors*
   Tahmineh Pourrostami (9/2005)

3. *Nanometer spaced electrodes for molecular electronics applications*
   Fan Zhang (11/2005)

4. *Electrical transport of ALILE crystallized nanocrystalline silicon*
   Nuryanti (12/2005)

5. *Functionalized silicon-on-insulator thin film resistors for biosensing applications*
   Alexander Solovev (12/2005)

6. Publications

Magnetotransport spectroscopy of mode coupling in electron wave guides
G. Apetrii, S. F. Fischer, U. Kunze, D. Schuh, and G. Abstreiter
in: Proc. of the 27th International Conference on the Physics of Semiconductors, Eds: J. Menéndez and C. G. Van de Walle, AIP Conference Proc. **772** (2005), p. 923-924

Chemical functionalization of GaN and AlNsurfaces
B. Baur, G. Steinhoff, J. Hernando, O. Purrucker, M. Tanaka, B. Nickel, M. Stutzmann, and M. Eickhoff
Appl. Phys. Lett. **87**, 263901 (2005)

Theoretical study of electrolyte gate AlGaN/GaN field effect transistors
M. Bayer, C. Uhl, and P. Vogl
J. Appl. Phys. **97** (3), 033703 (2005)

BioMOCA - a Boltzmann transport Monte Carlo model for ion channel simulation
T. A. van der Straaten, G. Kathawala, A. Trellakis, R. S. Eisenberg, and U. Ravaioli
Molecular Simulation **31** (2-3), 151-171 (2005)

Modeling of purely strain-induced CEO GaAs/$In_{0.16}Al_{0.84}As$ quantum wires
S. Birner, R. Schuster, M. Povolotskyi, and P. Vogl
in: Proc. of the 5th Int. Conf. Numerical Simulation of Optoelectronic Devices (NUSOD'05), Berlin, Germany, 1 (2005)

Diffusion of dopants in highly (1e20/cm3) n- and p-doped GaSb-based materials
O. Dier, M. Grau, C. Lauer, C. Lin, and M.-C. Amann
J. Vac. Sci. Technol. B **23**, No. 2, 349-353 (2005)

Negative differential conductance in cleaved edge overgrown surface superlattices
T. Feil, H.-P. Tranitz, M. Reinwald, W. Wegscheider, M. Bichler, D. Schuh, G. Abstreiter, and S. J. Allen
in: Proc. of the 27th International Conference on the Physics of Semiconductors, Eds: J. Menéndez and Chris G. Van de Walle, AIP Conference Proc. **772** (2005), p. 900-901

Modulating the growth conditions: Si as an acceptor in (110) GaAs for high mobility p-type heterostructures
F. Fischer, D. Schuh, M. Bichler, G. Abstreiter, M. Grayson, and K. Neumaier
Appl. Phys. Lett. **86**, 192106 (2005)

Physics and growth of Si-doped two-dimensional high mobility hole gases on (110) oriented GaAs
F. Fischer, M. Grayson, D. Schuh, M. Bichler, and G. Abstreiter
in: Proc. of the 27th International Conference on the Physics of Semiconductors, eds: J. Menéndez and C. G. Van de Walle, AIP Conference Proc. **772** (2005), p. 443-444

Influence of voltmeter input impedance on quantum Hall measurements
F. Fischer and M. Grayson
J. Appl. Phys. **98**, 013710 (2005)

Magnetotransport spectroscopy of spatially coincident coupled electron waveguides
S. F. Fischer, G. Apetrii, U. Kunze, D. Schuh, and G. Abstreiter
Phys. Rev. B **71**, 195330 (2005)

Injectorless quantum-cascade lasers
A. Friedrich, G. Scarpa, G. Böhm, and M.-C. Amann
in: Semiconductor and Integrated Opto-Electronics Conference (SIOE), Cardiff, UK (2005)

Quantum-cascade lasers without injector regions operating above room temperature
A. Friedrich, G. Scarpa, G. Böhm, and M.-C. Amann
Appl. Phys. Lett. **86**, 161114 (2005)

High performance injectorless quantum-cascade lasers
A. Friedrich, G. Scarpa, G. Böhm, and M.-C. Amann
Electron. Lett. **41**, No. 9, 529-531 (2005)

Above room temperature operation of injectorless quantum cascade lasers
A. Friedrich, G. Scarpa, G. Böhm, and M.-C. Amann
in: Proc. of the 17th International Conference on Indium Phosphide and Related Materials (IPRM), Glasgow, Scotland, UK (2005)

Low-threshold injectorless quantum cascade lasers emitting at l ~ 7.9 mm
A. Friedrich, G. Böhm, and M.-C. Amann
in: 8th International Conference on Intersubband Transitions in Quantum Wells (ITQW), Falmouth, Cape Cod, USA (2005)

Bound-to-bound and bound-to-free transitions in surface photovoltage spectra: Determination of the band offsets for $In_xGa_{1-x}As$ and $In_xGa_{1-x}As_{1-y}N_y$ quantum wells
M. Galluppi, L. Geelhaar, H. Riechert, M. Hetterich, A. Grau, S. Birner, and W. Stolz
Phys. Rev. B **72**, 155324 (2005)

ph sensors based on hydrogenated diamond surfaces
J. A. Garrido, A. Härtl, S. Kuch, M. Stutzmann, O. A. Williams, and R. B. Jackson
Appl. Phys. Lett. **86**, 073504-1-3 (2005)

Temperature dependence transport properties of hydrogen-induced diamond surface conductive channels
J.A. Garrido, T. Heimbeck, and M. Stutzmann
Phys. Rev. B **71**, 245310 (2005)

Optical and electrical properties of polycrystalline silicon-germanium thin films prepared by aluminium-induced layer exchange
M. Gjukic, R. Lechner, M. Buschbeck, and M. Stutzmann
Appl. Phys. Lett. **86**, (2005) 062115-1-3

Room-temperature operation of 3.26µm GaSb-based type-I lasers with quinternary *AlGaInAsSb barriers*
M. Grau, C. Lin, O. Dier, C. Lauer, and M.-C. Amann
Appl. Phys. Lett. **84**, 241104 (2005)

Four-point measurements of n- and p-type two-dimensional systems fabricated with cleaved-edge overgrowth
M. Grayson, S. F. Roth, Y. Xiang, F. Fischer, D. Schuh, and M. Bichler
Appl. Phys. Lett. **87**, 212113 (2005)

Corner overgrowth: Bending a high mobility two-dimensional electron system by 90°
M. Grayson, D. Schuh, M. Huber, M. Bichler, and G. Abstreiter
Appl. Phys. Lett. **86**, 032101 (2005)

Measuring carrier density in parallel conduction layers of quantum Hall systems
M. Grayson and F. Fischer
J. Appl. Phys. **98**, 013709 (2005)

Embedded atom simulations of titanium systems with grain boundaries
T. Hammerschmidt, A. Kersch, and P. Vogl
Phys. Rev. B **71**, 205409 (2005)

Progress towards single spin optoelectronics using quantum dot nanostructures
D. Heiss, M. Kroutvar, J. J. Finley, and G. Abstreiter
Sol. Stat. Comm. **135**, 591-601 (2005)

Highly Si-doped AlN grown by plasma-assisted molecular-beam epitaxy
M. Hermann, F. Furtmayr, A. Bergmaier, G. Dollinger, M. Stutzmann, and M. Eickhoff
Appl. Phys. Lett. **86**, 192108 (2005)

Design and optimization of vertical CEO-T-FETs with atomically precise ultrashort gates by simulation with quantum transport models
J. Höntschel, W. Klix, R. Stenzel, F. Ertl, and G. Abstreiter
in: Proc. of 27th International Conference on the Physics of Semiconductors, eds: J. Menéndez and C. G. Van de Walle, AIP Conference Proc. **772** (2005), p.1501-1502

Structure of a single sharp quantum Hall edge probed by momemtum-resolved tunneling
M. Huber, M. Grayson, M. Rother, W. Biberacher, W. Wegscheider, and G. Abstreiter
Phys. Rev. Lett. **94**, 016805 (2005)

Spin effects in a quantum ring
T. Ihn, A. Fuhrer, K. Ensslin, W. Wegscheider, and M. Bichler
Physica E **26**, 225-230 (2005)

32nm digitally tunable laser diode with a 0.58nm wavelength grid using a vertically integrated Mach-Zehnder interferometer
T. Jacke, R. Todt, R. Meyer, and M.-C. Amann
Appl. Phys. Lett. **87**, 201113 (2005)

Buried heterostructure laser with vertically-integrated Mach-Zehnder interferometer for Vernier-effect-based wide wavelength tuning
T. Jacke, R. Todt, and M.-C. Amann
IEE Proc. Optoelectronics **152**, No. 2, 72-76 (2005)

Widely tunable Mach-Zehnder interferometer laser with improved tuning efficiency
T. Jacke, R. Todt, M. Rahim, and M.-C. Amann
Electron. Lett. **41**, No. 5, 45-46 (2005)

30nm digitally tunable laser with a 0.57nm frequency grid
T. Jacke, R. Todt, R. Meyer, and M.-C. Amann
in: Proc. of CLEO/Europe 2005, CP1-7-THU (postdeadline), Munich, Germany (2005)

Deposition of microcrystalline silicon prepared by hot-wire chemical-vapor deposition: The influence of the deposition parameters on the material properties and solar cell performance
S. Klein, F. Finger, R. Carius, and M. Stutzmann
J. Appl. Phys. **98**, 024905 (2005)

Long-wavelength MEMS tunable VCSEL with high sidemode supression
B. Kögel, M. Maute, H. Halbritter, F. Riemenschneider, G. Böhm, M.-C. Amann, and P. Meissner
IEEE/LEOS International Conference on Optical MEMS and Their Applications (MOEMS 2005), Oulu, Finland (2005)

High single mode output power from long-wavelength VCSELs using curved micro-mirrors for mode control
B. Kögel, M. Maute, H. Halbritter, S. Jatta, G. Böhm, M.-C. Amann, and P. Meissner
IEEE Electron. Lett. **41**, No. 17, 43-44 (2005)

Direct observation of controlled coupling in an individual quantum dot molecule
H. J. Krenner, M. Sabathil, E. C. Clark, A. Kress, D. Schuh, M. Bichler, G. Abstreiter, and J. J. Finley
Phys. Rev. Lett. **94**, 057402 (2005)

Recent advances in exciton-based quantum information processing in quantum dot nanostructures
H. J. Krenner, S. Stufler, M. Sabathil, E. C. Clark, P. Ester, M. Bichler, G. Abstreiter, J. J. Finley, and A. Zrenner
New Journal of Physics **7**, 184 (2005)

Manipulation of the spontaneous emission dynamics of quantum dots in two-dimensional photonic crystals
A. Kress, F. Hofbauer, N. Reinelt, M. Kaniber, H. J. Krenner, R. Meyer, G. Böhm, and J. J. Finley
Phys. Rev. B **71**, 241304 (R) (2005)

Investigation of cavity modes and direct observation of Purcell enhancement in 2D photonic crystal defect microcavities
A. Kress, F. Hofbauer, N. Reinelt, H. J. Krenner, M. Bichler, D. Schuh, R. Meyer, G. Abstreiter, and J. J. Finley
Physica E **26**, 351-355 (2005)

Direct observation of controlled coupling in an individual quantum dot molecule
H. J. Krenner, M. Sabathil, E. C. Clark, A. Kress, D. Schuh, M. Bichler, G. Abstreiter, and J. J. Finley
Phys. Rev. Lett. **94**, 057402 (2005)

Spectrum of one-dimensional plasmons in a single stripe of two-dimensional electrons
I. V. Kukushkin, J. H. Smet, V. A. Kovalskii, S. I. Gubarev, K. von Klitzing, and W. Wegscheider
Phys. Rev. B **72**, 161317 (2005)

Cyclotron spin-flip mode as the lowest-energy excitation of unpolarized integer quantum Hall states
L. V. Kulik, I. V. Kukushkin, S. Dickmann, V. E. Kirpichev, A. B. Van`kov, A. L. Parakhonsky, J. H. Smet, K. von Klitzing, and W. Wegscheider
Phys. Rev. B **72**, 073304 (2005)

Modulation bandwidths of widely tunable SG-TTG laser diodes
R. Laroy, G. Morthier, R. Todt, R. Meyer, M.-C. Amann, and R. Baets
European Semiconductor Laser Workshop (ESLW), Glasgow, UK (2005)

Calculation of the linewidth broadening in vertical-cavity surface-emitting lasers due to temperature fluctuations
C. Lauer and M.-C. Amann
Appl. Phys. Lett. **86**, 191108 (2005)

Laser hygrometer using a vertical-cavity surface-emitting laser (VCSEL) with an emission wavelength of 1.84µm
C. Lauer, S. Szalay, G. Böhm, C. Lin, F. Köhler, and M.-C. Amann
IEEE Trans. Inst. and Meas. **54**, No. 3, 1214-1218 (2005)

VCSELs emerge as low-cost alternatives to edge-emitters
C. Lauer, M. Maute, W. Hofmann, and M.-C. Amann
Laser Focus World **41**, No. 6, 127-131 (2005)

Modeling the nonlinear photoluminescence intensity dependence observed in asymmetric GaN quantum discs with AlGaN barriers
K. H. Lee, S. Birner, J. H. Na, R. A. Taylor, J. W. Robinson, J. H. Rice, Y. S. Park, C. M. Park, and T. W. Kang
in: Proceedings of the 5th IEEE Conference on Nanotechnology, Nagoya, Japan, **547** (2005)

Nanometre spaced electrodes on a cleaved AlGaAs surface
S. M. Luber, S. Strobel, H.-P. Tranitz, W. Wegscheider, D. Schuh, and M. Tornow
Nanotechnology **16**, 1182 (2005)

Contact block reduction method for ballistic transport and carrier densities of open nanostructures
D. Mamaluy, D. Vasileska, M. Sabathil, T. Zibold, and P. Vogl
Phys. Rev. B **71**, 245321 (2005)

Mn-rich clusters in GaN: Hexagonal or cubic symmetry?
G. Martinez-Criado, A. Somogyj, S. Ramos, J. Campo, R. Tucoulou, M. Salome, J. Susini, M. Hermann, M. Eickhoff, and M. Stutzmann
Appl. Phys. Lett. **86**, 131927 (2005)

Long-wavelength tunable vertical-cavity surface-emitting lasers and the influence of coupled cavities
M. Maute, G. Böhm, M. Amann, B. Kögel, H. Halbritter, and P. Meissner
Opt. Express **13**, No. 20, 8008-8014 (2005)

Coupled cavity phenomena within MEMS-tunable long-wavelength VCSELs
M. Maute, G. Boehm, F. Riemenschneider, B. Kögel, P. Meissner, M. Ortsiefer, and M.-C. Amann
Conference on Lasers and Electro-Optics (CLEO), CThA4, Baltimore, USA (2005)

Widely tunable twin-guide laser diodes with over 40nm-tuning range
R. Todt, T. Jacke, R. Meyer, J. Adler, R. Laroy, G. Morthier, and M.-C. Amann
in: Proc. of the 32nd International Symposium on Compound Semiconductors (ISCS), paper Tu3.6, Rust, Germany (2005)

Aluminum arsenide cleaved-edge overgrown quantum wires
J. Moser, T. Zibold, D. Schuh, M. Bichler, F. Ertl, G. Abstreiter, M. Grayson, S. Roddaro, and V. Pellegrini
Appl. Phys. Lett. **87**, 052101 (2005)

Anomalous Stark shifts in single vertically coupled pairs of InGaAs quantum dots
R. Oulton, A. I. Tartakovskii, A. Ebbens, J. J. Finley, D. J. Mowbray, M. S. Skolnick, and M. Hopkinson
Physica E **26**, 302-307 (2005)

Hydroxyapatite kinetic deposition on solid substrates induced by laser-liquid-solid interaction
L. Pramatarova, E. Pecheva, T. Petrov, R. Presker, and M. Stutzmann
(13th Int. School on Quantum Electronics: Laser Physics and Applications)
in: Proc. of SPIE, Vol. **5830**, 419, ed. by P. A. Atanasov, S. V. Gateva, L. A. Avramov, and A. A. Serafetinides, SPIE, Bellingham, WA (2005)

A novel laser-liquid-solid interaction process for hydroxyapatite formation on porous silicon
L. Pramatarova, E. Pecheva, D. Dimova-Malinovska, R. Presker, M. Stutzmann, U. Schwarz, and R. Kniep
(13th Int. School on Quantum Electronics: Laser Physics and Applications)
in: Proc. of SPIE, **Vol.** 5830, 110, ed. by P. A. Atanasov, S. V. Gateva, L. A. Avramov, and A. A. Serafetinides, SPIE, Bellingham, WA (2005)

Towards a new quantum wire structure realizable by double cleaved-edge overgrowth: Characterizing the transfer potential
S. F. Roth, M. Grayson, M. Bichler, D. Schuh, and G. Abstreiter
in: Proc. of the 27th International Conference on the Physics of Semiconductors, Eds: J. Menéndez and C. G. Van de Walle, AIP Conference Proc. **772** (2005), p. 915-916

Field-effect induced mid-infrared intersubband electroluminescence of quantum wire cascade structures
S. Schmult, T. Herrle, H.-P. Tranitz, M. Reinwald, W. Wegscheider, M. Bichler, D. Schuh, and G. Abstreiter
in: Proc. of the 27th International Conference on the Physics of Semiconductors, Eds: J. Menéndez and C. G. Van de Walle, AIP Conference Proc. **772** (2005), p. 443-444

Controlled positioning of self-assembled InAs quantum dots on (110) GaAs
D. Schuh, J. Bauer, E. Uccelli, R. Schulz, A. Kress, F. Hofbauer, J. J. Finley, and G. Abstreiter
Physica E **26**, 72-76 (2005)

Effects of strain and confinement on the emission wavelength of InAs quantum dots due to a $GaAs_{1-x}N_x$ capping layer
O. Schumann, S. Birner, M. Baudach, L. Geelhaar, H. Eisele, L. Ivanova, R. Timm, A. Lenz, S. K. Becker, M. Povolotskyi, M. Dähne, G. Abstreiter, and H. Riechert
Phys. Rev. B **71**, 245316 (2005) &
Virtual Journal of Nanoscale Science Technology **12** (1) (2005)

Purely strain induced GaAs/InAlAs single quantum wires exhibiting strong charge carrier confinement
R. Schuster, H. Hajak, M. Reinwald, W. Wegscheider, D. Schuh, M. Bichler, S. Birner, P. Vogl, and G. Abstreiter
AIP Conf. Proc. **772**, 898 (2005)

Proceedings MRS Spring Meeting 2005 (Warrendale, PA)
Symposium H – Giant-Area Electronics on Nonconventional Substrates
Eds.: M. S. Shur, P. Wilson, and M. Stutzmann
Material Research Society Proc. Vol. **870E** (Electronic-Only Publication)

Recording of cell action potentials with AlGaN/GaN field-effect transistors
G. Steinhoff, B. Baur, G. Wrobel, S. Ingebrandt, A. Offenhäusser, A. Dadgar, A. Krost, M. Stutzmann, and M. Eickhoff
Appl. Phys. Lett. **86**, 033901-1-3 (2005)

AlGaN/GaN electrolyte-gate field-effect transistors as transducers for bioelectronic devices
G. Steinhoff, B. Baur, H.-G. von Ribbeck, G. Wrobel, S. Ingebrandt, A. Offenhäusser, M. Stutzmann, and M. Eickhoff
Adv. in Solid State Phys. **45**, 349 (2005)

Quantum optical properties of a single $In_xGa_{1-x}As$-GaAs quantum dot two-level system
S. Stufler, P. Ester, A. Zrenner, and M. Bichler
Phys. Rev. B **72**, 121301 (R) 2005

Raman scattering of folded acoustic phonons in self – assembled Si/Ge dot superlattices
P. H. Tan, D. Bougeard, G. Abstreiter, and K. Brunner
Chinese Journal of Light Scattering **17**, 312-314 (2005)

Depth profile of strain and composition in Si/Ge dot multilayers by microscopic phonon Raman spectroscopy
P. H. Tan, D. Bougeard, G. Abstreiter, and K. Brunner
J. Appl. Phys. **98**, 113517 (2005)

Influence of facet reflections on monolithic widely tunable laser diodes
R. Todt and M.-C. Amann
IEEE Photon. Technol. Lett. **17**, No. 12, 2520-2522 (2005)

Sampled grating tunable twin-guide laser diodes with over 40nm electronic tuning range
R. Todt, T. Jacke, R. Meyer, J. Adler, R. Laroy, G. Morthier, and M.-C. Amann
IEEE Photon. Technol. Lett. **17**, No. 12, 2514-2516 (2005)

Tunable twin-guide (TTG) distributed feedback (DFB) laser diodes with over 9nm continuous electro-optic tuning range
R. Todt, T. Jacke, R. Meyer, J. Adler, and M.-C. Amann
Electron. Lett. **41**, No. 19, 1063-1065 (2005)

State-of-the-art performance of widely tunable twin-guide laser diodes
R. Todt, T. Jacke, R. Meyer, J. Adler, R. Laroy, G. Morthier, and M.-C. Amann
European Semiconductor Laser Workshop (ESLW), Glasgow, UK (2005)

Thermally widely tunable laser diodes with distributed feedback
R. Todt, T. Jacke, R. Meyer, and M.-C. Amann
in: Proc. of the 31st European Conference on Optical Communication (ECOC), We4.P.77, Glasgow, UK (2005)

Thermally widely tunable laser diodes with distributed feedback
R. Todt, T. Jacke, R. Meyer, and M.-C. Amann
Appl. Phys. Lett. **87**, No. 2, 021103 (2005)

Widely tunable twin-guide laser diodes at 1.55µm
R. Todt, T. Jacke, R. Meyer, J. Adler, R. Laroy, G. Morthier, and M.-C. Amann
in: Proc. of the OptoElectronics and Communications Conference, post-deadline paper PDP_07, Seoul, Korea (2005)

Demonstration of Vernier effect tuning in tunable twin-guide laser diodes
R. Todt, T. Jacke, R. Laroy, G. Morthier, and M.-C. Amann
IEEE Proc. Optoelectronics **152**, No. 2, 66-71 (2005)

High output power tunable twin-guide laser diodes with improved lateral current injection structure
R. Todt, T. Jacke, R. Meyer, and M.-C. Amann
Electron. Lett. **41**, No. 4, 190-191 (2005)

Wide wavelength tuning of sampled-grating tunable twin-guide laser diodes
R. Todt, T. Jacke, R. Meyer, M.-C. Amann, R. Laroy, and G. Morthier
in: Proc. of the SPIE Conference Photonics West 2005, San Jose, USA (2005)

Spin-preserving ultrafast carrier capture and relaxation in InGaAs quantum dots
S. Trumm, M. Wesseli, H. J. Krenner, D. Schuh, M. Bichler, J. J. Finley, and M. Betz
Appl. Phys. Lett. **87**, 153113 (2005)

Influence of thermal oxidation on the electronic properties of Pt Schottky contacts on GaN grown by molecular beam epitaxy
O. Weidemann, E. Monroy, E. Hahn, M. Stutzmann, and M. Eickhoff
Appl. Phys. Lett. **86**, 083507 (2005)

Determination of the polarization discontinuity at the AlGaN/GaN interface by electro-reflectance spectroscopy
A. Winzer, R. Goldhahn, G. Gobsch, A. Link, M. Eickhoff, U. Rossow, and A. Hangleiter
Appl. Phys. Lett. **86,** 181912 (2005)

Calculation of carrier transport through quantum dot molecules
T. Zibold, M. Sabathil, D. Mamluy, and P. Vogl
AIP Conf. Proc. **722**, 799 (2005)

7. Invited Talks

Gerhard Abstreiter

1. *Optoelectronic control of single charge and spin in semiconductor quantum dots*
   Kolloquiumsvortrag, TU Delft, The Netherlands (22.2.2005)

2. *Novel developments in Si based hetero- and nanostructures*
   EuroMBE Workshop Grindelwald, Switzerland (8.3.2005)

3. *Spin doping and electronic coupling of self-assembled quantum dots*
   Special Symposium: 25 years Mauterndorf Winterschool, Austria (29.3.2005)

4. *Halbleiternanostrukturen – Basis für Quantum-Informationstechnologie?*
   Siemens-Stiftung München, Germany (11.4.2005)

5. *History and novel developments in SiGe based hetero- and nanostructures*
   (Plenary Talk)
   Int. Conference on Si Epitaxy and Heterostructures, Osaka, Japan (25.5.2005)

6. *Optically controlling charge of semiconductor and spin excitations in InGaAs quantum dots*
   Workshop on Growth, Electronic and Optical Properties of Semiconductor Nanostructures, Kühlingsborn, Germany (9.6.2005)

7. *Semiconductor nanostructures: science and possible implications for quantum information technology* (Plenary Talk)
   Italian Condensed Matter Physics Meeting, Genua, Italy (23.6.2005)

8. *Single semiconductor quantum dots – basic studies and novel devices I and II*
   BaCaTeC - Summer School, Würzburg, Germany (30.6.2005)

9. *Charge and spin excitations in single and coupled quantum dots* (Plenary Talk)
   Int. Conferences EP2DS-16 and MSS12, Albuquerque, USA (9.7.2005)

10. *Single and coupled quantum dots – spectroscopy and coherent control*
    NATO Advanced Study Institut, Cluj, Rumänien (4.-8.9.2005)

11. *Coupled quantum dots charge and spin storage in quantum dots*
    NATO Advanced Study Institut, Cluj, Rumänien (4.-8.9.2005)

12. *Spins in Si/Ge based systems*
    NATO Advanced Study Institut, Cluj, Rumänien (4.-8.9.2005)

13. *AlAs Nanostrukturen als quantengekoppelte Systeme/Gekoppelte Quantenpunkttransistoren in präziser Kettenanordnung*
BMBF NanoQuit meeting Ringberg, Tegernsee, Germany (26.9.2005)

14. *Tag der offenen Tür: Wunderbar Winziges - Die Welt der Nanowissenschaften*
TU München, Physik-Department, Garching, Germany (22.10.2005)

15. *Wunderbar Winziges - Einblicke in die Welt der Nano-Wissenschaften*
Deutsches Musem, München, Germany (16.11.2005)

16. *Charge and spin excitations in single and coupled quantum dots*
Int. Symposium on Quantum Dots and Nanoelectronics, Tokyo, Japan (18.11.2005)

Markus-Christian Amann

1. *Einmodige und abstimmbare oberflächenemittierende Laserdioden*
Eröffnungsveranstaltung des GK Steuerbare Komponenten in der Mikrowellentechnik und Optik, Darmstadt, Germany (25.2.2005)

2. *Long wavelength VCSEL´s*
Optical Fiber Communication Conference, Anaheim, USA (6.-11.3.2005)

3. *Single-mode and wavelength-tunable long-wavelength VCSEL´s*
OptoElectronics and Communications Conference, Seoul, Korea (4.-8.7.2005)

4. *Recent progress on MIR laser diodes*
Mid-infrared Optoelectronics: Materials and Devices VII, Lancaster, England (12.-14.9.2005)

5. *Licht ins analytische Dunkel – Laseroptische Gas- und Flüssigkeitssensorik*
VDE Arbeitskreis Medizintechnik & LifeScience Electronic, München, Germany (15.11.2005)

6. *Halbleiterlichtquellen – Anwendungen in der Gas-Sensorik*
OTTI – Profiforum, Regensburg, Germany (15.12.2005)

Stefan Birner

1. *Modeling of purely strain-induced CEO GaAs/InAlAs quantum wires*
5th International Conference Numerical Simulation of Optoelectronic Devices
Berlin, Germany (19.-22.09.2005)

Dominique Bougeard

1. *Group IV materials based spintronics*
   Seminar, Department of Electronic Engineering, University of Tokyo, Japan (6.10.2005)

Martin S. Brandt

1. *Hydrogen in ferromagnetic semiconductors*
   Japan-Germany Colloquium 2005: Semiconductor Science and Technology Dresden, Germany (14.2.2005)

2. *Ferromagnetische Halbleiter: Ordnung durch bewegliche Ladung*
   Physikalisches Kolloquium, Universität Ulm, Germany (9.5.2005)

3. *Spin-basierte Bauelemente auf Si-Basis*
   VDE/VDI-Workshop "Devices nach CMOS", München, Germany (17.6.2005)

4. *Hydrogen-manganese complexes in magnetic semiconductors*
   ESRF, Genoble, France (11.7.2005)

5. EPR characterization and its application to defects in magnetic semiconductors (Tutorial) 23rd Intern. Conference on Defects in Semiconductors Awaji Island, Japan (24.7.2005)

6. Functionalisation of silicon quantum dots and nanowires
   21st Intern. Conference on Amorphous and Nanocrystalline Semiconductors Lisbon, Portugal (8.9.2005)

7. *Spin effects in Si-based systems*
   University of Tokyo/Technische Universität München-Symposium on Nanosciences Tokyo, Japan (5.10.2005)

8. *Nanostrukturen für Quanteninformationsverarbeitung und Bioelektronik*
   Kolloquium, Forschungszentrum Jülich, Germany (8.10.2005)

Martin Eickhoff

1. *Group III-nitrides for biosensor applications*
   International Topical Workshop on Heteroepitaxy of 3C-SiC on Silicon and its Application to Sensor Devices, Krippen, Germany (29.4.2005)

2. *Group III-nitrides for biosensors*
   6th International Conference on Nitride Semiconductors, ICNS-6, Bremen, Germany (30.8.2005)

3. *Group III-nitrides as a substrate material for biosensor applications*
   4th IEEE Conference on Sensors, IEEE Sensors 2005, Irvine, CA, USA (2.11.2005)

Jonathan Finley

1. *Semiconductor nanodots: artificial atoms and molecules for solid state quantumoOptics*
   CENS Seminar, LMU Munich, Germany (21.1.2005)

2. *An optically programmable quantum dot electron spin memory*
   NNCI2005 Conference, NTT-Atsugi Laboratories, Japan (1.2.2005)

3. *Probing charge and spin excitations in artificial atoms and molecules*
   CAPS Seminar, Universität Konstanz, Germany (17.2.2005)

4. *Optically probing charge and spin excitations in quantum dots and molecules*
   Gordon Research Conference, Quantum Information Processing using Solid State Systems, Ventura, California, USA.(2.3.2005)

5. *Optically probing charge and spin excitations in quantum dots and molecules*
   DPG Frühjahrstagung, Berlin, Germany (5.3.2005)

6. *Semiconductor artificial atoms*
   Seminar, Technische Universität München E11, Germany (23.5.2005)

7. *Optically controlling charge and spin excitations in InGaAs quantum dots and molecules*
   W&E Hereaus Seminar "Trions in Semiconductor Nanostructures", Bad Honnef, Germany (29.5.2005)

8. *An optically programmable quantum dot electron spin memory*
   EMRS Conference, Strasbourg, France (31.5.2005)

9. *Optically probing charge and spin excitations quantum dot nanostructures*
   Nanostructures Seminar, University Sheffield, UK (17.6.2005)

10. *Optically probing charge and spin excitations in quantum dots and molecules*
    Optical Properties of Excitons in Confined Systems OECS-9, U. Southampton, UK (5.9.2005)

11. *Optically probing charge and spin excitations in InGaAs quantum dots and molecules*
    SSDM 2005 Conference, Kobe, Japan (13.9.2005)

12. *Optically probing charge and spin excitations in quantum dots and molecules*
    Bilateral Nanoscience Symposium, University Tokyo, Japan (5.10.2005)

13. *Semiconductor quantum dots, molecules and their coupling to photons*
    University of Tokyo, Arakawa Group, Japan (6.10.2005)

14. *Semiconductor quantum dots, molecules and their coupling to photons*
    NTT Basic Research Laboratories, Hirayama Group, Japan (7.10.2005)

15. *Probing charge and spin excitations in quantum dots and molecules*
    GDEST Conference, Max Planck Gesellschaft, München, Germany (9.12.2005)

José Antonio Garrido Ariza

1. *Enzyme-modified diamond biosensors*
   Surface and Bulk Defects in CVD Diamond Films, X, Hasselt, Belgium (23.-25.2.2005)

2. *Enzyme-modified nanocrystalline diamond electrodes for biosensor applications*
   MRS-Spring Meeting 2005, San Francisco, USA (28.3-1.4.2005)

3. *Enzyme-modified nanocrystalline diamond electrodes for biosensor applications*
   8th International Conference on Applications of Diamond and Related Materials at Argonne National Laboratory, Argonne, Il, USA (15.-19.5.2005)

4. *Diamond based biosensors*
   16th European Conference on Diamond, Toulouse, France (1.-16.9.2005)

5. *Diamond surfaces: a novel platform for biosensors*
   Seminar, Max Bergmann Center of Biomaterials, Dresden, Germany (17.11.2005)

Matthew Grayson

1. *Bending the quantum Hall effect: Evidence for new one-dimensional phase transitions*
   DFG Schwerpunkt Programm, Bad Honnef, Germany (24.1.2005)

2. *Bending the quantum Hall effect: Evidence for new one-dimensional phase transitions*
   International Conference on Strongly Correlated Electron Systems ‘05, Vienna, Austria (30.7.2005)

3. *Bending the quantum Hall effect: Novel metallic and insulating states in one dimension*
Seminar, Stanford University, La Jolla, California, USA (10.10.2005)

4. *Bending the quantum Hall effect: Novel metallic and insulating states in one dimension*
Seminar, University of California, Berkeley, California, USA (11.10.2005)

5. *Bending the quantum Hall effect: Novel metallic and insulating states in one dimension*
Seminar, University of California, Los Angeles, California, USA (12.10.2005)

6. *Bending the quantum Hall effect: Novel metallic and insulating states in one dimension*
Seminar, University of California, Santa Barbara, California, USA (13.10.2005)

7. *Bending the quantum Hall effect: Novel metallic and insulating states in one dimension*
Seminar, California Technical University, Pasadena, California, USA (14.10.2005)

8. *Bending the quantum Hall effect: Novel metallic and insulating states in one dimension*
Seminar, Princeton University, Princeton, New Jersey, USA (17.10.2005)

9. *Bending the quantum Hall effect: Novel metallic and insulating states in one dimension*
Seminar, Yale University, New Haven, Connecticut, USA (19.10.2005)

10. *Bending the quantum Hall effect: Novel metallic and insulating states in one dimension*
Colloquium, Case Western Reserve University, Cleveland, Ohio, USA (20.10.2005)

11. *Quantum confined structures in aluminum arsenide*
COLLECT Meeting, Columbia University, New York, USA (21.10.2005)

12. *Bending the quantum Hall effect: Novel metallic and insulating states in one dimension*
Seminar, Rutgers University, Piscataway, New Jersey, USA (25.10.2005)

13. *Anomalous magnetoresistance peaks in 2D (110) GaAs holes: Heavy-hole spin anticrossings*
Seminar, Scuola Normale Superiore, Pisa, Italy (5.12.2005)

14. *Bending the quantum Hall effect: Novel metallic and insulating states in one dimension*
Colloquium, Technische Universität München, Germany (15.12.2005)

Dominik Heiss

1. *Dynamics of optically generated single electron spins in self-assembled quantum dots*
   Nanoforum 2005, Johannes Keppler Universität Linz, Austria (27.5.2005)

Andreas Kress

1. *High quality photonic crystal nano-cavities for solid state quantum optics*
   Nanoforum 2005, Johannes Keppler Universität Linz, Austria (27.5.2005)

Ulrich Rant

1. *Electrical manipulation of DNA on gold*
   Boston University, USA (4.11.2005)

Georg Steinhoff

1. *Biosensor applications of AlGaN/GaN solution gate field effect transistors*
   Annual Meeting of the German Physical Society (DPG), Symposium Bio- and Neurotransistors, Berlin, Germany (8.3.2005)

Martin Stutzmann

1. *Biofunktionalisierung von Halbleiter-Oberflächen*
   Seminar, Institut für Physik, Technische Universität Ilmenau, Germany (11.1.2005)

2. *Nanotechnologie - quo vadis?*
   Kolloquium Fachbereich Physik, Philipps-Universität Marburg, Germany (27.1.2005)

3. *Cells meet chips: Neue Halbleiter-Bauelemente für die Bioelektronik*
   Institut für Theoretische Physik, Universität Göttingen, Germany (30.5.2005)

4. *Neue Halbleiter-Bauelemente für die Bioelektronik*
   Elektrotechnisches Kolloquium, Universität Ulm, Germany (1.6.2005)

5. *Biofunctionalized semiconductors*
   IUVSTA International Summer School, Science and Technology at Nanoscale, Tři Studně, Czech Republic (6.-11.6.2005)

6. *Semiconductors meet biology: challenges and opportunities*
   INESC, Lisbon, Portugal (10.10.2005)

7. *Semiconductor nanostructures as biosensors*
   1st Russian-Bavarian Conference on Bio-Medical Engineering, Munich, Germany (13.-14.10.2005)

8. *III-nitride research at the Walter Schottky Institut: an overview*
   University Madrid, Spain (25.11.2005)

9. *Bioelectronics with wide band gap semiconductors*
   Nanotechnology Symposium, Waseda University, Toky, Japan (6.12.2005)

Marc Tornow

1. *Orientation switching of DNA layers as a new detection scheme in bio-sensing*
   Seminar, Goethe-Universität Frankfurt, Institut für Biochemie, Biozentrum, Frankfurt, Germany (25.1.2005)

2. *Orientation switching of functional DNA monolayers*
   European Science Foundation (ESF) Exploratory Workshop "Nanowires: Bridging the Gaps between Materials Science and Biology", Bad Hofgastein, Austria, (26.5.2005)

3. *Orientation switching of DNA layers as a new detection scheme in bio-sensing*
   Seminar, IPHT, Abt. Biotechnische Mikrosysteme, Institut für Physikalische Hochtechnologie, Jena, Germany (13.6.2005)

4. *DNA as a nanoelectromechanical system*
   Hauptseminar, TU München, Fakultät für Elektrotechnik und Informationstechnik Lehrstuhl für Nanoelektronik, München, Germany (23.6.2005)

5. *Silicon-on-insulator as a functional substrate for bio-organic systems*
   International Workshop "Functional Solid-Supported Bimolecular Lipid Membranes", Max-Planck-Institute for Polymer Research, Mainz, Schloss Ringberg, Tegernsee, Germany (18.-21.9.2005)

6. *Nanogap electrodes for molecular bio-electronics*
   "University of Tokyo – TU Munich", Bilateral Symposium on Nanosciences, Institute of Industrial Science, Komaba II Campus, University of Tokyo, Japan (5.10.2005)

7. *Orientation switching of functional DNA* monolayers: *applications in bio-nanotechnology*
   Seminar, Princeton University, Department of Chemistry, Princeton NJ, USA, (4.11.2005)

Alexandros Trellakis

1. *Simulation of 3D quantum structures with Nextnano^3*
IR-ON Workshop 2005, Bad Ischl, Austria (3.-4.11.2005)

2. *Efficient solution of the Schrödinger equation in semiconductor device simulations*
5th Int. Conference on Large-Scale Computations, Sozopol, Bulgaria (6.-10.6.2005)

Peter Vogl

1. *nextnano3, a versatile simulation tool for nanostructures and nanodevices*
Tokyo-Munich Bilateral Symposium on Nanosciences 4.-6.10.2005, IIS, University of Tokyo, Komaba Campus, Japan (5.10.2005)

8. Courses, Seminars, and other Scientific Activities

Lectures

Gerhard Abstreiter

WS 2004/2005	Sabbatical
SS 2005	Halbleiterphysik II – Physik niedrigdimensionaler Systeme (Physics of low dimensional systems)
	Moderne Materialphysik für Lehramt Gymnasium
WS 2005/2006	Grundlagen der Halbleiterphysik (Introduction to semiconductor physics)
	Experimental Physics I together with Matthew Grayson

Markus-Christian Amann

WS 2004/2005	Werkstoffe der Elektrotechnik (Materials for electrical engineering)
	Technologie der III/V-Halbleiterbauelemente (Technology of III/V semiconductor devices) together with Ralf Meyer
	Optoelektronik II (Optoelectronics II)
SS 2005	Optoelektronik I (Optoelectronics I)
	Optoelectronics
WS 2005/2006	Werkstoffe der Elektrotechnik (Materials for electrical engineering)
	Technologie der III/V-Halbleiterbauelemente (Technology of III/V semiconductor devices) together with Ralf Meyer
	Optoelektronik II (Optoelectronics II)

Martin Brandt

WS 2004/2005	Quantum computing
SS 2005	Halbleiterphysik II – Spintronik Spins in Festkörpern: Von Defekten zur Spintronik
WS 2005/2006	Experimentalphysik 1 für Chemiker
	Quantum computing
	Seminar zu aktuellen Fragen der Spintronik

Manfred Claassen

WS 2004/2005	Hochfrequenz-Elektronik (High-frequency electronics)
	Partielle Differentialgleichungen in der Elektrotechnik (Partial differential equations in electrical engineering)
	Technische Elektrizitätslehre 1 (Electrical engineering 1)
SS 2005	Optische Schaltungen (Optical circuits)
	Nichtlineare Schwingungsvorgänge (Nonlinear oscillations)

Jonathan Finley

WS 2004/2005	Semiconductor science and nanotechnology I
SS 2005	Semiconductor science and nanotechnology II
WS 2005/2006	Semiconductor science and nanotechnology I together with Mattew Grayson
	Optics of nanoscale systems I

Martin Stutzmann

WS 2004/2005	Grundlagen der Halbleiterphysik (Introduction to semiconductor physics)
	Tutorium zu Halbleiterphysik (Tutorial semiconductor physics)

	Bio- and nanoelectronic systems 1 together with Martin Eickhoff and Marc Tornow
	Biochemical sensors together with José Antonio Garrido Ariza
SS 2005	Halbleiterphysik II – Moderne Bauelemente
	Bio- and nanelectronic systems 2 together with Martin Eickhoff and Marc Tornow
	Organic electronics: physics and applications together with José Antonio Garrido Ariza
	Renewable energy together with Martin Eickhoff
	Solid state spectroscopy
WS 2005/2006	Einführung in die Festkörperphysik 1
	Biochemical sensors I together with José Antonio Garrido Ariza

Marc Tornow

WS 2005/2006 Bio- and nanoelectronic systems I

Alex Trellakis

WS 2004/2005 Theoretical physics 3 (Quantum mechanics)

Peter Vogl

WS 2004/2005	Theoretische Physik 4A (Quantenmechanik II) (Theoretical physics 4A (Quantum mechanics II)
SS 2005	Theoretische Physik 1 - Mechanik
WS 2005/2006	Theoretische Physik 4A (Quantenmechanik II) neu

Other Scientific Activities

Stefan Birner

Organisation: next**nano³** workshop in Berlin/Germany (23.9.2005), Erwin Schrödinger Center Adlershof, Humboldt University Berlin

Martin S. Brandt

Member, Program Committee
23rd Intern. Conference on Defects in Semiconductors Awaji Island, Japan, 2005

9. Selected Topics of Semiconductor Physics and Technology

Since1997, all doctoral theses are published in the series: Selected Topics of Semiconductor Physics and Technology, eds.: G. Abstreiter, M.-C. Amann, M. Stutzmann, and P. Vogl. The following volumes appeared so far in this series:

Vol. 1
Cornelia Engel
Si/SiGe basierende Phototransistoren
131 Seiten
ISBN 3-932749-01-4

Vol. 2
Peter Schittenhelm
Selbst-Organisation und Selbst-Ordnung in Si/SiGe-Heterostrukturen
151 Seiten
ISBN 3-932749-02-2

Vol. 3
Andreas Nutsch
Selektive Epitaxie von (GaIn)(AsP) Schichtstrukturen
129 Seiten
ISBN 3-932749-03-0

Vol. 4
Peter Baumgartner
Optische und elektronische Eigenschaften lasergeschriebener GaAs-Nanostrukturen
180 Seiten
ISBN 3-932749-04-9

Vol. 5
Walter Franz Rieger
Untersuchung der elektronischen und strukturellen Eigenschaften von GaNAlN und deren Legierungen
158 Seiten
ISBN 3-932749-05-7

Vol. 6
Markus Hauser
Oberflächenemittierende Laserdioden mit Mehrfachepitaxie
148 Seiten
ISBN 3-932749-06-5

Vol. 7
Markus Sexl
Verspannte und gitterrelaxierte In(GaAl)As Heterostrukturen
144 Seiten
ISBN 3-932749-07-3

Vol. 8
Christian Obermüller
Photolumineszenszspektroskopie mit optischen Nahfeldmethoden an GaAs-Nanostrukturen
140 Seiten
ISBN 3-932749-08-1

Vol. 9
Edilson Silveira
Inelastische Lichtstreuung an niedrig-dimensionalen Halbleiterstrukturen
104 Seiten
ISBN 3-932749-09-X

Vol. 10
Eberhard Christian Rohrer
Photoleitungs-Spektroskopie von Diamant
153 Seiten
ISBN 3-932749-10-03

Vol. 11
Thomas Wimbauer
Magnetische Resonanz-Untersuchungen an modernen Halbleitermaterialien
125 Seiten
ISBN 3-932749-11-1

Vol. 12
Herbert Verhoeven
Thermische Eigenschaften von CVD-Diamantschichten
154 Seiten
ISBN 3-932749-12-X

Vol. 13
Hans-Christoph Ostendorf
Trennung von Volumen- und Oberflächenrekombination in Silizium
128 Seiten
ISBN 3-932749-13-8

Vol. 14
Martin Städele
Dichtefunktionaltheorie mit exaktem Austausch für Halbleiter
202 Seiten
ISBN 3-932749-14-6

Vol. 15
Helmut Angerer
Herstellung von Gruppe III-Nitriden mit Molekularstrahlepitaxie
144 Seiten
ISBN 3-932749-15-4

Vol. 16
Wolfgang Heller
Spektroskopie einzelner Quantenpunkte in magnetischen und elektrischen Feldern
128 Seiten
ISBN 3-932749-16-2

Vol. 17
Molela Moukara
Pseudopotentiale mit exaktem Austausch
117 Seiten
ISBN 3-932749-17-0

Vol. 18
Ralph Oberhuber
Elektronische Struktur und Transport in verspannten Halbleiterschichtsystemen
110 Seiten
ISBN 3-932749-18-9

Vol. 19
Reiner Pech
High-Energy Boron-Implantation into Different Silicon Substrates
158 Seiten
ISBN 3-932749-19-7

Vol. 20
Christoph Martin Engelhardt
Zyklotronresonanz zweidimensionaler Ladungsträgersysteme in Halbleitern, Effekte der Elektron-Elektron-Wechsel-wirkung und Lokalisierung
317 Seiten
ISBN 3-932749-20-0

Vol. 21
Eduard Neufeld
Erbium-dotierte Si/SiGe-Lichtemitter und -Wellenleiter
136 Seiten
ISBN 3-932749-21-9

Vol. 22
Gert Schedelbeck
Optische Eigenschaften von Halbleiter-nanostrukturen hergestellt durch Über-wachsen von Spaltflächen
154 Seiten
ISBN 3-932749-22-7

Vol. 23
Jürgen Zimmer
Optoelektronisches Verhalten von Dünn-schichtbauelementen aus amorphem und mikrokristallinem Silizium
171 Seiten
ISBN 3-932749-23-5

Vol. 24
Berthold Schmidt
Leistungsoptimierung abstimmbarer InGaAsP/InP Halbleiterlaser
85 Seiten
ISBN 3-932749-24-3

Vol. 25
Jianhong Zhu
Ordering of self-assembled Ge and SiGe nanostructures on vicinal Si surfaces
120 Seiten
ISBN 3-932749-25-1

Vol. 26
Gerhard Groos
Herstellung und Charakterisierung von Silizium-Nanostrukturen
168 Seiten
ISBN 3-932749-26-X

Vol. 27
Uwe Hansen
Theorie der Reaktionskinetik an Festkörperoberflächen
119 Seiten
ISBN 3-932749-27-8

Vol. 28
Roman Dimitrov
Herstellung und Charakterisierung von AlGaN/GaN-Transistoren
196 Seiten
ISBN 3-932749-28-6

Vol. 29
Martin Eickhoff
Piezowiderstandsmechanismen in Halbleitern mit großer Bandlücke
151 Seiten
ISBN 3-932749-29-4

Vol. 30
Nikolai Wieser
Ramanspektroskopie an Gruppe III-Nitriden
161 Seiten
ISBN 3-932749-30-8

Vol. 31
Rainer Janssen
Strukturelle und elektronische Eigenschaften amorpher Silizium-Suboxide
275 Seiten
ISBN 3-932749-31-6

Vol. 32
Martin W. Bayerl
Magnetic resonance investigations of group III-nitrides
155 Seiten
ISBN 3-932749-32-4

Vol. 33
Martin Rother
Elektronische Eigenschaften von Halbleiternanostrukturen hergestellt durch Überwachsen von Spaltflächen
196 Seiten
ISBN 3-932749-33-2

Vol. 34
Frank Findeis
Optical spectroscopy on single self-assembled quantum dots
156 Seiten
ISBN 3-932749-34-0

Vol. 35
Markus Ortsiefer
Langwellige Vertikalresonator-Laserdioden im Materialsystem InGaAlAs/InP
152 Seiten
ISBN 3-932749-35-9

Vol. 36
Roland Zeisel
Optoelectronic properties of defects in diamond and AlGaN alloys
140 Seiten
ISBN 3-932749-36-7

Vol. 37
Liwen Chu
Inter- und Intraband Spektroskopie an selbstorganisierten In(Ga)As/GaAs Quantenpunkten
124 Seiten
ISBN 3-932749-37-5

Vol. 38
Christian Alexander Miesner
Intra-Valenzbandspektroskopie an SiGe-Nanostrukturen in Si
100 Seiten
ISBN 3-932749-38-3

Vol. 39
Szabolcs Kátai
Investigation of the nucleation process of chemical vapour deposited diamond films
178 Seiten
ISBN 3-932749-39-1

Vol. 40
Markus Arzberger
Wachstum, Eigenschaften und Anwendungen selbstorganisierter InAs-Quantenpunkte
236 Seiten
ISBN 3-932749-40-5

Vol. 41
Markus Oliver Markmann
Optische Eigenschaften von Erbium in $Si/Si_{1-x}C_x$, $Si/Si_{1-x}Ge_x$ und Si/SiO_x Heterostrukturen
182 Seiten
ISBN 3-932749-41-3

Vol. 42
Rainer Alexander Deutschmann
Two dimensional electron systems in atomically precise periodic potential
210 Seiten
ISBN 3-932749-42-1

Vol. 43
Uwe Karrer
Schottky-Dioden auf Galliumnitrid: Eigenschaften und Anwendungen in der Sensorik
182 Seiten
ISBN 3-932749-43-X

Vol. 44
Günther Anton Johann Vogg
Epitaxial thin films of Si and Ge based Zintl phases and sheet polymers
169 Seiten
ISBN 3-932749-44-8

Vol. 45
Christian Strahberger
Vertikaler Transport und extreme Magnetfelder in Halbleitern
167 Seiten
ISBN 3-932749-45-6

Vol. 46
Jan Schalwig
Feldeffekt-Gassensoren und ihre Anwendung in Abgas-nachbehandlungssystemen
125 Seiten
ISBN 3-932749-46-4

Vol. 47
Christopher Eisele
Novel absorber structures for Si-based thin film solar cells
126 Seiten
ISBN 3-932749-47-2

Vol. 48
Stefan Hackenbuchner
Elektronische Struktur von Halbleiter-Nanobauelementen im thermodynamischen Nichtgleichgewicht
213 Seiten
ISBN 3-932749-48-0

Vol. 49
Andreas Sticht
Herstellung und Charakterisierung von dünnen Silizium/Siliziumoxid-Schichtsystemen
166 Seiten
ISBN 3-932749-49-9

Vol. 50
Giuseppe Scarpa
Design and fabrication of Quantum Cascade Lasers
193 Seiten
ISBN 3-932749-50-2

Vol. 51
Jörg Frankenberger
Optische Untersuchungen an zwei-dimensionalen Ladungsträgersystemen
158 Seiten
ISBN 3-932749-51-0

Vol. 52
Doris Heinrich
Wavelength selective optically induced charge storage in self-assembled semiconductor quantum dots
144 Seiten
ISBN 3-932749-52-9

Vol. 53
Nicolaus Ulbrich
Entwurf und Charakterisierung von Quanten-Kaskadenlasern und Quantenpunktkaskaden
133 Seiten
ISBN 3-932749-53-7

Vol. 54
Lutz Carsten Görgens
Analyse stickstoffhaltiger III-V Halbleiter-Heterosysteme mit hochenergetischen schweren Ionen
116 Seiten
ISBN 3-932749-54-5

Vol. 55
Andreas Janotta
Doping, light-induced modification and biocompatibility of amorphous silicon suboxides
180 Seiten
ISBN 3-932749-55-3

Vol. 56
Sebastian Tobias Benedikt Gönnenwein
Two-dimensional electron gases and ferromagnetic semiconductors: materials for spintronics
198 Seiten
ISBN 3-932749-56-1

Vol. 57
Evelin Beham
Photostromspektroskopie an einzelnen Quantenpunkten
186 Seiten
ISBN 3-932749-57-X

Vol. 58
Po-Wen Chiu
Towards carbon nanotube-based molecular electronics
116 Seiten
ISBN 3-932749-58-8

Vol. 59
Tobias Graf
Spin-spin interactions of localized electronic states in semiconductors
194 Seiten
ISBN 3-932749-59-6

Vol. 60
Stefan Klein
Microcrystalline silicon prepared by hot wire CVD: preparation and characterisation of material and solar cells
157 Seiten
ISBN 3-932749-60-X

Vol. 61
Markus Krach
Frequenzverdreifacher mit Anti-Seriellem Schottky-Varaktor für den Terahertz-Bereich
156 Seiten
ISBN 3-932749-61-8

Vol. 62
Ralph Thomas Neuberger
AlGaN/GaN-Heterostrukturen als chemische Sensoren in korrosiven Medien
153 Seiten
ISBN 3-932749-62-6

Vol. 63
Sonia Perna
Wasserstoff-Passivierung von tri-kristallinem Silizium durch hydro-genisiertes Siliziumnitrid
136 Seiten
ISBN 3-932749-63-4

Vol. 64
Oliver Schumann
Einfluss von Stickstoff auf das Wachstum und die Eigenschaften von InAs-Quantenpunkten
148 Seiten
ISBN 3-932749-64-2

Vol. 65
Gerhard Rösel
Entwicklung und Charakterisierung von Typ-II-Heterostrukturen für die Abstimmregion in abstimmbaren Laserdioden
101 Seiten
ISBN 3-932749-65-0

Vol. 66
Angela Link
Zweidimensionale Elektronen- und Löcher-Gase in GaN/AlGaN Heterostrukturen
156 Seiten
ISBN 3-932749-66-9

Vol. 67
Matthias Sabathil
Opto-electronic and quantum transport properties of semiconductor nanostructures
156 Seiten
ISBN 3-932749-67-7

Vol. 68
Frank Fischer
Growth and electronic properties of two-dimensional systems on (110) oriented GaAs
139 Seiten
ISBN 3-932749-68-5

Vol. 69
Robert Shau
Langwellige oberflächenemittierende Laserdioden mit hoher Ausgangsleistung und Modulationsbandbreite
198 Seiten
ISBN 3-932749-69-3

Vol. 70
Andrea Baumer
Structural and electronic properties of hydrosilylated silicon surfaces
163 Seiten
ISBN 3-932749-70-7

Vol. 71
Andreas Florian Kreß
Manipulation of the light-matter-inter-action in photonic crystal nanocavities
185 Seiten
ISBN 3-932749-71-5

Important addresses

Walter Schottky Institut
Technische Universität München
Am Coulombwall 3
85748 Garching
Germany
http://www.wsi.tum.de

Secretaries:

Veronika Enter
Tel.: ++49-89-28912761, Fax: ++49-89-28912737, e-mail: veronika@wsi.tum.de

Daniela Huber
Tel.: ++49-89-28912781, Fax: ++49-89-3206620, e-mail: daniela.huber@wsi.tum.de

Irmgard Neuner
Tel.: ++49-89-28912771, Fax: ++49-89-3206620, e-mail: irmgard@wsi.tum.de

Liane Lindner (SFB 631)
Tel.: ++49-89-28912751, Fax: ++49-89-28912737, e-mail: liane@wsi.tum.de

Faculty Members and Scientific Staff

Gerhard Abstreiter
Tel.: ++49-89-28912770, Fax: ++49-89-3206620, e-mail: abstreiter@wsi.tum.de

Markus-Christian Amann
Tel.: ++49-89-28912780, Fax: ++49-89-3206620, e-mail: mcamann@wsi.tum.de

Martin Stutzmann
Tel.: ++49-89-28912760, Fax: ++49-89-28912737, e-mail: stutz@wsi.tum.de

Peter Vogl
Tel.: ++49-89-28912750, Fax: ++49-89-28912737, e-mail: vogl@wsi.tum.de

Gerhard Böhm
Tel.: ++49-89-28912791, Fax: ++49-89-3206620, e-mail: boehm@wsi.tum.de

Dominique Bougeard
Tel.: ++49-89-28912777, Fax: ++49-89-3206620, e-mail: bougeard@wsi.tum.de

Martin Brandt
Tel.: ++49-89-28912758, Fax: ++49-89-28912737, e-mail: brandt@wsi.tum.de

Martin Eickhoff
Tel.: ++49-89-28912889, Fax: ++49-89-28912737, e-mail: eickhoff@wsi.tum.de

Jonathan Finley
Tel.: ++49-89-28912778, Fax: ++49-89-3206620, e-mail: finley@wsi.tum.de

Anna Fontcuberta i Morral
Tel.: ++49-89-28912779, Fax: ++49-89-3206620, e-mail: annafm@wsi.tum.de

Jürgen Freyer
Tel.: ++49-89-28912789, Fax: ++49-89-3206620, e-mail: freyer@wsi.tum.de

José Antonio Garrido Ariza
Tel.: ++49-89-28912766, Fax: ++49-89-28912737, e-mail: garrido@wsi.tum.de

Matthew Grayson
Tel.: ++49-89-28912778, Fax: ++49-89-3206620, e-mail: grayson@wsi.tum.de

Ralf Meyer
Tel.: ++49-89-28912790, Fax: ++49-89-3206620, e-mail: meyer@wsi.tum.de

Ulrich Rant
Tel.: ++49-89-28912776, Fax: ++49-89-3206620, e-mail: rant@wsi.tum.de

Dieter Schuh
Tel.: ++49-89-28912779, Fax: ++49-89-3206620, e-mail: schuh@wsi.tum.de

Marc Tornow
Tel.: ++49-89-28912772, Fax: ++49-89-3206620, e-mail: tornow@wsi.tum.de

Alexandros Trellakis
Tel. : ++49-89-28912741, Fax: ++49-89-28912737, e-mail: trellakis@wsi.tum.de